CHALMERS

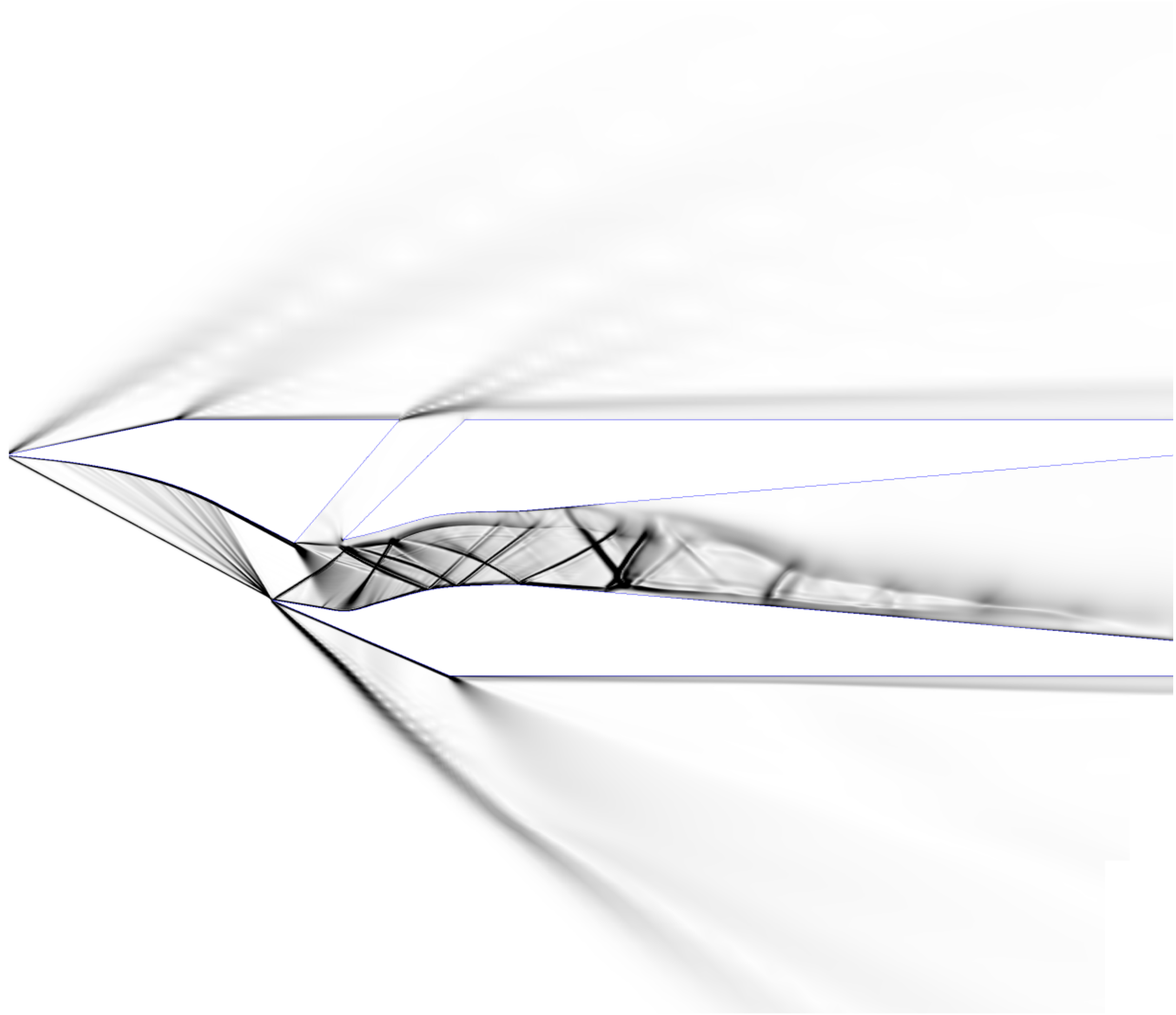

Validation and Parametric Study of Supersonic Air Intake

Master's thesis in Applied Mechanics

JAKOB EKERMO

Department of Mechanics and Maritime Sciences
CHALMERS UNIVERSITY OF TECHNOLOGY
Göteborg, Sweden 2018

MASTER'S THESIS IN APPLIED MECHANICS

Validation and Parametric Study of Supersonic Air Intake

JAKOB EKERMO

Department of Mechanics and Maritime Sciences
Division of Fluid Dynamics
CHALMERS UNIVERSITY OF TECHNOLOGY

Göteborg, Sweden 2018

Validation and Parametric Study of Supersonic Air Intake
JAKOB EKERMO

Master's thesis 2018:18
Department of Mechanics and Maritime Sciences
Division of Fluid Dynamics
Chalmers University of Technology
SE-412 96 Göteborg
Sweden
Telephone: +46 (0)31-772 1000

Cover:
Illustration of complex shock wave patterns residing in the intake for a simulation in the supercritical operating range.

Chalmers Reproservice
Göteborg, Sweden 2018

Validation and Parametric Study of Supersonic Air Intake
Master's thesis in Applied Mechanics
JAKOB EKERMO
Department of Mechanics and Maritime Sciences
Division of Fluid Dynamics
Chalmers University of Technology

Abstract

The current study was carried out on behalf of GKN Aerospace as a Master's thesis at Chalmers University of Technology. The Department of Propulsion Engineering at this company wished to develop a deeper understanding into the performance of supersonic engine intakes and to relate this to the influential physical notions and geometry alterations. The ultimate objective was to obtain a CFD model to study the effects of key variations of geometrical and physical parameters on the aerodynamic performance. This model was initially to be validated on a model scale against the results of wind tunnel tests. The specific means by which this validation was done was to compare the mass flow and total pressure recovery at the outlet of the intake, as predicted by wind tunnel tests and by the CFD model. The results of the validation study show that despite the two-dimensional geometry of the intake, the flow in the interior of the intake is highly three-dimensional. This is mainly attributed to the separation in the subsonic diffuser, induced by shock waves and end-wall, turbulent effects. This has highlighted distinct differences in the means by which the global, gross effects of total pressure recovery is estimated in wind tunnel tests as compared to the model. Nevertheless, disregarding from the explicable differences, a sound model was achieved.

The secondary objective was to scale this generic model intake to a real size, to meet the mass flow requirements of a typical engine. As the scaling was performed, alterations to the external compression ramp geometry was implemented. This was done in order to investigate the global effects of having an *isentropic*, continuous-curve type ramp as compared to a discrete, two-step ramp. As the parametric study was carried out, it was concluded that the effect of having a discrete ramp was mainly that of reducing the mass flow swallowed by the intake. While having comparable levels of global total pressure recovery, the discrete-ramp geometry featured the positive effect of limiting flow separation and distortion in the diffuser section. This effect was attributed to the reduction in velocity and momentum of the ingested mass flow, due to less efficient external compression and increased mass flow spillage. Finally, aerodynamic performance of the large-scale intake was assessed in terms of aerodynamic drag forces and pitch torque. On the basis of the conclusions formed in this project, some recommendations for future work were given.

Keywords: Intake, Supersonic, Rectangular, Shock wave, Separation, Diffuser, SST, Shear Stress Transport, Validation Study, Parametric Study, Wind Tunnel

Preface

The idea of taking on a Master's thesis involving a CFD study of a supersonic engine intake came into existence after taking a course in *Compressible Flow* at Chalmers University of Technology in the Spring of 2017. I had previously been introduced to the field of *Computational Fluid Dynamics* and the interest steadily grew as I was able to perform an introductory study on the SR-71 Blackbird engine intake. Being enrolled in the final year of my engineering studies, I wished to deepen my knowledge and experience in this academic field to be able to pursue a career therein. Being offered the opportunity to perform this thesis at GKN Aerospace was a great chance to do this. The Department of Propulsion Engineering at this company wished to create a validated CFD model of a generic supersonic intake, on which basic design alterations could be made to predict and study global aerodynamic performance.

Acknowledgements

At the conclusion of this project, I am very proud of what I have accomplished in terms of the results of the study and the personal development gained. It has been the most interesting and awarding, yet the most difficult part of all my years of University studies. To carry out a project of this magnitude for the first time has given me invaluable knowledge and experience. I am today very humbled by this process. Technical difficulties have been manifold and ranged from troubleshooting ambiguous error codes in the model to constructing a robust and suitable mesh. Practical difficulties have included commuting several hours a day and staying focused and disciplined prior to a long-awaited graduation.

I would like to express my deep gratitude towards my supervisors at GKN Aerospace, Bernhard Gustafsson, Thomas Johansson, Patrick Nilsson and Kim Stenholm, for their invaluable support, encouragement and patience. I would like to especially thank Bernhard, who has been my CFD supervisor. He has helped me along every small step of the way with great experience and knowledge relating to every aspect of CFD modelling. I hope to be able to return the favor by providing an insightful report along with a robust intake model.

Also, I would like to thank my thesis supervisor at Chalmers University of Technology, Niklas Andersson. Apart from sharing his experience and knowledge, he has allowed me to work independently without requiring frequent updates of the work progress. Moreover, it was from a University course in *Compressible Flow*, which he led, that I got the inspiration of taking on this thesis in the first place.

Furthermore, my opponents Caroline Olofsson and Emma Sundell deserve my sincere recognition for attentively reading my report, attending my oral presentation and providing useful feedback. Their efforts, for which I am very grateful, have allowed me to further improve the quality of this report.

Finally, I would like to thank all my friends and family who have supported me. Not only have they showed great interest in my thesis work, but they have also understood and accepted me not being the best version of myself during some of the hard times of this project. To all my classmates, thank you for these years of friendship and being in the trenches together.

On a final note, I am very happy that I chose to write this thesis and beyond excited to graduate and pursue a career in the field of *Computational Fluid Dynamics.*

Trollhättan, October 2018, Jakob Ekermo

Nomenclature

Physics Constants

C_p	Reference, specific heat of air in an isobaric process	$1006\, J \cdot kg^{-1} K^{-1}$
C_v	Reference, specific heat of air in an isochoric process	$717.1\, J \cdot kg^{-1} K^{-1}$
γ	Ratio of specific heats of air	1.4
R	Specific gas constant of air	$287\, J \cdot kg^{-1} K^{-1}$
g	Gravitational constant	$9.81\, m \cdot s^{-2}$

Variables

t	Time $[s]$
a	Local speed of sound $[m \cdot s^{-1}]$
ρ	Density $[kg \cdot m^{-3}]$
p	Pressure $[kg \cdot m^{-1} \cdot s^{-2}]$
T	Temperature $[K]$
x, y, z	Displacement components in a Cartesian coordinate system $[m]$
u, v, w	Velocity components in a Cartesian coordinate system $[m \cdot s^{-1}]$
V	Magnitude of velocity vector $[m \cdot s^{-1}]$
e	Internal energy $[J \cdot kg^{-1}]$
h	Enthalpy $[J \cdot kg^{-1}]$
θ	Deflection angle $[^\circ]$
β	Shock wave angle $[^\circ]$
μ	Dynamic viscosity $[kg \cdot m^{-1} \cdot s^{-1}]$
ν	Kinematic viscosity $[m^2 \cdot s^{-1}]$
τ	Viscous shear stress $[kg \cdot m^{-1} \cdot s^{-2}]$
S	Strain-rate tensor $[s^{-1}]$
n	Distance between cell nodes $[m]$
k	Turbulent kinetic energy $[m^2 \cdot s^{-2}]$
ϵ	Turbulent eddy dissipation rate $[m^2 \cdot s^{-3}]$
ω	Turbulent eddy frequency $[s^{-1}]$
$\dot{q}$	Heat flux $[J \cdot kg^{-1} \cdot s^{-1}]$
K	Thermal conductivity $[J \cdot s^{-1} \cdot m^{-1} \cdot K^{-1}]$
$\dot{m}$	Mass flow $[kg \cdot s^{-1}]$
W	Specific work $[J \cdot kg^{-1}]$
D	Drag force $[kg \cdot m \cdot s^{-2}]$
L	Lift force $[kg \cdot m \cdot s^{-2}]$
F	Force (used in multiple contexts) $[kg \cdot m \cdot s^{-2}]$
P	Pitch torque $[kg \cdot m^2 \cdot s^{-2}]$
A	Area $[m^2]$

Dimensionless coefficients

M	Mach Number
Re	Reynolds number

TPR Total Pressure Recovery (usually denoted η)
MFR Mass Flow Ratio/Capture Area Ratio (usually denoted ϵ)
C_D Drag coefficient
y^+ Non-dimensional wall distance
CFL Courant (Courant-Friedrichs-Lewy) number
SF Scale factor used for geometry transformation
$DIST$ Distortion factor
δ_{ij} Kronecker delta

Indices and Abbreviations

p Referring to an isobaric process
v Referring to an isochoric process
s Referring to an isentropic process
0 Referring to stagnation (total) conditions
∞ Referring to free stream (capture face) conditions
d Referring to design conditions of intake
e Referring to engine face conditions
n Referring to conditions normal to pertinent shock wave
N Referring to nozzle exhaust conditions
1 Referring to conditions upstream of pertinent shock
2 Referring to conditions downstream of pertinent shock
$*$ Referring to conditions obtained after an isentropic acceleration to sonic speed
x, y, z Referring to the axes of a Cartesian coordinate system
int Referring to internal contribution from the interior of the intake
ext Referring to external contribution from the exterior of the intake
add Referring to additive contribution
PT Referring to axis of pitch torque
$corr$ Referring to corrected quantity
w Referring to conditions adjacent to walls
ss Referring to conditions at small scale
ls Referring to conditions at large scale
V Referring to implementation in validation study
P Referring to implementation in parametric study
IR Referring to *Isentropic Ramp*, a continuous-curve type intake ramp
DR Referring to *Discrete Ramp*, an intake ramp featuring straight segments
LE Referring to leading edge
TE Referring to trailing edge
BP Referring to intake back pressure
LP Referring to low intake back pressure
HP Referring to high intake back pressure

Contents

Abstract i

Preface iii

Acknowledgements iii

Nomenclature v

Contents vii

List of Figures ix

1 Introduction 1
1.1 Background . . . 2
1.2 Purpose . . . 2
1.3 Limitations . . . 3

2 Method 4
2.1 Geometry and Mesh Creation . . . 4
2.2 CFD Modelling . . . 5
2.2.1 Boundary Conditions . . . 6
2.2.2 Model Settings . . . 7
2.2.3 Review of the SST Turbulence Model . . . 7
2.3 Post-Processing and Analysis of Results . . . 9
2.3.1 Validation Study . . . 9
2.3.2 Mesh Convergence Study . . . 9
2.3.3 Parametric Study . . . 10
2.3.4 Convergence Criteria . . . 10

3 Theory 12
3.1 Thermodynamic Properties of Air . . . 12
3.2 Governing Conservation Principles . . . 13
3.2.1 Conservation of Mass . . . 13
3.2.2 Conservation of Momentum . . . 14
3.2.3 Conservation of Energy . . . 14
3.2.4 Navier-Stokes Equations . . . 15
3.3 Shock Relations . . . 15
3.4 Area-Velocity Relation . . . 17
3.5 Area-Mach Number Relation . . . 18
3.6 Compressible Mass Flow Equation . . . 18
3.7 Aerodynamic Forces . . . 19
3.8 Ideal Brayton Cycle . . . 21
3.9 Jet Propulsion . . . 22

4 Results 23
4.1 Geometry Creation . . . 23
4.2 Results of Validation Study . . . 24
4.2.1 Mass Flow and Total Pressure Recovery . . . 24
4.2.2 Conclusions of Validation Study . . . 29
4.3 Results of Parametric Study . . . 31
4.3.1 Mass Flow and Total Pressure Recovery . . . 31
4.3.2 Aerodynamic Forces . . . 35
4.3.3 Conclusions of Parametric Study . . . 38

5 Discussion **40**

References **42**

A Validation study simulation, $M_{V,1}$ **43**
A.1 Critical operating point, $p_{1,4}$ . . . 43
A.2 Subcritical operating range, $p_{1,5}$ . . . 45
A.3 Supercritical operating range, $p_{1,1}$ . . . 46

B Validation study simulation, $M_{V,2}$ **48**
B.1 Critical operating point, $p_{2,4}$ . . . 48
B.2 Supercritical operating range, $p_{2,2}$ . . . 50

C Validation study simulation, $M_{V,3}$ **52**
C.1 Supercritical operating range, $p_{3,1}$, coarse/fine mesh . . . 52

D Validation study simulation, $M_{V,4}$ **53**
D.1 Critical operating point, $p_{4,3}$ . . . 53

E Parametric study simulation, $M_{P,1}$ **55**
E.1 Critical operating point, $p_{1,3}$ . . . 55
E.2 Subcritical operating range, $p_{1,5}$ . . . 59
E.3 Supercritical operating range, $p_{1,1}$ . . . 62

F Parametric study simulation, $M_{P,2}$ **64**
F.1 Supercritical operating range, $p_{2,1}$ . . . 64

G Parametric study simulation, $M_{P,3}$ **68**
G.1 Subcritical operating range, $p_{3,4}$ . . . 68
G.2 Supercritical operating range, $p_{3,1}$ . . . 72

H Parametric study simulation, $M_{P,4}$ **76**
H.1 Supercritical operating range, $p_{4,1}$ . . . 76

List of Figures

1.1 View of a generic, supersonic, rectangular engine intake including key terminology. 1
2.1 Isoview of model domain. 6
3.1 Illustration of characteristic angles as well as Mach number evolution over an oblique shock wave. 16
3.2 Simplified view of the jet engine cycle. 21
3.3 Ideal Brayton Cycle represented in a h-s and T-s graph. 21
4.1 Isometric view of intake geometry. 23
4.2 Profile views of intake ramp geometry configurations. 24
4.3 Mass flow versus total pressure recovery for small-scale intake, $M = M_{V,1}$ 25
4.4 Mass flow versus total pressure recovery for small-scale intake, $M = M_{V,2}$ 26
4.5 Mass flow versus total pressure recovery for small-scale intake, $M = M_{V,3}$ 26
4.6 Mass flow versus total pressure recovery for small-scale intake, $M = M_{V,4}$ 27
4.7 Distortion of total pressure in evaluation plane for small-scale intake. 30
4.8 Procedures of estimating the total pressure in the evaluation plane. 30
4.9 Mass flow versus total pressure recovery for large-scale intake, $M = M_{P,1}$ 32
4.10 Mass flow versus total pressure recovery for large-scale intake, $M = M_{P,2}$ 33
4.11 Mass flow versus total pressure recovery for large-scale intake, $M = M_{P,3}$ 33
4.12 Mass flow versus total pressure recovery for large-scale intake, $M = M_{P,4}$ 34
4.13 Pressure-induced drag acting on intake for the different conditions of flight. 36
4.14 Shear-induced drag acting on intake. 37
4.15 Pressure-induced pitch torque acting on intake. 38
4.16 Distortion of total pressure in evaluation plane for large-scale intake. 39

1 Introduction

Modern supersonic aircraft rely heavily on the performance of the engine intake, whose primary function is to decelerate and direct the incoming air to the engine to allow for a propulsion of the aircraft to be achieved. It is argued by many authors, of which a few are mentioned here [12] [26], that the engine intake is critical to the overall aerodynamic performance of the propulsion unit. The flight domain is paramount to understanding engine intake design philosophy, as the deceleration and compression of air is achieved in different manners depending on the desired Mach number range. Engines for subsonic operation, mainly found on subsonic passenger aircraft, utilize rotational parts in the form of stator and rotor blade rows in the compressor and turbine, where the former requires a work input supplied by the latter to compress the air to a sufficient pressure. In contrast, engines for supersonic operation employ an initial air intake prior to the compressor, that is less intricate in the sense that it has no moving parts, as the kinetic energy of the air is sufficient to achieve a high level of static pressure rise at supersonic speeds. Hence, the pressure rise in the latter mode, mainly performed in the intake, is achieved by a successive diffusion of air velocity with no work input.

To aid in the description of a generic supersonic intake, a schematic view that includes key terminology is provided in Figure 1.1. A supersonic intake generally involves a supersonic and a subsonic diffuser, giving rise to a mixed-compression mode. The supersonic diffuser is a convergent section, designed in such a way that the flow area is reducing towards the throat section, where the area is at a minimum. The domain of supersonic flight is associated with the presence of shock waves, which originate due to the inability of sudden changes of flow properties to propagate upstream at a velocity greater than the local speed of sound. The design procedure involves choosing a sequence of oblique shock waves, that are characterized by the varying angles they form to the flow upstream of the shock, and to control the strength of the terminal, normal shock which controls the transition from supersonic to subsonic flow. As the flow enters the subsonic diffuser at a velocity below the speed of sound, further deceleration is achieved by means of a flow area increase, hence this constitutes a divergent section.

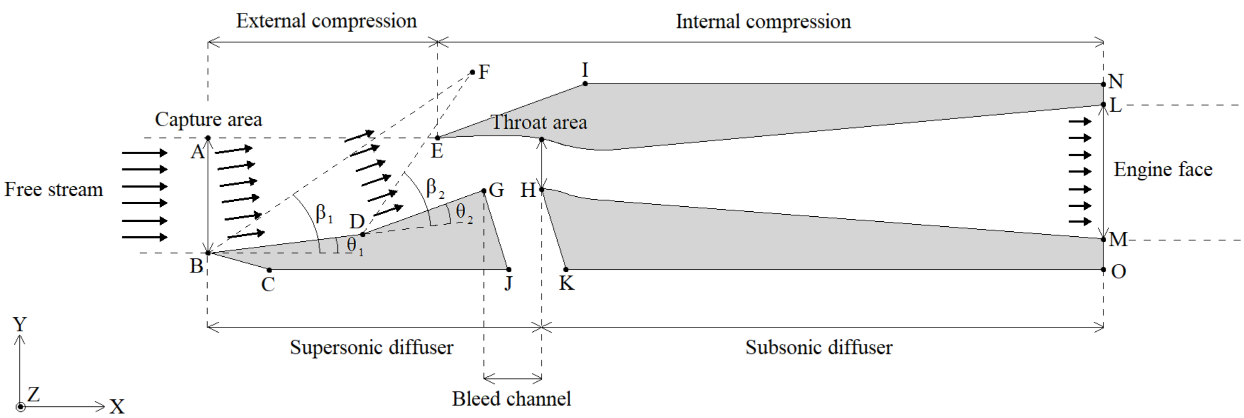

Figure 1.1: *View of a generic, supersonic, rectangular engine intake including key terminology.*

When evaluating the aerodynamic performance of supersonic intakes there is a strong consensus among authors, of which a few are mentioned here, as to the objectives that are of importance. The primary objective to engine intake design is to maximize the total pressure recovery [7] [10] [22], by means of minimizing total pressure losses. These losses are a direct consequence of entropy creation due to the various transport phenomena that occur as the flow decelerates from the free-stream supersonic flow to the subsonic flow at the intake outlet, such as thermal conduction and viscous diffusion across shock waves [2]. The intake outlet, also denoted engine face, is identified in Figure 1.1. Saravanan et al. [22] argues that a good total pressure recovery increases the attainable engine thrust and reduces the fuel consumption. Ran & Mavris [20] elaborates on this by estimating that for 1% total pressure loss, the engine suffers at least 1% thrust loss. Furthermore, a quantity that is of essential interest is the mass flow entering the engine [10] [22]. This objective is usually stated as a criterion rather than a quantity subject to optimization [10], meaning that the engine requires a certain mass flow as a function of the operating Mach number, and the excess can be utilized as a bypass flow that is redirected prior to the engine. Moreover, it is desired that the air flow at the engine face exhibits a uniform pressure and velocity distribution, while maintaining a Mach number around 0,4 [22] [20]. Secondary objectives to engine intake design are the minimization of added aerodynamic drag to the aircraft, which will reduce the required engine thrust that is needed for the desired level of aircraft propulsion, as well as minimizing the added mass to the aircraft [7].

Benchmarking procedures used in modern industry involves experimental, numerical and analytical methods. There is an extensive analytical framework for analysis of shock waves and boundary layer evolution in external flows. However, the interaction of these phenomena in supersonic intakes, potentially including the effects of separation and viscosity, increases the flow complexity to such an extent that analytical methods are insufficient to accurately model the intake flow [23]. Furthermore, it is argued [23] that the costs of experimental tests limits their use to the evaluation of special cases, such as validation of numerical results. Also, taking advantage of the dynamic similarity laws, these procedures require scaled physical models of the intakes that are the subject of the study, further compromising the feasibility of parametric studies. [10] argues on the basis of the conclusion formed by [19], that some major advances in technology have resulted in a revolution of the process of intake design. The first is the development of simulation software for aerodynamic performance prediction that features accuracy, robustness and efficiency. As an example of a highly efficient simulation tool, the 2ES3D (Euler semi-empirical simulation for three-dimensional intakes) has been developed [5], and is able to accurately predict total pressure recovery and mass capture ratio for a significant range of the performance curve of a three-dimensional supersonic intake in a few minutes on a single-processor workstation. Consequently, this tool was chosen as the CFD software in an automated design optimization study conducted on the French VESTA missile [9]. The 2ES3D solver was coupled with a genetic algorithm for the selection and generation of improved designs in an automated procedure, where an optimized shape of the supersonic intake was achieved. The conclusion of that study was that a comparable design in terms of aerodynamic performance was achieved in three months using the automated approach, where classical methods used for the original design required about two years. On the other end of the efficiency spectrum are the full Navier-Stokes simulations using conventional two-equation turbulence models, that may require computational efforts in the range of several hundreds of CPU hours [6]. Another of these major technological advances is the continued increase of computer and network performance, as it is estimated that processor speeds double every 18 to 24 months [10]. As this evolution progresses, CFD tools that are heavy in terms of computational requirements may be utilized to a greater extent in larger parametric studies as well as automated design procedures.

1.1 Background

The current study was performed as a Master's thesis at Chalmers University of Technology on behalf of the supplier of the mission, GKN Aerospace. The Department of Propulsion Engineering of said company wished to develop a deeper understanding into the performance of supersonic intakes and relate this to the physical notions as well as the geometrical variations that are influential to the aerodynamic performance, by creation of a CFD model. It was therefore of great interest to not only perform a numerical, parametric study but also a comprehensive literature study to profit from the conclusions drawn from previous work on the subject. While there is a wide range of parameters that influence the intake performance, the essential interest has been defined by selecting a few of these. The design variation is focused on the external compression ramp shape. Furthermore, physical parameters of interest that determine the domain of operation are the operating Mach number as well as the back pressure created at the engine face. Considering these conditions as the governing input parameters, the output is the performance in terms of total pressure recovery, engine mass flow, flow distortion and aerodynamic drag. As a starting point, the results of wind tunnel tests conducted on a generic, rectangular, supersonic intake were made available. This particular intake features a ramp of continuous deflection curvature rather than the typical ramp which is comprised of a discrete number of inclination steps. It was therefore of great interest to compare these two conceptual designs in terms of their individual performance.

1.2 Purpose

The purpose of this project is to create a CFD model of a supersonic intake, which initially is to be validated on a small, model scale against existing wind tunnel test results. As this model is created and validated, the secondary objective is to employ it to perform a parametric study on a full-scale, generic intake. The performance in terms of total pressure recovery, engine mass flow, flow distortion and aerodynamic forces is to be evaluated as a function of the ramp geometry of the intake as well as the free-stream Mach number and intake back pressure. Two ramp geometry configurations will be the subject of this parametric study. Firstly, the continuous-curvature type, *isentropic* ramp that was the subject of the small-scale, validation study will be used as a reference. Secondly, another configuration will be generated by replacing this curvature with two straight segments, such that the initial and total deflection angles of both ramp geometries are the same. A comprehensive literature study will be carried out simultaneously to support the project and to benefit from conclusions drawn from previous work. The ultimate goal is to use these results to obtain a deeper understanding into how these variations affect the intake performance as specified above and to obtain a model that can be used to generate and evaluate further candidate geometries in the future.

1.3 Limitations

Due to the time frame of this project, some limitations were introduced in order to set the scope of the work to a feasible extent. As the project was concluded, these limitations were the basis of recommendations for future work, where a scope extension could prove to be interesting. For the sake of structure and conciseness, these limitations are listed below.

1. Due to the requirements of CFD simulations in terms of computational efforts, only two geometry configurations were the subject of the study, as outlined in Section 1.2. Furthermore, the performance in the intermediate, parametric range of physical conditions was estimated by means of linear interpolation.

2. A mesh convergence study was conducted on the small, model scale of the intake to estimate the mesh dependency of the results. This did not include the whole Mach number range but was limited to a single Mach number case. The results on the small scale proved to be independent of mesh size. How this dependency translated to the full scale was neglected, but it is reasonable to suspect that viscous effects are less pronounced when the model is enlarged as they are absolute in size, resulting in a higher Reynolds number.

3. The effects of the aircraft fuselage on the free-stream flow was neglected. It is reasonable to suspect that an interaction of the free-stream flow with the fuselage will cause a change in variables required for boundary conditions such as static and total pressure as well as angle of attack and yaw. It was therefore assumed that the free-stream conditions are the ambient, atmospheric conditions and that the flow is completely aligned with the axis of the intake.

4. The flight mode selected for this study corresponds to cruise operation, indicating a constant-velocity, free-stream flow that is completely aligned with the axial direction of the intake. Should maneuverability of the aircraft be taken into consideration, this would include variations of angles of attack and yaw, changing the free-stream flow direction. Hence, these variations were neglected.

5. Minor simplifications were made to the geometry of the reference, small-scale intake, to reduce mesh complexity. These changes were made such that the results were not compromised.

6. Limited consideration was given to the dependency of the results on the choice of turbulence model implemented in the CFD model. On the basis of the literature study, supervisor recommendations as well as time window of the project, a suitable turbulence model was chosen.

7. The choice of mesh resolution adjacent to walls and parameters such as the size of time steps was made while taking into consideration the associated increase in computational efforts, respecting the time window of the project.

2 Method

This chapter aims at reproducing the methodology involved in the creation of the CFD intake model that is the basis of this study. The starting point is considered to be the scaled, physical model of the intake that is the subject of the wind tunnel test results. The procedure of obtaining a complete CFD model will be outlined in chronological order, starting with the geometry and mesh creation and proceeding to the numerical aspects of the CFD solver chosen. As the data is gathered, the objective is then to describe how these are reduced into results by means of post-processing. To simplify the extraction of model settings from this chapter, Table 2.1 is used to summarize all the discussed settings in a structured format. Furthermore, Figure 2.1 illustrates the domain and the discussed boundaries.

2.1 Geometry and Mesh Creation

The primary intake studied in in this project is of the rectangular, mixed-compression type with a continous-curve external ramp shape. Subsequent to the ramp is a bleed channel in the centerbody, after which a duct aligns the flow with the axial direction. The purpose of the bleed channel is to divert the boundary layer flow of the ramp to the exterior of the intake, as it is of less quality in terms of total pressure than the flow far away from walls. Finally, a subsonic diffuser is implemented, leading the flow to the engine face. A generic representation of the intake profile is seen in Figure 1.1. The creation of the geometrical model was done using the software *ANSA*. For the sake of an efficient implementation, some geometrical features that were deemed not critical for the results were removed or simplified. This involved eliminating an extrusion of the sidewalls over the lip wedge (corresponding to the side *E-I* in Figure 1.1) as well as a simplification of the shape of the bleed hole. In the latter case, rounded corners of a rectangular bleed hole shape were removed to simplify the mesh, with the condition that the cross-sectional area of the bleed hole was kept intact. An isometric view of the model geometry is provided in Figure 4.1. The curves of the intake profile shape were given as sets of coordinates with tangent angles at each point. As these points were implemented and a curve adaptation was performed to intersect these points, the resulting shapes featured one or more inflexion points, where a concavity-convexion transition would occur. This was deemed to be an undesirable feature and one or more points causing this were neglected. This approximation led to the initial deflection angle as well as the total deflection angle of the ramp being underestimated by $0.2°$, a deviation that was considered to be insignificant and likely within component tolerance limits. Finally, the free-stream domain was extended to the farfield in the upstream and transverse directions, respectively.

The resulting domain as seen in Figure 2.1 was of a rectangular shape, where the sides corresponded to inlet and outlet at which the free stream would flow perpendicularly as well as sides along which the free stream would flow parallel. The extension into the farfield of the domain was made such that the oblique shock waves forming at the forebody of the intake would be swallowed by the free-stream outlet boundary, simplifying the implementation of boundary conditions. This was achieved by using Equation 3.48 to approximate the wave angles. The evaluation of quantities such as the total pressure and mass flow at the intake outlet was done in a plane just prior to the engine face of the subsonic diffuser, in accordance with the corresponding pressure rake location in the wind tunnel tests. A constant-area extension was added to the subsonic diffuser. As shall be discussed in Section 2.2.1, this was done in order to simplify the implementation of an intake outlet boundary condition.

The meshing procedure was far more intricate than the creation of the geometry, as this involved more freedom of choice and guidelines to follow. As the geometry was created, this was exported to *ANSYS ICEM CFD v17.1* where a multi-block, structured meshing approach was adopted. The resulting cells would be of the hexahedral type. To minimize the requirements of computational efforts associated to simulations, the mesh was very coarse in the far-field domain where free-stream conditions would dictate the flow. Furthermore, the mesh was refined in the interior of the intake where large gradients of thermodynamic properties and complex flow structures were expected. This was done in the regions of shock waves, boundary layers etc. Moreover, the extension added to the subsonic diffuser was meshed with hexahedral cells initially, transitioning into tetrahedral cells with continuously increasing coarseness in the axial direction. Should the cell sizes increase too rapidly, pressure waves may reflect in this interface. This is analogous to matching the impedance in an electrical system to avoid reflections of signals or to match the thickness of a guitar string to avoid wave reflections.

Two dimensionless parameters that are indicators of a mesh that is qualitative and adapted to the specific application are the CFL and y^+ numbers, which are both locally defined. The CFL number (Courant-Friedrichs-Lewy), also usually referred to as the Courant number, applies primarily to transient flow simulations [4]. For a one-dimensional grid, it is defined as;

$$CFL = \frac{u\Delta t}{\Delta x} \tag{2.1}$$

This parameter indicates how far flow information will travel by means of convection during a discrete time step and relates that distance to the local cell size. As the governing equations upon which the CFD solver is based are discretized and a numerical scheme is chosen, cell values of flow properties are iterated upon and based on linear combinations of the corresponding values of neighboring cells. Hence, if a fluid element were to be considered, it is important that this element does not displace too far during a time step into a region that has no influence on its thermodynamic state. Consequently, for the sake of numerical stability, the desire is to limit this number to respect recommendations that are set depending on the application. However, it is argued [4] that *ANSYS CFX*, as an implicit code, does not require this number to be small to ensure numerical stability.

The other dimensionless number that is of interest, y^+, relates to the treatment and resolution of the flow boundary layers adjacent to walls. The definition follows from [4];

$$y^+ = \frac{\sqrt{\tau_w/\rho} \cdot \Delta n}{\nu} \tag{2.2}$$

This is an indicator of the transverse displacement in a boundary layer relative to its thickness, hence the normalization using variables that are expected to influence this thickness. In order to accurately resolve the flow in a boundary layer, it is desired to limit the value of this number to allow for the placing of one or several cell nodes inside this layer. The recommended upper limit is very specific to the application. Using wall functions, high-Reynolds-number applications may include values of y^+ safely exceeding 1000 while low-Reynolds-number applications with more predominant viscous effects may be limited to within $y^+ = 300$ [4]. Wall functions are an efficient way of modelling a boundary layer by extrapolating velocity profiles onto it, rather than actually resolving the boundary layer flow. This is done using the *log law*, also known as the *law of the wall*. Attempts were made to respect this latter condition for both the small-scale and large-scale intakes, relating to the resolution adjacent to all the interior walls.

Since the size of fully-developed boundary layers is absolute, the same absolute cell size is required regardless of model scaling to obtain the same level of boundary layer flow resolution. This means that a large-scale model will require a smaller relative wall cell size. Using a structured, block-meshing approach, it proved very difficult to lower this relative size beyond a certain extent. This is due to the primary drawback of this meshing strategy, which is the propagation of cell counts and/or sizes along common block edges. When trying to maintain the same absolute wall cell sizes while enlarging the model, larger local expansion ratios of cell sizes will be encountered. In this case, this occurred in regions where the coarse, free-stream mesh meets the finer, intake interior mesh that propagated outwards along the block structure. As these expansion ratios grew too large, the robustness of the mesh was compromised and numerical issues were encountered in the CFD solver. Ultimately, the wall cell sizes of the large-scale mesh were iteratively changed a few times and the final size was chosen such that these problems were avoided. Wall cell sizes, values of y^+ and mesh cell counts for the different meshes are summarized in Table 2.1.

2.2 CFD Modelling

The model involving geometry and mesh was subsequently exported to *ANSYS CFX v.18*, which was the software chosen to set up the CFD solver. This environment offers a lot of customizable settings, where a common trend is that a compromise has to be made between accuracy of results and associated computational efforts of simulations. This section describes the approach to setting up the solver. An essential setting is the selection of turbulence model. Hence, Section 2.2.3 will be devoted to this subject. Options that have been maintained in default setting will be neglected from discussion.

2.2.1 Boundary Conditions

The validity of boundary conditions are paramount to the fidelity of the CFD model. A majority of the numerical issues encountered in this project have been related to these. It is therefore of great importance to establish flow conditions encompassing the domain that do not interfere with the flow by means of boundary condition reflections or other mechanisms. A visualization of all the model boundaries are provided in Figure 2.1. The most simple boundary conditions apply to the walls of the intake, on the interior as well as the exterior. To allow for the simulation of boundary layers, all walls are considered to be of the type *No Slip Wall*, which implies zero velocity at the wall. The only exception to this is the walls of the subsonic diffuser extension, that are of the type *Free Slip Wall*, indicating no obstruction of the flow other than that of passing through the wall. This is related to the purpose of this component, which is to eliminate all gradients and mix the fluid to such an extent that it is axially uniform when passing through the intake interior outlet of the domain, namely the extension exit. This will reduce potential reflections of the boundary conditions on the outlet, such as pressure waves travelling back and forth in the intake. Furthermore, an additional purpose of this extension was to place the interior outlet far away from zones of potential separation, where circulation is induced in the flow. Placing this outlet close to the exit plane of the subsonic diffuser may cause the mass flow to enter the domain rather than leaving it, due to separation-induced circulation. Initially, when the extension was not long enough, this was a recurring problem during the iterative procedure of the CFD solver. This caused the solver to place walls at the parts of the diffuser outlet with an inverse mass flow. In turn, these walls caused a redirection of the local flow, successively spreading this effect to the whole diffuser outlet. The final outcome was a complete blockage of the mass flow, causing rapidly diverging solutions and a solver crash.

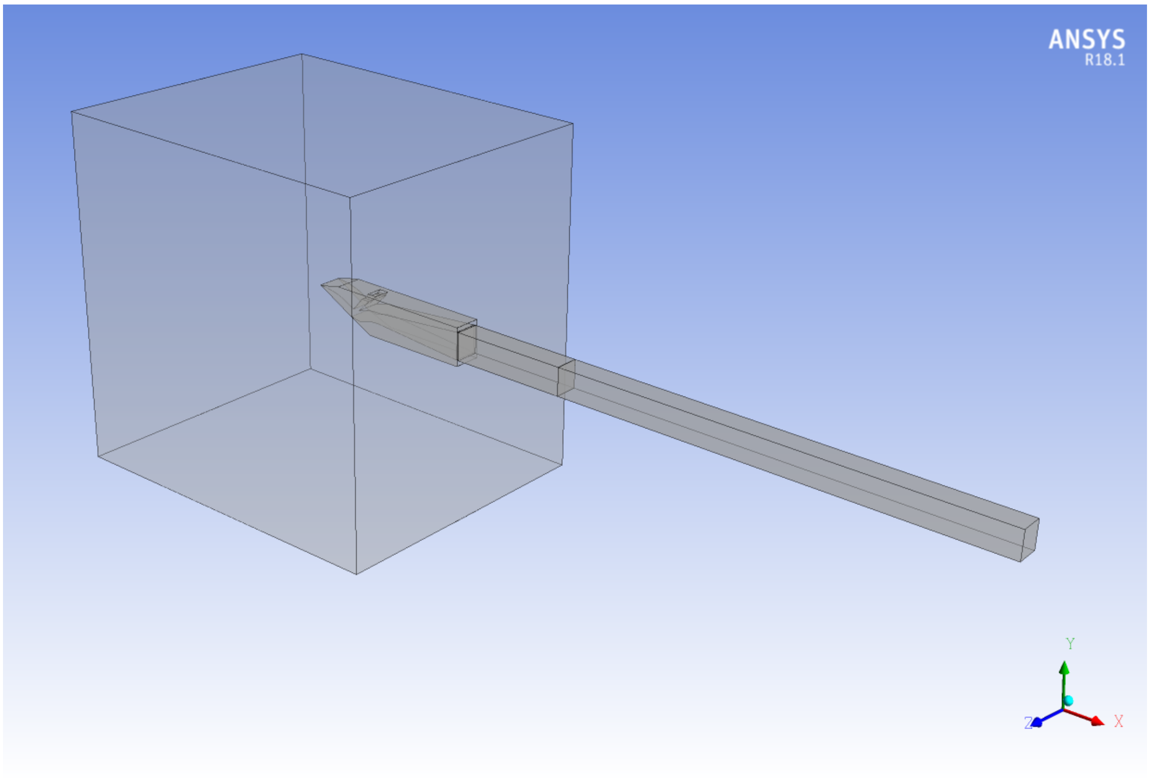

Figure 2.1: *Isoview of model domain.*

The type of boundary condition used for the interior outlet is *Outlet Subsonic*, where the static pressure was imposed. This is identified as the intake back pressure, a key parameter in this study. The far-field inlet and outlet of the domain is, with the exception of the case of solution initialization, defined as being *Inlet Supersonic* and *Outlet Supersonic*, respectively. At the inlet, the static and total pressure are defined, the first being known from the atmospheric conditions at the pertinent altitude and the second being known from the addition of the dynamic pressure corresponding to the desired Mach number (Equation 3.12). Furthermore, at the inlet boundary, the flow direction is chosen as *Normal to Boundary Condition* and the values of k and ϵ are set to $10^{-6}[m^2/s^2]$ and $10^{-6}[m^2/s^3]$, respectively, while setting these to be the transport variables. The static temperature is implicitly stated through the total temperature (Equation 3.10). The supersonic outlet does not require any additional information, as this information can not propagate upstream against a speed superior to that of the local speed of sound. Finally, the remaining sides of the farfield domain, along which the free-stream flow is parallel, are defined as *Opening Subsonic*, with the specification of the static pressure and temperature as well as *Zero Gradient* as turbulence option. In the case of initializing a stationary solution, the free-stream Mach number needs to be ramped up from zero, to avoid a sudden flow onset causing numerical issues. It is therefore a sound strategy to ramp up the free-stream flow to sonic speeds, utilizing *Inlet Subsonic* and *Outlet Subsonic* conditions, where the static pressure is defined. These values can be set to evolve from zero to a set value over a number of iterations by the use of *Expressions*, avoiding numerical issues. As a sonic solution is obtained, this can be used as a starting guess to initialize a supersonic, stationary simulation. The Mach number is then ramped up from sonic speeds to a desired supersonic value over a specified number of iterations. This ramping strategy has also been employed to smoothly increase or decrease the intake back pressure.

2.2.2 Model Settings

All the settings discussed in the forthcoming sections are summarized in Table 2.1, for the sake of structure and brevity. The settings categories are outlined in the tree section of *ANSYS CFX-Pre*. The first option in the tab *Analysis Type* involves choosing a stationary or transient formulation. As will be discussed in Sections 2.3.1 and 2.3.3, transient formulations were used to record time-averaged solutions, initialized from stationary, converged solutions. After choosing the simulation type, the number of and size of time steps are defined. *Auto Timescale* was selected for stationary simulations. For the stationary formulation, the implication of a time step is false. However, the option controls the time scale as a means of under-relaxing the equations as iterations are performed towards convergence [4]. For the transient, small-scale simulations, the size of the time step was $10^{-5}s$. For the transient, large-scale simulations it was selected as $10^{-3}s$. These values were selected to keep the CFL number at reasonable levels in regions of unsteady flow while limiting the computational efforts associated to a decrease of the time step size. Under the tab *Default Domain*, the fluid is assumed to be air obeying the ideal gas law, defined by Equation 3.2. Furthermore, *Total Energy* with the inclusion of the *Viscous Work Term* is chosen, allowing for an internal heating by means of viscous work. The *Shear Stress Transport* turbulence model is chosen, along with *Wall Functions Automatic* to model the behaviour of the boundary layer by means of extrapolation of velocity profiles, as previously discussed. Under the tab *Initialization*, *Low Intensity Turbulence* is selected, as a very low value of the turbulent kinetic energy κ is expected in the free-stream domain.

Under the tab *Solver Control*, *High Resolution* turbulence and advection schemes are chosen. Furthermore, for the transient simulations, the *Second Order Backward Euler* scheme was chosen and the *Convergence Control* implies 7-10 equilibrium iterations inside each time step. Finally, *High Speed Numerics* is selected, which is an option adapted to supersonic flow involving shocks. Some of the numerical characteristics of this option are the addition of a special type of dissipation at shocks as well as nodal pressure gradients being set to zero at all pressure boundaries and openings [4]. For transient simulations, the quantities that were to be time-averaged are defined in the *Trn Stats* tab of the *Output Control* section. The statistical representation of these variables were made by calculating the *Arithmetic Average*. To enlarge the scale of the model, a *Scale Transformation* was performed under the tab *Transformations*. Finally, in *Execution Control*, the initial guess from which the solution procedure is initialized is defined by choosing a preexisting, converged solution.

2.2.3 Review of the SST Turbulence Model

The choice of a suitable turbulence model to accompany the Navier-Stokes Equations is very much dependent on the application. On the basis of the literature study performed in this project as well as supervisor recommendations, the *SST* (Shear Stress Transport) model is an appropriate choice to account for the transport of turbulent quantities in the internal flow of the intake. This turbulence model, which is argued to be numerically robust [15], is a variation of the *BSL* (Baseline $k-\omega$) model, where the transported quantities are the turbulent kinetic energy k and the turbulent eddy frequency ω. Furthermore, the SST model is able to account for the transport of turbulent shear stress in adverse-pressure-gradient boundary layers, a present characteristic in a subsonic diffuser. Although the ability to predict separation is often praised, many authors point to its tendency of overestimating the onset of separation and turbulence in wakes, of which [24] is one. A review, provided by [11], concludes that the SST model has been found to provide very good predictions of wall-bounded flows even with highly separated regions.

Table 2.1: Selection of settings relating to geometry, mesh and model creation.

	Geometry
Software	*ANSA*
Simplifications	Smoothening of ramp curve shape
	Side wall extrusions over lip wedge removed
	Bleed holes made rectangular
	Meshing
Software	*ANSYS ICEM CFD v17.1*
Type	Multi-block, structured meshing (hexahedral cells)
	Unstructured meshing in diffuser extension (tetrahedral cells)
Mesh cell count	$8.6M$ (coarse mesh)
	$35.8M$ (fine mesh)
	$33.5M$ (modified, large-scale, fine mesh)
$\Delta n_w / y^+$	200 $[\mu m]$ / < 700 (coarse mesh)
	50 $[\mu m]$ / < 200 (fine mesh)
	750 $[\mu m]$ / < 500 (modified, large-scale, fine mesh)
CFL	< 100 in unsteady regions
	Boundary Conditions
Software	*ANSYS CFX v18.1*
Farfield Inlet	*Inlet Sub-/Supersonic*
	$p_\infty, v_\infty, T_{0,\infty} / p_\infty, p_{0,\infty}, T_{0,\infty}$
	Normal to Boundary Condition
	$k = 10^{-6} [m^2 \cdot s^{-2}]$
	$\epsilon = 10^{-6} [m^2 \cdot s^{-3}]$
Farfield Outlet	*Outlet Sub-/Supersonic*
	$p_\infty / \sim$
Farfield Sides	*Opening*
	p_∞, T_∞
	Zero Gradient
Intake Walls	*No Slip Wall*
Diffuser Extension Walls	*Free Slip Wall*
Intake Interior Outlet	*Outlet Subsonic*
	p_e
	Model Settings
Type	Stationary / Transient
Stationary time step size	*Auto Timescale*
Transient time step size	$10^{-5}[s]$ (small-scale)
	$10^{-3}[s]$ (large-scale)
Number of transient time steps	500 (small-scale)
	250 (large-scale)
Turbulence model	*Shear Stress Transport (SST)*
	Wall Functions Automatic
Miscellaneous	*Total Energy*
	Viscous Work Term
	Low Intensity Turbulence
	Second Order Backward Euler
	High Resolution Turbulence/Advection
	High Speed Numerics
	Convergence Criteria
RMS values of cellular residuals	*U-, V-, W-Mom, P-Mass, H-Energy*
	$\sim 10^{-5}$ of respective units
Global continuity imbalance	*U-, V-, W-Mom, P-Mass, H-Energy*
	$\sim 10^{-5}$ of respective units
Extension massflow imbalance	$< 1\%$

2.3 Post-Processing and Analysis of Results

This project consists of three individial studies, two of which are used for validation purposes prior to the final, parametric study. This section aims at describing the procedure for reducing data into results for these different parts as well as the validation methodology involved.

2.3.1 Validation Study

The starting point of this project was the results of the wind tunnel tests performed on a scaled, physical model of the intake. To specify, these results are in the form of characteristic curves relating to ratios of total pressure recovery and mass flow, for the implemented range of free-stream Mach numbers and intake back pressures. The specified, ambient conditions were those of sea level, $p_\infty = 101325[Pa]$ and $T_\infty = 288.15[K]$. Furthermore, these curves are obtained by varying the intake back pressure, and this procedure is done for a set of different supersonic Mach numbers. As the values of back pressure for the physical test cases were not given as an input, these were estimated and the objective was to reproduce the curves rather than individual test points of the wind tunnel tests. After initial stationary simulations, the flow in the subsonic diffuser showed tendencies of separation and subsequent unsteady flow. This tendency was pronounced in terms of fluctuating momentum residuals and periodic signals of mass flow and total pressure in the evaluation plane. To increase the statistical accuracy of the results used for validation purposes, a strategy was implemented where transient simulations were used to record time-averaged representatives of these results, after being initiated from stationary solutions as described in Section 2.2.2. The choice of two transient parameters directly influenced the numerical and statistical accuracy as well as the computational efforts of the simulations, namely the number of and the size of time steps. Implicitly defined by the choice of these two parameters is the total, physical simulation time. This should allow for the unsteady flow in the intake to progress long enough such that the reduced output signals of mass flow and total pressure in the evaluation plane display 5-10 periods of its lowest frequency component. Furthermore, the total simulation time chosen allowed for a particle of sonic speed to travel 5-10 times the length of the intake. When choosing the size of the time step, the governing parameter is the CFL number defined in Equation 2.1. The time step was chosen such that this number was safely below 100 in regions of unsteady flow.

When constructing the transient output signal of mass flow in the evaluation plane of the subsonic diffuser, the mass flow in each time step was simply evaluated by means of a summation of contributions across the plane. The statistical representative of the mass flow was then chosen as the arithmetic time-average of the values in each individual time step. The corresponding procedure used for the total pressure was a bit more intricate, as this also included a mass flow averaging of the total pressure in the evaluation plane inside each time step. The reason for choosing a *mass flow average* rather than an *area average* is that the total pressure is not spatially conserved and regions of high mass flow need to have a proportionally larger influence on this metric than regions of low mass flow. Finally, the mass flow entering the intake through the capture area was considered to be steady-state and calculated from free-stream conditions. The final values of mass flow and total pressure recovery ratios for each simulation case, corresponding to Equations 3.14 and 3.64, were then implemented to construct performance curves. To obtain these curves from the results of a set of evaluated cases, linear interpolation was used in the intermediate range. These were later compared to the corresponding curves of the wind tunnel test results. For this purpose, the software *MATLAB* was chosen.

2.3.2 Mesh Convergence Study

To evaluate whether the results obtained in this study were independent of the mesh and to ensure that a sufficient resolution was chosen, a mesh convergence study was performed. The scope of this study was the evaluation of a curve relating to ratios of total pressure recovery and mass flow for a single Mach number case using two significantly different mesh resolutions on the small-scale model. Furthermore, the local resolution adjacent to walls in the interior of the intake was further increased in the fine mesh. The cell count for the coarse and fine mesh was $8.6M$ and $35.8M$, respectively. Observing an approximate factor of 4 between these cell counts, this roughly corresponds to a halving of the cell sizes in the x- and y-directions, as depicted by Figure 1.1. This includes a decrease of the transverse wall cell size from 200 to 50 $[\mu m]$. The resulting values of y^+ as defined by Equation 2.2 for the two different meshes were roughly within 200 and 700, respectively. Hence, the fine mesh, unlike the coarse mesh, respected the condition of $y^+ < 300$ outlined in Section 2.1. Note that this evaluation was done using the variable *Yplus* rather than *Solver Yplus* in *CFX-Post*, which are two differing quantities as defined by [4]. The evaluation of the results of simulations run using these different meshes followed the same procedure that was outlined in Section 2.3.1. Finally, the comparison was made between the generated curves to evaluate the mesh sensitivity. It should be noted that the coarse mesh was used for all the other simulations in the Mach number and back pressure range of the validation study.

2.3.3 Parametric Study

The primary part of this project was the parametric study performed on the large-scale intake. The implementation featured two major differences as compared to the small-scale, validation study. Firstly, the geometry of the intake was scaled to a real size to match the mass flow requirements of a typical engine, according to the procedure outlined in Section 3.6. This resulted in a scaling factor of $SF \approx 37$. Secondly, the flight altitude was changed from sea level to a significantly higher, stratospheric design altitude for the intake, resulting in a dramatic decrease of ambient conditions of static pressure and temperature. The parametric variations of geometry concerned the construction of the external compression ramp, where the two configurations that were deemed to yield the most useful comparison were studied. The first was considered to be that of the reference intake, namely the continuous-deflection type ramp, also referred to as an *Isentropic Ramp (IR)*. To compare the effect of discrete flow deflections, or more specifically the effect of oblique shock waves to continuous compression modes, a two-step, discrete ramp *(DR)* was implemented as the second configuration. The condition for this configuration was that the initial and total deflection angle of the ramp would be the same as those of the reference case. Knowing these two angles, the point of intersection between ramp segments and their individual lengths were implicitly defined. As the deflection angle of the ramp is a key parameter to the obtained level of external compression, this was expected to yield an insightful comparison. The geometry candidates are illustrated in Figure 4.2.

Having these two geometries as the starting point, simulations were run with varying supersonic, free-stream Mach numbers and intake back pressures to predict the characteristic performance curves. The same strategy of running transient simulations initiated from stationary, converged solutions and recording time-averaged quantities, as described in Section 2.3.1, was used. Moreover, *Arithmetic Averages* in time of the distributions of static temperature and pressure, total temperature and pressure, density, Mach number, CFL number, wall shear and y^+ were used to visualize the flow, rather than instantaneous quantities. This was also the case for the small-scale simulations of the validation study. The statistical representation also involves *Minimum*, *Maximum*, *Standard Deviation* and *Root Mean Square* values for the same properties. These options allows for a calculation of the distortion factor of total pressure, as defined by Equation 3.15. Furthermore, these time-averaged representations of static pressure and wall shear were used to calculate the aerodynamic forces outlined in Section 3.7, by means of the respective integral expressions.

Finally, as the mesh convergence study was concluded, the decision was made to use a modified version of the fine mesh for the parametric study, translated into the large scale by means of a uniform scale factor $SF \approx 37$. Since it proved difficult to identify shock structures on the small-scale, coarse mesh, and large-scale simulations likely would require a greater number of cells to resolve the shock structures that are absolute in size, a modified version of the fine mesh was used. These modifications involved further decreasing the resolution in the free stream as well as increasing the resolution in the interior of the intake, including regions adjacent to walls. The resulting mesh used for the large-scale, parametric study had a cell count of $33.5M$. Due to the same difficulties of maintaining absolute wall cell sizes when enlarging the model, that were discussed in Section 2.1, the transverse sizes of cells adjacent to interior walls were set to roughly 750 $[\mu m]$.

2.3.4 Convergence Criteria

To ensure the numerical quality and convergence of the solutions obtained, regardless of which individual study it pertains to, monitoring of local and global residuals in *CFX-Solver* has been performed. On the local level, *Root Mean Square (RMS)* values of cellular residuals of mass flow, energy and momentum in all three principal directions of a Cartesian coordinate system have been limited to an order of magnitude of 10^{-5} of the respective units, whether it be stationary or transient simulations. Furthermore, on the global level, the continuity check was performed using the defined inflow and outflow boundaries of the domain, where the imbalance of inflow and outflow of the aforementioned quantities is of the order of magnitude 10^{-5} of the respective units.

Another tendency has proved capable of compromising the results while escaping detection in these continuity checks and relates to the stationary approximations from which final, transient simulations were initiated. This is primarily attributed to the addition of the diffuser extension as well as the far-field streching of the domain inlet, and relates to the implemented boundary condition ramping strategy discussed in Section 2.2.1. When imposing conditions of Mach number and static pressure on the domain inlet and intake outlet boundaries, a large number of iterations is required for these conditions to propagate throughout the domain and for the domain flow structures to become fully developed. This is due to the increased physical distance from these boundaries to the interior of the intake. It has therefore proven important to ensure that enough iterations are added to the simulation to allow for the solution to stabilize. To ensure that a fully developed flow was obtained for each stationary solution, an additional continuity check was implemented. This related to the inflow and outflow of mass to the diffuser extension. Since this extension was made significantly longer prior to the parametric study, this primarily concerns the large-scale simulations. For these cases, the imbalance of the mentioned mass flow was typically limited to within 1%, which was deemed acceptable.

3 Theory

This chapter aims at introducing the main theoretical framework of flow features present in a supersonic engine intake. The idea is to promote conceptual understanding and to introduce the tools behind preliminary design, such as shock relations that are used when designing the intake forebody at the design Mach number. Furthermore, aerodynamic forces as well as dimensionless performance coefficients are defined. Unless otherwise stated, [2] is used as the source for all derivations in this chapter. For the sake of being concise, some derivations will be omitted and the reader is assumed to have some prerequisites.

3.1 Thermodynamic Properties of Air

Two fundamental assumptions that will be made when implementing boundary conditions in the CFD model are the material equations relating to a calorically perfect and ideal gas;

$$h = C_p T \tag{3.1}$$

$$p = \rho R T \tag{3.2}$$

Adopting a gross-effect evaluation over a finite region, the principles of conservation of mass, momentum and energy lead to the following expressions;

$$\rho_1 V_1 = \rho_2 V_2 \tag{3.3}$$

$$p_1 + \rho_1 V_1^2 = p_2 + \rho_2 V_2^2 \tag{3.4}$$

$$h_1 + \frac{V_1^2}{2} = h_2 + \frac{V_2^2}{2} \tag{3.5}$$

The total (also denoted stagnation) properties of air, denoted with a subscript 0, are obtained by considering a complete, isentropic stagnation of the flow, using Equations 3.5 and 3.1;

$$C_p T + \frac{V^2}{2} = C_p T_0 \tag{3.6}$$

Furthermore, the specific heat can be expresssed as;

$$C_p = \frac{\gamma R}{\gamma - 1} \tag{3.7}$$

Momentum conservation across a sound wave yields the expression for the speed of sound;

$$a = \frac{V}{M} = \sqrt{\frac{\gamma p}{\rho}} \tag{3.8}$$

or equivalently, using 3.2;

$$a = \sqrt{\gamma R T} \tag{3.9}$$

Using Equations 3.6-3.9, the total temperature can be expressed as a function of the static temperature and Mach number according to;

$$\frac{T_0}{T} = 1 + \frac{(\gamma - 1)}{2} M^2 \tag{3.10}$$

The first law of thermodynamics can be written in a form that relates stagnation temperature to stagnation pressure and density;

$$\frac{p_0}{p} = \left(\frac{\rho_0}{\rho}\right)^{\gamma} = \left(\frac{T_0}{T}\right)^{\gamma/(\gamma-1)} \tag{3.11}$$

Consequently, using Equations 3.10 and 3.11, the total pressure and density can be written as;

$$\frac{p_0}{p} = \left(1 + \frac{\gamma - 1}{2} M^2\right)^{\gamma/(\gamma-1)} \tag{3.12}$$

$$\frac{\rho_0}{\rho} = \left(1 + \frac{\gamma - 1}{2} M^2\right)^{1/(\gamma-1)} \tag{3.13}$$

Finally, the total pressure recovery TPR is, by common practice, defined as the ratio of the total pressure at the engine face to the total pressure in the free stream flow prior to entering the intake. The parameter governing this performance indicator is thus;

$$TPR = \frac{p_{0,e}}{p_{0,\infty}} \tag{3.14}$$

A useful, statistical tool in the analysis of the results in a later stage of this project is the distortion coefficient, applied to total pressure at the engine face. As the name implies, it helps in determining the level of variance of a given property in an arbitrary domain, in this case applied to the engine face. It is defined as;

$$DIST = \frac{max(Q) - min(Q)}{mean(Q)} \tag{3.15}$$

where Q is an arbitrary quantity, in this case the total pressure.

3.2 Governing Conservation Principles

The physical principles that provide the framework for all fluid dynamics analysis are the governing equations of conservation of mass, momentum and energy. Generally, there are two approaches to establishing useful expressions [27]. Firstly, one can seek to determine gross effects over a finite region, allowing for a suitable implementation of the control-volume approach. This will be the case when determining property changes across a shock wave in Section 3.3. Secondly, the more general approach to establishing the expressions of conservation is to adapt an infinitesimal perspective to determine a continuous, point-by-point evolution of the respective properties. This leads to the differential equations of conservation that is the subject of this section. The derivations are quite extensive and consequently, the majority of these will be omitted. The interested reader is referred to the respective authors which are cited for the derivations. Anderson [2] is chosen as the source for the equation of mass conservation, while White [27] is chosen for the momentum equation. For the energy equation, an alternative to the standard form is that of considering the total energy $(e + V^2/2)$ as the transported quantity. Anderson [1] provides the derivations for the total energy equation and is consequently chosen as the source. Note that the expressions obtained in the following sections will be general in the sense that they are valid for compressible, viscous and unsteady flows.

3.2.1 Conservation of Mass

Considering an infinitesimal volume, the time rate of change of mass inside the element volume equals the net mass flow entering the element volume by means of convection across the surface boundary. Considering the velocity components in a cartesian coordinate system as;

$$\boldsymbol{V} = [u, v, w]^T \tag{3.16}$$

Furthermore, the vector gradient operator is defined as;

$$\boldsymbol{\nabla} = \left[\frac{\partial}{\partial x}, \frac{\partial}{\partial y}, \frac{\partial}{\partial z}\right]^T \tag{3.17}$$

The equation of mass conservation yields the following form;

$$\frac{\partial \rho}{\partial t} + \frac{\partial}{\partial x}(\rho u) + \frac{\partial}{\partial y}(\rho v) + \frac{\partial}{\partial z}(\rho w) = 0 \tag{3.18}$$

or more compact, using the above notations;

$$\frac{\partial \rho}{\partial t} + \boldsymbol{\nabla} \cdot (\rho \boldsymbol{V}) = 0 \tag{3.19}$$

3.2.2 Conservation of Momentum

The treatment of fluid momentum follows from Newton's Law, which, in its appropriate form, states that the time rate of change of momentum inside the element equals the net flux of momentum into the domain. Summing the forces acting on a control volume results in the following expression;

$$\sum \boldsymbol{F} = \frac{\partial}{\partial t}\left(\int_{CV} \boldsymbol{V}\rho dV\right) + \sum(\dot{m}\boldsymbol{V})_{out} - \sum(\dot{m}\boldsymbol{V})_{in} \tag{3.20}$$

Considering an infinitesimal volume, this reduces to a derivate term according to;

$$\frac{\partial}{\partial t}(\boldsymbol{V}\rho dV) \approx \frac{\partial}{\partial t}(\rho\boldsymbol{V})dxdydz \tag{3.21}$$

Elaborating the flux terms, introducing the gravitational body force vector in the downward direction $g_z = -g$ and taking into account surface forces arising from pressure and shear stresses acting on the control volume boundary surfaces yields the full expressions for momentum conservation in the three principal directions;

$$\rho g_x - \frac{\partial p}{\partial x} + \frac{\partial \tau_{xx}}{\partial x} + \frac{\partial \tau_{yx}}{\partial y} + \frac{\partial \tau_{zx}}{\partial z} = \rho\left(\frac{\partial u}{\partial t} + u\frac{\partial u}{\partial x} + v\frac{\partial u}{\partial y} + w\frac{\partial u}{\partial z}\right) \tag{3.22}$$

$$\rho g_y - \frac{\partial p}{\partial y} + \frac{\partial \tau_{xy}}{\partial x} + \frac{\partial \tau_{yy}}{\partial y} + \frac{\partial \tau_{zy}}{\partial z} = \rho\left(\frac{\partial v}{\partial t} + u\frac{\partial v}{\partial x} + v\frac{\partial v}{\partial y} + w\frac{\partial v}{\partial z}\right) \tag{3.23}$$

$$\rho g_z - \frac{\partial p}{\partial z} + \frac{\partial \tau_{xz}}{\partial x} + \frac{\partial \tau_{yz}}{\partial y} + \frac{\partial \tau_{zz}}{\partial z} = \rho\left(\frac{\partial w}{\partial t} + u\frac{\partial w}{\partial x} + v\frac{\partial w}{\partial y} + w\frac{\partial w}{\partial z}\right) \tag{3.24}$$

Introducing the following notation for the viscous shear stresses;

$$\boldsymbol{\tau}_{xy} = \begin{bmatrix} \tau_{xx} & \tau_{yx} & \tau_{zx} \\ \tau_{xy} & \tau_{yy} & \tau_{zy} \\ \tau_{xz} & \tau_{yz} & \tau_{zz} \end{bmatrix} \tag{3.25}$$

and the material (substantial) derivative;

$$\frac{D}{Dt} = \frac{\partial}{\partial t} + u\frac{\partial}{\partial x} + v\frac{\partial}{\partial y} + w\frac{\partial}{\partial z} \tag{3.26}$$

$$\frac{D}{Dt} = \frac{\partial}{\partial t} + (\boldsymbol{V}\cdot\boldsymbol{\nabla}) \tag{3.27}$$

a more compact form of the momentum conservation equations is obtained;

$$\rho\boldsymbol{g} - \boldsymbol{\nabla}p + \boldsymbol{\nabla}\cdot\boldsymbol{\tau}_{xy} = \rho\frac{D\boldsymbol{V}}{Dt} \tag{3.28}$$

3.2.3 Conservation of Energy

The differential equation of energy conservation resulting from selection of the total energy $(e + V^2/2)$ as the transported quantity, stems from the following balance consideration [1];

$$E_1 = E_2 + E_3 \tag{3.29}$$

where

- E_1: Rate of energy change inside element
- E_2: Net flux of heat into element
- E_3: Rate of work done on element due to pressure and shear stress forces acting on boundary surface

Following the derivations [1] of the individual terms of Equation 3.29, the energy conservation equation is obtained;

$$\rho\frac{D(e+V^2/2)}{Dt} = \rho\dot{q} + \frac{\partial}{\partial x}\left(K\frac{\partial T}{\partial x}\right) + \frac{\partial}{\partial y}\left(K\frac{\partial T}{\partial y}\right) + \frac{\partial}{\partial z}\left(K\frac{\partial T}{\partial z}\right) - \boldsymbol{\nabla}\cdot p\boldsymbol{V} + \frac{\partial(u\tau_{xx})}{\partial x} + \\ + \frac{\partial(u\tau_{yx})}{\partial y} + \frac{\partial(u\tau_{zx})}{\partial z} + \frac{\partial(v\tau_{xy})}{\partial x} + \frac{\partial(v\tau_{yy})}{\partial y} + \frac{\partial(v\tau_{zy})}{\partial z} + \frac{\partial(w\tau_{xz})}{\partial x} + \frac{\partial(w\tau_{yz})}{\partial y} + \frac{\partial(w\tau_{zz})}{\partial z} \tag{3.30}$$

This equation shows the inherent difficulty of dealing with viscous flows as compared to inviscid flows, considering the addition of several terms. Furthermore, it translates directly into the CFD model, where the viscous terms contribute to a heating of the fluid. Note that the constitutive assumptions of a Newtonian fluid that will be defined in the following Section 3.2.4, can help to obtain a more explicit form of this equation.

3.2.4 Navier-Stokes Equations

Introducing the constitutive assumption of a generalized Newtonian fluid, one can obtain an alternative form of the momentum equations 3.22-3.24. The viscous shear stress components take the following form, using Einstein notation [3];

$$\tau_{ij} = \mu\left(2S_{ij} - \frac{2}{3}S_{mm}\delta_{ij}\right) \tag{3.31}$$

where the strain-rate tensor is defined as;

$$S_{ij} = \frac{1}{2}\left(\frac{\partial u_i}{\partial x_j} + \frac{\partial u_j}{\partial x_i}\right) \tag{3.32}$$

Expanding these individual terms and inserting them into Equations 3.22-3.24, one obtains the full Navier-Stokes Equations;

$$\rho\frac{Du}{Dt} = \rho g_x - \frac{\partial p}{\partial x} + \frac{\partial}{\partial x}\left(-\frac{2}{3}\mu\left[\frac{\partial u}{\partial x} + \frac{\partial v}{\partial y} + \frac{\partial w}{\partial z}\right] + 2\mu\frac{\partial u}{\partial x}\right) + \frac{\partial}{\partial y}\left(\mu\left[\frac{\partial u}{\partial y} + \frac{\partial v}{\partial x}\right]\right) + \frac{\partial}{\partial z}\left(\mu\left[\frac{\partial u}{\partial z} + \frac{\partial w}{\partial x}\right]\right) \tag{3.33}$$

$$\rho\frac{Dv}{Dt} = \rho g_y - \frac{\partial p}{\partial y} + \frac{\partial}{\partial y}\left(-\frac{2}{3}\mu\left[\frac{\partial u}{\partial x} + \frac{\partial v}{\partial y} + \frac{\partial w}{\partial z}\right] + 2\mu\frac{\partial v}{\partial y}\right) + \frac{\partial}{\partial x}\left(\mu\left[\frac{\partial u}{\partial y} + \frac{\partial v}{\partial x}\right]\right) + \frac{\partial}{\partial z}\left(\mu\left[\frac{\partial v}{\partial z} + \frac{\partial w}{\partial y}\right]\right) \tag{3.34}$$

$$\rho\frac{Dw}{Dt} = \rho g_z - \frac{\partial p}{\partial z} + \frac{\partial}{\partial z}\left(-\frac{2}{3}\mu\left[\frac{\partial u}{\partial x} + \frac{\partial v}{\partial y} + \frac{\partial w}{\partial z}\right] + 2\mu\frac{\partial w}{\partial z}\right) + \frac{\partial}{\partial x}\left(\mu\left[\frac{\partial u}{\partial z} + \frac{\partial w}{\partial x}\right]\right) + \frac{\partial}{\partial y}\left(\mu\left[\frac{\partial v}{\partial z} + \frac{\partial w}{\partial y}\right]\right) \tag{3.35}$$

Only a limited number of analytical solutions to these equations are available [27], yet this is the basis of modern CFD modelling, where these expressions are discretized on fine meshes and solved for on a cellular level. When extending to turbulence modelling, these equations often employ a one- or two-equation turbulence model that depicts the transport of turbulent quantities.

3.3 Shock Relations

The approach to deriving relations that depict the behavior of normal and oblique shock waves start in recognizing the fundamental, governing laws of nature - the preservation of mass, momentum and energy. As is recognized from following the full derivations [2], oblique shock waves only differ from normal shock waves in the sense that they are more general, meaning that it is only the upstream velocity component normal to the shock that determines the wave strength and the changes of properties across. Hence, an oblique shock wave includes a velocity component parallel to the shock wave which remains constant due to the preservation of momentum across. Figure 3.1 illustrates the characteristic angles as well as the Mach number evolution over an oblique shock wave.

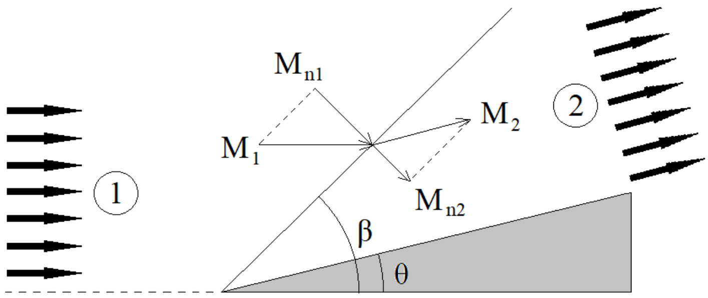

Figure 3.1: *Illustration of characteristic angles as well as Mach number evolution over an oblique shock wave.*

The conservation equations 3.3-3.5 using a gross-effect evaluation as well as the expressions for the speed of sound 3.8-3.9 are here reiterated while it is assumed that the changes occur across a shock wave.

$$\rho_1 V_1 = \rho_2 V_2 \tag{3.36}$$

$$p_1 + \rho_1 V_1^2 = p_2 + \rho_2 V_2^2 \tag{3.37}$$

$$h_1 + \frac{V_1^2}{2} = h_2 + \frac{V_2^2}{2} \tag{3.38}$$

$$a = \frac{V}{M} = \sqrt{\frac{\gamma p}{\rho}} \tag{3.39}$$

$$a = \sqrt{\gamma RT} \tag{3.40}$$

Performing some cumbersome algebra while using these equations as well as the material equations from Section 3.1, the Mach number downstream of a normal shock wave can be written as a function of the upstream Mach number as follows;

$$M_2^2 = \frac{1 + [(\gamma - 1)/2]M_1^2}{\gamma M_1^2 - (\gamma - 1)/2} \tag{3.41}$$

This relation shows that, considering a calorically perfect gas, the downstream Mach number is only a function of the upstream Mach number, which will prove to be a very powerful parameter. The conservation equations 3.3-3.5 along with the equation of state 3.2 lead to the following expressions relating to the thermodynamic property changes across normal shock waves;

$$\frac{p_2}{p_1} = 1 + \frac{2\gamma}{\gamma + 1}(M_1^2 - 1) \tag{3.42}$$

$$\frac{\rho_2}{\rho_1} = \frac{(\gamma + 1)M_1^2}{2 + (\gamma - 1)M_1^2} \tag{3.43}$$

$$\frac{T_2}{T_1} = \frac{p_2}{p_1}\frac{\rho_1}{\rho_2} \tag{3.44}$$

As previously stated, the oblique shock wave behaves in the same way as the normal shock wave, with the exception of the addition of a tangential velocity component that is preserved. Hence, to consider property changes across an oblique shock wave, it is sufficient to replace the Mach numbers M_1 and M_2 with the corresponding normal components M_{n1} and M_{n2} in Equations 3.42-3.44. These are simply defined by use of the characteristic angles as;

$$M_{n1} = M_1 \sin\beta \tag{3.45}$$

$$M_{n2} = M_2 \sin(\beta - \theta) \tag{3.46}$$

The relation between the downstream and upstream normal Mach number component takes the form;

$$M_{n2}^2 = \frac{M_{n1}^2 + [2/(\gamma - 1)]}{[2\gamma/(\gamma - 1)]M_{n1}^2 - 1} \tag{3.47}$$

Finally, an essential relation when it comes to the design of external compression ramps is the θ-β-M relation, which relates the upstream Mach number to the deflection angle θ of the ramp and the resulting oblique shock wave angle β;

$$\tan\theta = 2\cot\beta \left[\frac{M_1^2 \sin^2\beta - 1}{M_1^2(\gamma + \cos 2\beta) + 2} \right] \tag{3.48}$$

Looking at Equation 3.48, as often is the case, the upstream Mach number and the ramp deflection angle is given. In this case it is quite cumbersome to analytically solve for the shock wave angle. An iterative approach may be used to solve for this angle with a desired level of accuracy.

3.4 Area-Velocity Relation

The conceptual intake considered in this project is of the rectangular kind, where the intake interior profile can be simplified as being constant in the z-direction as depicted by Figure 4.1. It could therefore prove tempting to consider the flow two-dimensional, or even neglect the transverse flow and consider the flow to be axial and one-dimensional. Any of these assumptions would be erroneous. Experimental wind tunnel tests as well as Reynolds-Averaged Navier-Stokes (RANS) simulations have proved the flow in supersonic inlets to be highly three-dimensional [16], which also extends to the rectangular intake described above under symmetric free-stream conditions. Nevertheless, when considering the internal part of the intake, an assumption that leads to some interesting analytical features is the approximation of quasi one-dimensional flow. This approximation is a relaxation to the assumption of one-dimensional, constant-area flow. Here, the cross-sectional flow area is allowed to gradually vary in the axial direction, and the transverse velocity components are neglected to enable all flow properties to vary in the axial direction only.

With the assertion of quasi one-dimensional flow, a differential approach to the conservation equations in an internal duct yields the following expressions for conservation of mass, momentum and energy, respectively;

$$d(\rho u A) = 0 \tag{3.49}$$

$$dp = -\rho u du \tag{3.50}$$

$$dh + udu = 0 \tag{3.51}$$

Assuming isentropic flow, the speed of sound can be written as;

$$a^2 = \frac{dp}{d\rho} = \left(\frac{\partial p}{\partial \rho}\right)_s \tag{3.52}$$

Performing some algebra while combining these equations and neglecting second-order terms involving products of differentials, it can be shown that;

$$\frac{dA}{A} = (M^2 - 1)\frac{du}{u} \tag{3.53}$$

This result, also known as the *Area-Velocity Relation*, contains some striking features on the characteristics of intake duct flow. The identification of 4 cases is made as follows;

1. As $M \to 0$, the limit pertaining to incompressible, constant-density flow is approached and the familiar continuity equation is obtained, $Au = \text{const}$.

2. In the range $0 \leq M \leq 1$, an area increase is associated with a decrease in velocity and vice versa.

3. For supersonic flow $M > 1$, an area increase is associated with an increase in velocity, and vice versa.

4. For sonic flow $M = 1$, Equation 3.53 yields $dA/A = 0$, which corresponds to a minimum or maximum of flow area, where the former is the only physically sound solution. Hence, sonic conditions will always be attained at the aerodynamic throat section.

The conclusion of this discussion that applies to the studied intake is that a convergent-divergent duct is required in order for air to compress isentropically from supersonic to subsonic speeds, where sonic flow is attained at the throat. Another powerful parameter governing the behavior of the divergent section is the back pressure of the subsonic diffuser. At a certain balanced value, the flow will become choked at the throat, meaning that no further mass flow can be achieved my means of lowering the back pressure, and the flow throughout the divergent section will be subsonic. This is governed by Equation 3.53. Should the back pressure be lowered further a normal shock will appear in the divergent section, which requires the flow to accelerate to supersonic speeds after the throat section. The position of this shock will be controlled by the back pressure.

3.5 Area-Mach Number Relation

When expanding on the notion of continuity, another interesting relation can be obtained that relates the Mach number in an arbitrary duct to the evolution of the cross-sectional area. Furthermore, as this Mach number distribution is obtained, one can calculate the isentropic values of static properties as described below. Once again, quasi one-dimensional and isentropic flow is assumed. Applying conservation of mass at an arbitrary location in the duct and relating to sonic (throat) conditions, denoted with a superscript $*$, yields;

$$\rho^* V^* A^* = \rho V A \tag{3.54}$$

Per definition, $u^* = a^*$, and Equation 3.54 becomes;

$$\frac{A}{A^*} = \frac{\rho^*}{\rho}\frac{a^*}{V} = \frac{\rho^*}{\rho_0}\frac{\rho_0}{\rho}\frac{a^*}{V} \tag{3.55}$$

At this point, one can utilize the expression for stagnation density, Equation 3.13, and assume $M = 1$ to obtain;

$$\frac{\rho_0}{\rho^*} = \left(\frac{\gamma - 1}{2}\right)^{1/(\gamma-1)} \tag{3.56}$$

Considering the energy equation for one-dimensional, adiabatic flow, it can be shown [2] that;

$$\left(\frac{V}{a^*}\right)^2 = M^{*2} = \frac{\frac{\gamma+1}{2}M^2}{1 + \frac{\gamma-1}{2}M^2} \tag{3.57}$$

Combining Equations 3.55, 3.56, 3.57 and 3.13, the area-Mach number relation is obtained as follows;

$$\left(\frac{A}{A^*}\right)^2 = \frac{1}{M^2}\left[\frac{2}{\gamma + 1}\left(1 + \frac{\gamma - 1}{2}M^2\right)\right]^{(\gamma+1)/(\gamma-1)} \tag{3.58}$$

As stated above, this relation can be used to obtain the Mach number variation in a duct as a function of the ratio of the local duct area to the sonic throat area. As this information is gained, it is possible to calculate the values of static temperature, pressure and density according to Equations 3.10, 3.12 and 3.13. It is reiterated that the applicability of this relation depends on the validity of the approximation of isentropic, quasi-one dimensional flow. Nevertheless, it is a practical tool to preliminary design as, given a capture area of the intake and a free stream Mach number, one can approximate the required throat area.

3.6 Compressible Mass Flow Equation

At low Mach numbers, where density changes occuring in the flow are negligible and it can be assumed to be incompressible, mass flow is easily expressed as;

$$\dot{m} = \rho V A \tag{3.59}$$

where A is the area that is perpendicular to the flow. However, when exceeding Mach numbers of $M = 0.3$, compressibility has to be taken into consideration and density changes can no longer be neglected [8]. Due to density changes resulting from pressure losses, velocity changes can occur in a constant-area duct in high speed flows [25]. Hence, total properties are invoked and the mass flow for a compressible flow is expressed using Equations 3.59, 3.10, 3.12 and 3.13. Neglecting the derivations for the sake of conciseness, this equation takes the following form;

$$\frac{\dot{m}\sqrt{C_p T_0}}{A p_0} = \frac{\gamma}{\sqrt{\gamma - 1}} M \left[1 + \frac{\gamma - 1}{2} M^2\right]^{-\frac{1}{2}\left(\frac{\gamma+1}{\gamma-1}\right)} \tag{3.60}$$

Note that the assumption of an ideal gas is implicitly stated through the use of the equations for total properties. Finally, the corrected mass flow, corresponding to the mass flow which would be obtained for ambient conditions at sea level can be expressed as follows;

$$\dot{m}_{corr} = \dot{m}\sqrt{\left(\frac{T_0}{T}\right) / \left(\frac{p_0}{p}\right)} \tag{3.61}$$

These equations are used to calculate the intake capture area that is required to sustain a certain mass flow to the engine at the design Mach number, given ambient conditions corresponding to a certain altitude. Combining these expressions with Equation 3.7, the required capture area can be solved for according to;

$$A_\infty = \frac{\dot{m}_{corr}\sqrt{RT}}{Mp\sqrt{\gamma}} \left[1 + \frac{\gamma - 1}{2} M^2\right]^{-\frac{1}{2}\left(\frac{\gamma+1}{\gamma-1}\right)} \tag{3.62}$$

Knowing that the intake features a rectangular inlet area and assuming that $A_{\infty,ss}$ is the value of this area at the small scale and that the required large-scale value is $A_{\infty,ls}$, the corresponding scale transformation factor SF can be calculated as;

$$SF = \sqrt{\frac{A_{\infty,ls}}{A_{\infty,ss}}} \tag{3.63}$$

The dimensionless parameter relating to mass flow in this study is the capture area ratio, or mass flow ratio MFR, expressed as a ratio of the mass flow entering the engine face to the mass flow swallowed by the intake capture area;

$$MFR = \frac{\dot{m}_e}{\dot{m}_\infty} \tag{3.64}$$

3.7 Aerodynamic Forces

The prediction of aerodynamic forces acting on a submerged body has been a centralized subject for aerodynamicists throughout the centuries. This concerns the area of compressible flow in particular, as the prediction of lift and drag forces on bodies in all Mach number domains is at the heart of the subject of Aerodynamics [2]. The mechanism by which an aerodynamic force is transmitted from a fluid to a surface stems from two sources: fluid pressure and fluid shear stress acting on the surface, where the latter arises from the viscosity of the fluid. By common practice, a decomposition of the resulting force vector is made into components of drag and lift, that act parallel and perpendicular to the free stream flow direction, respectively. The mathematical definition of the force resulting from pressure and shear stress follows [2];

$$\mathbf{F} = \oint_S p\mathbf{n}dS + \oint_S \tau\mathbf{m}dS \tag{3.65}$$

where $\mathbf{n}$ and $\mathbf{m}$ are unit vectors perpendicular and parallel to the surface element dS, respectively. Since the free-stream flow direction coincides with the axial direction of the intake, the drag and lift are acting in the x- and y-directions, respectively. Hence, the decomposition of the force vector into drag and lift are made as follows;

$$D = \oint_S p n_x dS + \oint_S \tau m_x dS \tag{3.66}$$

$$L \approx \oint_S p n_y dS \tag{3.67}$$

For most practical aerodynamic shapes, it is mainly the surface pressure distribution that generates lift [2], hence the neglect of the shear stress contribution in the expression for lift. Note that also the shear stress contribution to the drag is in general small. However, it is included in the expression for drag seeing as this assumption will be subject to validation later on as the results of the study are presented. It is safe to assume that the generated lift of the intake will be small in comparison to that of the aircraft wings, thus the primary interest related to the lift will be that of determining the pitch torque it induces on the aircraft body. Selecting an arbitrary pair of coordinates (x_{PT}, y_{PT}) in the intake, the pitch torque about the z-axis at this location becomes;

$$P \approx \oint_S pn_y(x - x_{PT})dS + \oint_S pn_x(y - y_{PT})dS \tag{3.68}$$

The drag is related to the net propulsion force F of the aircraft according to [18];

$$F = F_T - D_{add} - D_{ext} \tag{3.69}$$

where F_T is the net thrust generated by the engine and the total drag is divided into additive and external contributions. There exists many different classifications of drag sources, depending on the application. Malan & Brown [14] divides the drag acting on the intake into spillage, wave and profile contributions. Spillage drag is defined as the drag induced by mass flow that is spilled on the outside of the intake, thus it is present when the engine mass flow demand is less than the maximum that can be swallowed by the intake at the pertinent Mach number. Wave drag is defined as the drag increase due to the presence of localized or global supersonic flow. Finally, profile drag is divided into skin friction and form drag, where the former is due to the viscous shear stress acting on the intake and the latter is due to the shape of the intake. In contrast, as previously stated, Mount [17] divides the total drag into additive and external contributions as depicted by Equation 3.69. The recognized definition of additive drag [14] [17] is the force acting on the stream tube of air entering the intake by the surrounding atmosphere.

As the purpose of this study is to gain knowledge into how the key parameters of free stream Mach number, intake back pressure and mass flow affect the total drag rather than to perform a benchmarking of the intake, a more relaxed classification will be adopted. A large emphasis of the interest is put on how the mass flow spillage affects the drag, thus the drag will be divided into internal and external contributions. The internal contribution is from the forces generated by the mass flow that ultimately enters the engine, acting on the ramp, internal duct and subsonic diffuser section. The external force contribution stems from the exterior surfaces of the intake, including those of the bleed channel. In the case of the intake studied in this project, two different sources of mass flow spillage exists. Firstly, when oblique shock waves forming at the external ramp are not swallowed by the intake, a portion of the capture area mass flow will be diverted over the lip wedge. Secondly, a portion of the interior flow is redirected into the bleed channel by means of expansion over the trailing edge of the ramp or re-circulation in the throat section. Since mass flow spillage over the lip wedge and in the bleed channel are expected to redistribute the pressure on these exterior surfaces, the mass flow spillage is represented implicitly as the relative change of external drag.

$$D = D_{ext} + D_{int} \tag{3.70}$$

Finally, the non-dimensionalized drag coefficients are obtained by means of division with the product of free-stream, dynamic pressure and the projected, cross-sectional area of the intake;

$$C_{D,ext} = \frac{D_{ext}}{(1/2)\rho_\infty v_\infty^2 A_\infty} \tag{3.71}$$

$$C_{D,int} = \frac{D_{int}}{(1/2)\rho_\infty v_\infty^2 A_\infty} \tag{3.72}$$

$$C_D = C_{D,int} + C_{D,ext} \tag{3.73}$$

3.8 Ideal Brayton Cycle

The analysis of thermodynamic cycles prove very useful to the determination of efficiencies relating to the work output [13] of the propulsion unit. However, the current objective is merely to gain a conceptual understanding of how the static pressure increase across the compression unit is necessary to gain a positive net work output in the propulsion unit as a whole. A simplified, schematic view of the *Ideal Brayton Cycle* is shown in Figure 3.2. Furthermore, this cycle is represented in a *h-s* and a *T-s* graph in Figure 3.3.

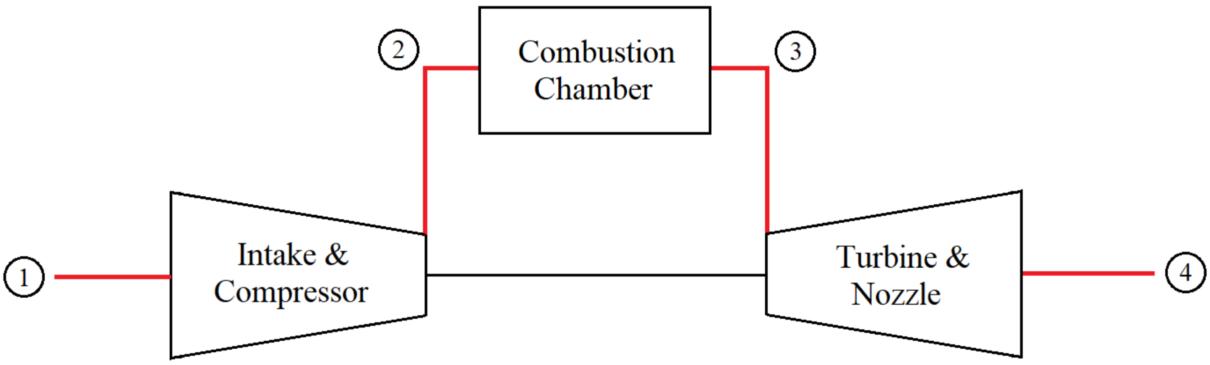

Figure 3.2: *Simplified view of the jet engine cycle.*

The individual steps of the simplified cycle are identified as follows;

- 1 → 2: Isentropic compression.
- 2 → 3: Isobaric heat addition.
- 3 → 4: Isentropic expansion.
- 4 → 1: Isobaric heat rejection.

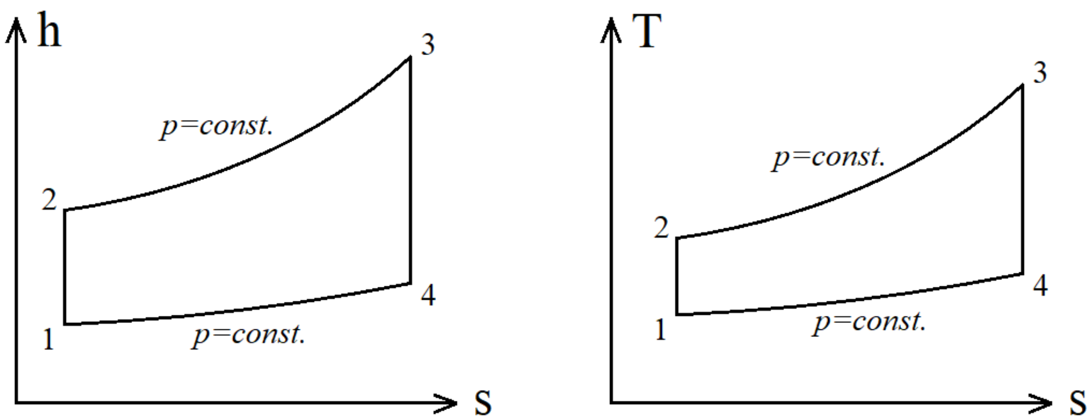

Figure 3.3: *Ideal Brayton Cycle represented in a h-s and T-s graph.*

Combining the first and second law of thermodynamics, it can be shown [2] that;

$$Tds = dh - vdp \tag{3.74}$$

Consequently, as isobaric processes are considered, the following relation is obtained [13];

$$\left(\frac{\partial h}{\partial s}\right)_p = \frac{dh}{ds} = T \tag{3.75}$$

It is apparent that the slope of the isobaric curves in the h-s graph is the temperature. As is the case in this study, a calorically perfect gas is considered, leading to Equation 3.1. Hence, the isentropic increase of enthalpy in the compression phase implicitly gives an increase of temperature, with the scale factor C_p. This is the reason that the two isobars in the depicted Brayton cycle diverge, due to the increased slope at a higher temperature. The net work output of the propulsion unit is expressed as;

$$W = \Delta h_{3\to4} - \Delta h_{1\to2} = C_p(\Delta T_{3\to4} - \Delta T_{1\to2}) \tag{3.76}$$

Due to the divergence of isobars, it is apparent that;

$$\Delta h_{3\to4} > \Delta h_{1\to2} \tag{3.77}$$

leading to a positive net work output as defined by Equation 3.76. This is the fundamental reason that a net positive work output can be drawn from an engine with an integrated compression unit. As a direct consequence of the ideal gas law, Equation 3.2, it is also realized that a higher pressure ratio in the compression unit leads to a higher divergence of isobars, which can be shown to ultimately increase the cycle efficiency of the propulsion unit [13].

3.9 Jet Propulsion

The propulsion of an aircraft stems from sources, one static and one dynamic in nature. The static contribution is provided from the net force exerted on the aircraft due to pressure and shear stress distributions acting on the surface. When dealing with the relatively low viscosity of air, the shear stress contribution is very small as compared to that of pressure [2], hence it can be neglected. Ultimately, the static contribution to the propulsion of the aircraft is that of a net pressure force being exerted on the submerged body. The dynamic contribution to the thrust can be derived from the integral form of the momentum equations outlined in Section 3.2.2, and is a direct result of Newton's laws of motion. As mass enters and exits a propulsion unit, it will experience a change of momentum flux as a result of the heat addition in the combustion chamber. This change of momentum flux will result in a force being exerted on the engine in the direction opposed to that of the mass flow, contributing to the propulsion of the aircraft. Ultimately, the uninstalled momentum thrust equation takes the following form [2];

$$F = (\dot{m}_N V_N - \dot{m}_\infty V_\infty) + (p_N - p_\infty)A_\infty \tag{3.78}$$

Note that, using the above sign convention, the force is defined as positive in the direction of aircraft motion. The first term corresponds to the momentum thrust and the second to the pressure thrust exerted on the aircraft. Seeing as the effects of the pressure distribution are known through the total drag, calculated with Equation 3.66, this term can be replaced in the above equation to obtain;

$$F = (\dot{m}_N V_N - \dot{m}_\infty V_\infty) - D \tag{3.79}$$

Once again, the shear stress contribution seen in Equation 3.66 is neglected due to its small influence. As the momentum thrust requires knowledge about the work input by means of heat addition in the combustion chamber of the engine unit, the momentum thrust can be obtained through engine specifications.

4 Results

In this chapter, the results of the geometry creation as well as the validation and parametric studies will be presented, in the mentioned order. Considering that the mesh convergence study is a part of the validation study, it will be included in Section 4.2 where the results of the validation study are presented. Due to the confidential nature of the results, exact geometries, boundary conditions and numerical results will not be subject to disclosure. In the forthcoming sections, all geometries have been distorted, boundary conditions are represented algebraically and numerical results are scaled. Naturally, this will mean a compromise of the results to some extent, after which the performance in terms of the studied parameters can not be compared to similar intakes investigated in other studies. However, it still allows for a qualitative understanding of how the intake performance depends on the key parameters to be developed.

The numerical results are primarily represented by graphs depicting the global behavior of the intake. To aid in analyzing these results in more detail, flow field visualizations in terms of key quantities of total pressure, static pressure and Mach number distributions inside the intake have been made available as appendices. These illustrations include two different views. One is a profile view of the intake at the symmetry plane, or centralized intake depth coordinate (along the z-axis as depicted in Figure 4.1). The other is an isometric view including the flows in transverse planes at key, axial positions in the intake. The purpose of this latter view is to account for the three-dimensional nature of the flow, which is neglected in the profile view. Furthermore, to clearly illustrate the shock wave patterns residing in the intake for the various flow scenarios, density gradient illustrations have been generated using only the profile view. Please note at this stage that the density gradient illustrations are based on instantaneous rather than time-averaged distributions. This is to further highlight the complex flow structures by avoiding more diffuse patterns associated to mixing in time. Finally, due to the extent of the study, a vast number of these illustrations have been generated and only key cases will be included to elaborate on the general behavior, for the sake of brevity. This concerns both the validation and parametric study.

4.1 Geometry Creation

Following the procedure outlined in Section 2.1, the geometry of the primary intake was created and exported to mesh creation. This primary intake, which was the subject of the validation study, was then enlarged uniformly by a scaling factor as discussed in Section 2.3.3. On the basis of this enlarged intake, an alternate geometry was created, representing an alternative ramp shape. These two large-scale geometries were the basis of the subsequent parametric study and are presented in Figures 4.1-4.2 below.

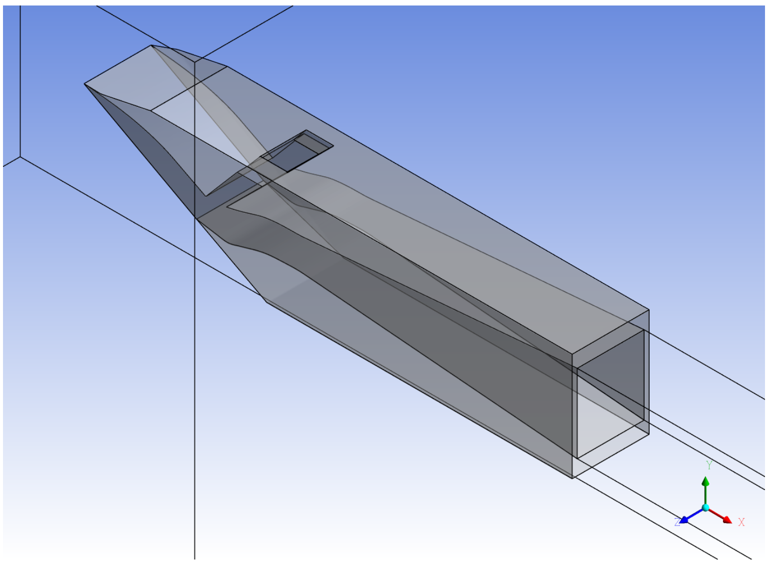

Figure 4.1: *Isometric view of intake geometry.*

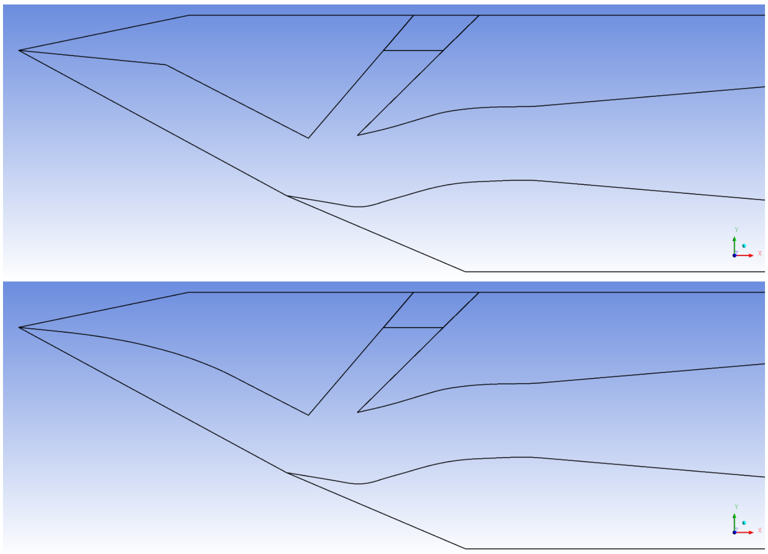

Figure 4.2: *Profile views of intake ramp geometry configurations. The upper geometry is the discrete-ramp (DR) configuration while the lower is the reference, continuous-curve, isentropic-ramp (IR) configuration.*

4.2 Results of Validation Study

The scope of the validation study that was carried out was the generation of performance curves relating to mass flow and total pressure recovery using the obtained CFD model. This global behavior was mapped as a function of the intake back pressure for a set of different Mach numbers. The operating conditions that were implemented in the study were defined in two levels. Firstly, 4 distinctly different free stream Mach numbers were implemented. Secondly, for each of these, a back pressure variation was implemented such that 3-5 distinctly different levels of back pressure were modelled, depending on the applicable range in the model. Table 4.1 is used to illustrate the scope of the study in terms of the performed simulations. For the set of Mach numbers, $\{M_{V,1}, M_{V,2}, M_{V,3}, M_{V,4}\}$, listed in increasing order, the index V is used to denote implementation in the validation study. Furthermore, back pressure levels are denoted $p_{m,n}$, where m relates to the Mach number in increasing order and n is the index of increasing order of back pressure.

As these performance curves were generated, they were compared to the corresponding curves obtained in the wind tunnel tests. Finally, the level of accordance between these two sets was assessed and deviations were analyzed. To not only validate the fidelity of the CFD model but also the robustness of the mesh, a mesh dependency study was carried out to evaluate the dependency of the results on the spatial resolution of the mesh that was employed in the model. The complete procedure is outlined in more detail in Chapter 2.

4.2.1 Mass Flow and Total Pressure Recovery

The characteristic intake performance curves, described in Section 4.2, are illustrated in Figures 4.3-4.6 below. For the sake of comparison between Mach number cases, note that the axes have the same numerical ranges in all the Figures. Two things are important to take into consideration at this stage when examining these graphs. Firstly, given a Mach number, by increasing the back pressure one moves from the lower end of the respective curve to the upper end. Three characteristic regions of these curves are identified, and will be defined in more detail below as they are referenced. They are best exemplified by Figure 4.4. The first is the *subcritical* operating range, which corresponds to the horizontal, upper part of the curve. The second is the *supercritical* operating range, corresponding to the vertical, lower part of the curve. The critical operating point is defined in the region of transition between these two ranges. In short, this attribute indicates the positioning of the sonic transition. At the critical point, the sonic transition occurs in the aerodynamic throat section, while it occurs upstream and downstream of this location in the subcritical and supercritical range, respectively. Finally, as the objective was to reproduce the curves obtained from wind tunnel testing rather than the individual testing points, of which the levels of intake back pressure were unknown, there is no correspondence between points on the CFD curves and points on the wind tunnel testing curves.

Table 4.1: Simulations of validation study.

Case	Comments	
$M_{V,1}$	Off-design operation, $M_{V,1} < M_d$	
$p_{1,1}$	Supercritical range	
$p_{1,2}$	Supercritical range	
$p_{1,3}$	Supercritical range	
$p_{1,4}$	Critical point	
$p_{1,5}$	Subcritical range	
$M_{V,2}$	Off-design operation, $M_{V,2} < M_d$	
$p_{2,1}$	Supercritical range	
$p_{2,2}$	Supercritical range	
$p_{2,3}$	Supercritical range	
$p_{2,4}$	Critical point	
$M_{V,3}$	On-design operation, $M_{V,3} \approx M_d$, chosen for mesh convergence study	
	Coarse mesh	*Fine mesh*
$p_{3,1}$	Supercritical range	Supercritical range
$p_{3,2}$	Supercritical range	Supercritical range
$p_{3,3}$	Supercritical range	Supercritical range
$p_{3,4}$	Supercritical range	Supercritical range
$p_{3,5}$	Critical point	Critical point
$M_{V,4}$	Off-design operation, $M_{V,4} > M_d$	
$p_{4,1}$	Supercritical range	
$p_{4,2}$	Supercritical range	
$p_{4,3}$	Critical point	

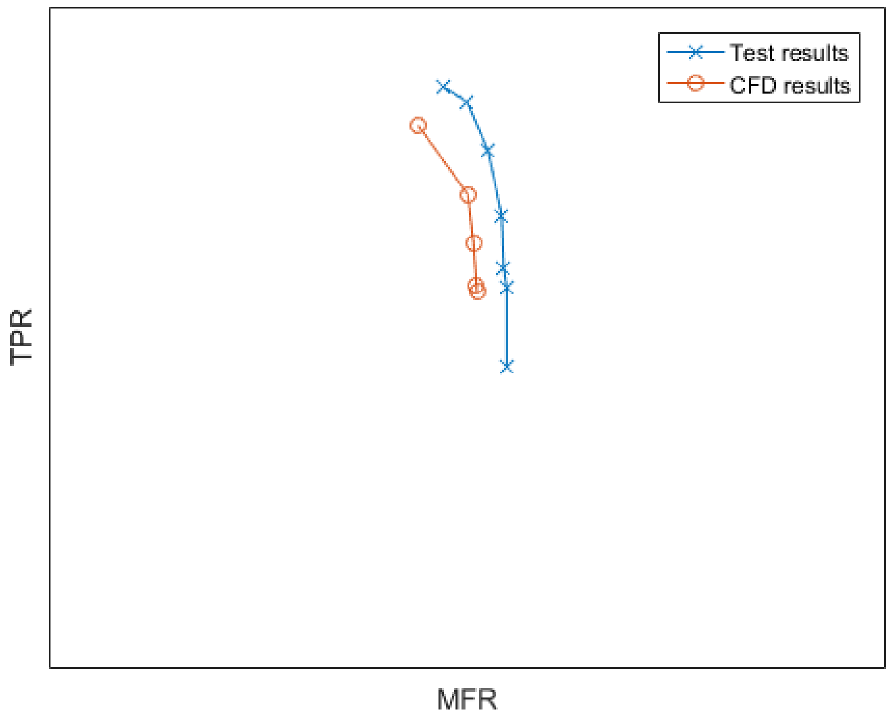

Figure 4.3: *Mass flow versus total pressure recovery for small-scale intake, $M = M_{V,1}$*

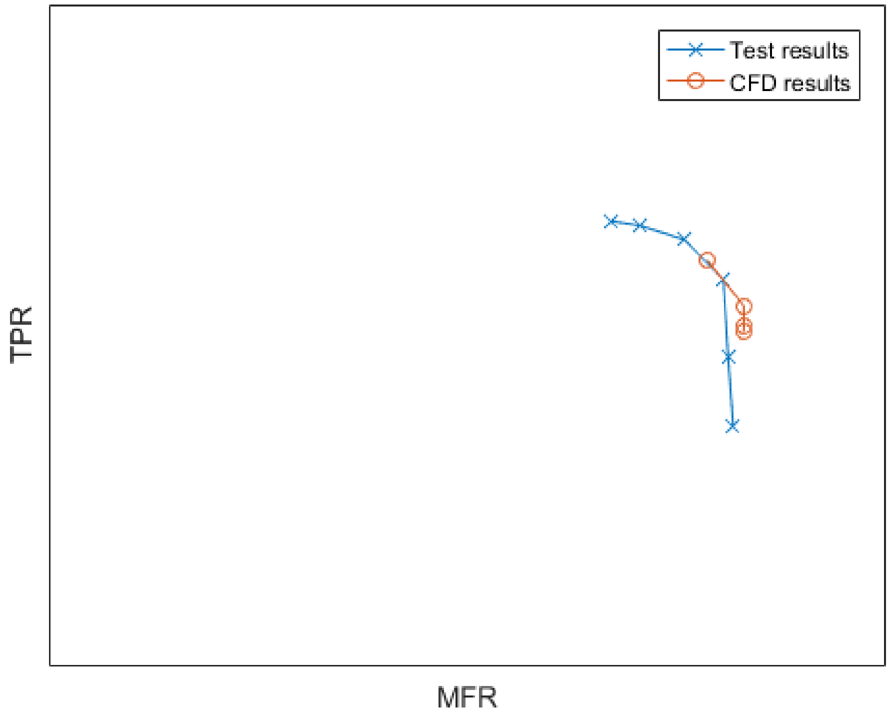

Figure 4.4: *Mass flow versus total pressure recovery for small-scale intake,* $M = M_{V,2}$

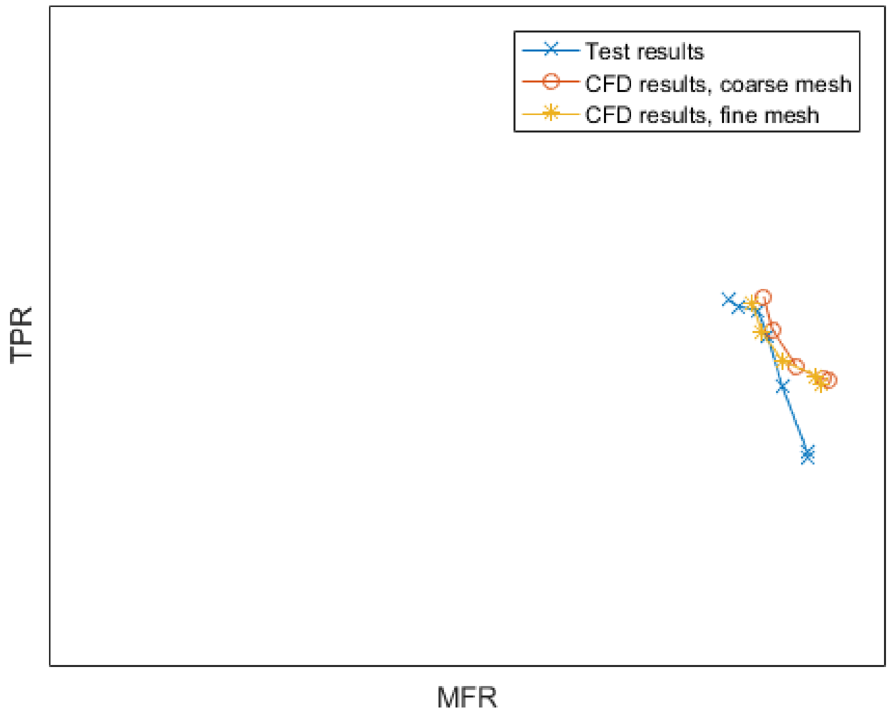

Figure 4.5: *Mass flow versus total pressure recovery for small-scale intake,* $M = M_{V,3}$

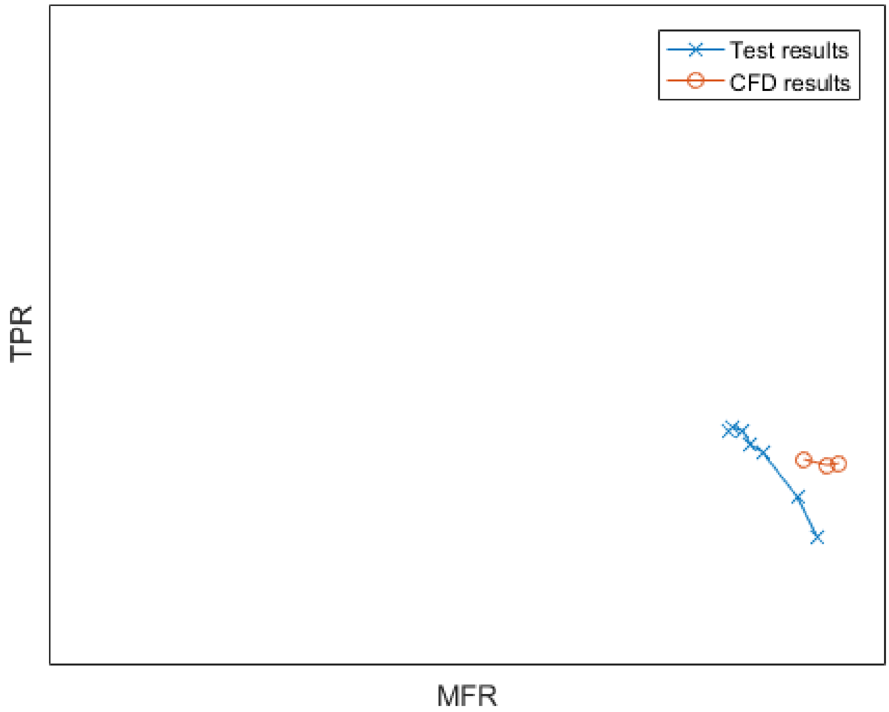

Figure 4.6: *Mass flow versus total pressure recovery for small-scale intake, $M = M_{V,4}$*

Mach $M = M_{V,1}$

At the critical point of operation for the Mach number $M_{V,1}$, exemplified by the flow scenario of Appendix A.1, the back pressure is chosen such that the normal shock terminating the external compression phase is placed in the aerodynamic throat section of the intake. In the external compression phase at this Mach number, two key features are identified. Firstly, the initial oblique shock wave angle is large enough to divert a significant portion of the incoming, capture area mass flow to the outside of the intake. As will be made evident later on, this angle is made smaller as the free-stream Mach number increases. As the angle is made smaller, less mass flow is spilled to the outside and the mass flow swallowed by the intake increases. This signifies the Mach number dependence of the swallowed mass flow, the regulation of the initial oblique shock wave angle as accurately predicted by the theory of Section 3.3. The second feature of the external phase is that the compression, resulting from the continuous flow deflection of the ramp, causes a negligible total pressure loss. This validates the notion of an *isentropic intake*. As the pressurized flow enters the interior of the intake, leaving the trailing edge of the ramp, it expands. This causes an acceleration and a diversion of the boundary layer flow of the ramp into the bleed channel, precisely as intended. Subsequent to the bleed channel section, the terminating normal shock is induced, causing the transition to the subsonic flow of the subsonic diffuser. An interesting feature of this normal shock is that its strength, or intensity, varies across the duct section due to the upstream acceleration fan. Ultimately, the total pressure loss across the normal shock is larger close to the centerbody of the intake. Another consequence of this acceleration fan is that an additional normal shock occurs at the trailing edge of the ramp. As the subsonic flow enters the subsonic diffuser after the terminating normal shock, the flow distortion is kept at a minimum by means of efficient mixing.

When further increasing the intake back pressure, the terminating normal shock is pushed upstream inside the intake, moving the operating point into the subcritical range. As this happens, the mass flow diverted into the bleed channel increases rapidly, beyond the intended levels. This will decrease the intensity of this shock, further increasing the total pressure recovery at the expense of a decrease of mass flow ultimately entering the engine. The subcritical range is exemplified by A.2.

Departing once again from the critical point of operation, the intake back pressure can be decreased to access the supercritical range, as is the case in Appendix A.3. As the overall static pressure increase of the subsonic diffuser is now smaller, the flow is forced to remain supersonic throughout a significant portion of this section. Consequently, the obtained shock wave structure is far more intricate and multiple reflections are observed. An undesired effect of this behavior is the flow separation that occurs inside the subsonic diffuser. This separation is in general initiated at locations of shock wave reflections, as will be observed across the Mach number range. This well-known phenomenon of shock-induced separation is attributed to the rapid pressure increase across shock waves. This disturbance is strong enough to cause a high-momentum, supersonic particle travelling along the subsonic diffuser surface to be redirected by the impulse of the shock wave, causing strong separation and regions of re-circulation to be induced in the wake. The primary outcome of separation in the subsonic diffuser section is that the flow entering the engine face is heavily distorted in terms of velocity and total pressure.

Observing Figure 4.3, it appears that the model is able to predict a wide range of ratios of total pressure recovery, closely resembling the curve of wind tunnel tests. However, a somewhat constant offset of mass flow is observed between the curves. A plausible explanation for this is the placement of the trailing edge of the bleed channel in terms of hardware manufacturing tolerances, combined with the underestimation of the initial and total deflection angle of the ramp in the model, as described in Section 2.1. When studying the general flow at this Mach number (Appendix A), it can be concluded that the amount of mass flow entering the bleed channel is very sensitive to the placement of this edge and the rate of expansion of the flow leaving the ramp.

Mach $M = M_{V,2}$

The increase of the free stream Mach number to a value $M_{V,2}$, slightly below the design Mach number M_d, is made evident by a reduction of the initial oblique shock wave angle. The inclination is such that this shock wave propagates outside the tip of the lip wedge by a small margin, as can be seen by the flow field representing the critical operating point in Appendix B.1. As argued in the previous paragraph, the range of mass flow swallowed by the intake is increased due to this effect. This is observed in Figure 4.4. Another interesting feature of increasing the free stream Mach number is that the effective area of the throat section, terminating the convergent part of the intake, decreases. Having an effective aerodynamic throat area that is smaller than the actual, physical area of the intended throat section, causes the shear layer of the flow leaving the ramp to be ingested by the internal duct. As this happens, mass flow is spilled by means of diffusion across the shear layer and re-circulation into the bleed channel, caused by an adverse pressure gradient. Having a shear layer ingested in the subsonic diffuser section increases the complexity of the flow, compromising the axial uniformity of the flow. This effect is also present at higher Mach numbers.

At a point p_{e2} of supercritical operation, shown in Appendix B.2, the lower overall static pressure increase of the subsonic diffuser forces larger velocities in this section. For the same reasons that were previously discussed while treating a low back pressure case at $M_{V,1}$, separation is induced, causing heavy flow distortion. Upon inspection of the results in Figure 4.4, it can be seen that the range of modelled total pressure recovery is quite narrow as compared to that of the tests. However, the predicted mass flow by the model almost coincide. Furthermore, the total pressure recovery seems to converge towards a minimum value as the back pressure is lowered. Finally, there is no representation of the subcritical range in the model results. Attempts have been made to raise the back pressure levels beyond that of the critical point to access the subcritical range. However, this domain of operation is strongly associated with instability, as the intake will be *unstarted* when the terminating normal shock is pushed upstream to the convergent part of the intake. Hence, no such solutions were obtained that were deemed satisfactory.

Mach $M = M_{V,3}$

As the design Mach number is slightly exceeded by reaching $M_{V,3}$, the initial oblique shock wave of the external compression phase is swallowed by the intake, eliminating mass flow spillage to the exterior of the lip wedge. This Mach number $M_{V,3}$, being the best approximation of the design Mach number M_d, was chosen for the mesh convergence study. The overall results can be seen in Figure 4.5. The same flow features of shear layers, re-circulation, separation and distortion that were discussed in the previous paragraph are present at this Mach number. Furthermore, the same intake back pressure dependency is observed. Hence, the supercritical operating scenario of Appendix C.1 was chosen to highlight the differences of flow fields obtained when using the different meshes. A few distinct tendencies are identified. Firstly, as the wall resolution is increased, the boundary layer thickness increases, made evident by the flow adjacent to the ramp. Secondly, large gradients associated with shock wave structures are better resolved using the fine mesh. Finally, the point of separation along the subsonic diffuser wall moves marginally downstream as the boundary layer modelling is neglected while using a coarse mesh. However, the main observation is that the flow structures and modes remain the same regardless of mesh resolution.

The global results are presented in Figure 4.5. The first observation is that a negligible difference is obtained when using different mesh resolutions, and thus the prediction of mass flow and total pressure recovery can be considered independent of mesh resolution. Secondly, the range of mass flow predicted by the model closely resembles that of the wind tunnel tests. However, just as previously concluded, the total pressure recovery predicted by the model seems to converge in the supercritical range towards a minimum value. This results in an overestimation as compared to the test results.

Mach $M = M_{V,4}$

When increasing the free stream Mach number far beyond the design Mach number M_d, the angle of the initial oblique shock wave is very small. Consequently, as can be seen in Appendix D.1, a portion of the incoming, capture area mass flow is subjected to a very strong normal shock close to the tip of the lip wedge, causing a significant total pressure loss. The resulting flow structure of the intake interior is a supersonic tail encompassed by viscous shear layers. As this tail progresses into the subsonic diffuser section, it is gradually diffused. It is apparent from the interior shock wave structure that a virtual geometry change occurs due to the ability of shock waves to reflect on viscous shear layers, which govern this change. Hence, the converging-diverging concept of the intake is suppressed and it is difficult to identify the different ranges of operation. Hence, as the flow scenario of Appendix D.1 is deemed to be in the critical range, the reader is encouraged to take this attribute lightly.

Finally, Figure 4.6 shows the global results at this Mach number. It appears that the range of mass flow predicted by the model is narrow and that there is no dependence of total pressure recovery on the back pressure variation. Two possible explanations to this are provided. Firstly, the range of intake back pressures that was implemented at this Mach number was relatively narrow. As attempts were made to increase the back pressure beyond p_{e3}, the flow as predicted by the model became unstable and did not converge to any satisfactory solution. Secondly, the normal shock manifested at the tip of the lip wedge is of such strength that it constitutes a large part of the overall static pressure increase of the intake. This is the case regardless of the intake back pressure, seeing as the flow of the convergent section is independent of this parameter. The strength of this normal shock limits the degree of freedom of the subsequent flow, in terms of further increasing the static pressure by varying shock structures. Consequently, the total pressure recovery as predicted by the model appears to be invariant.

4.2.2 Conclusions of Validation Study

The general difference between the model and test results, as shown in Figures 4.3-4.6, is the prediction of total pressure recovery in the low-back-pressure, supercritical range. The observed trend is that this response, as predicted by the model, seems to converge towards a minimum value in this range. An investigation was carried out to ascertain the reasons for this. The conclusion was found by first identifying the flow structures that are present in this domain of operation. For a given Mach number and a relatively low intake back pressure, the sonic transition will occur in the subsonic diffuser. This means that shock structures will be present in this section. As previously argued, the reflections of oblique shock waves tend to cause separation along the subsonic diffuser walls. Furthermore, end-wall turbulence in the corners of the rectangular cross-section is another reason for strong separation. When these regions of separation merge, the consequence is highly skewed and distorted flow, compromising the axial uniformity of the flow. The distortion in terms of total pressure at the evaluation plane is illustrated in Figure 4.7. This graph shows the distortion coefficient of total pressure, as defined by Equation 3.15. Note that an *area average* was used to calculate this coefficient. As concluded, this distortion increases with decreasing intake back pressure, for each of the Mach numbers.

Keeping this reasoning in mind, the estimation of total pressure in the evaluation plane is considered next. In the wind tunnel tests, a total pressure rake was used to estimate this quantity. The rake is a series of thin tubes aligned with the axial direction of the intake, in which the total pressure is estimated after a complete deceleration of the flow. For a more thorough description of this measurement hardware, the reader is referred to any available literature on the subject. To simplify, each tube provides a distinct value of the total pressure, corresponding to a location in the flow. The final metric is the average of these distinct values. Since they are weighted equally, this corresponds to an *area average* of the total pressure in the evaluation plane. The locations of these tubes are illustrated in Figure 4.8a.

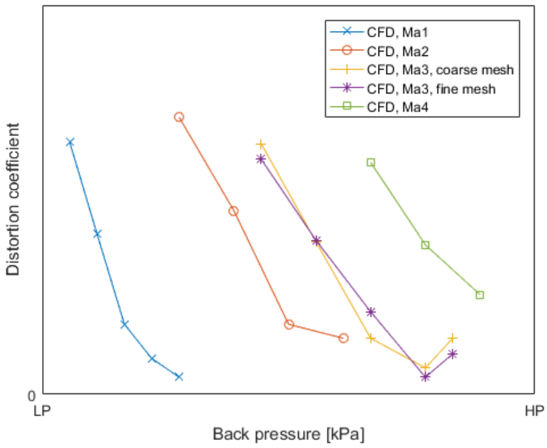

Figure 4.7: *Distortion of total pressure in evaluation plane for small-scale intake.*

In contrast, the estimation procedure of the total pressure in the model is based on a *mass flow average*, a choice that was discussed in Section 2.3.1. Furthermore, instead of basing the estimate on a discrete set of numbers, it is based on an area integral of the whole evaluation plane. Now, considering the example total pressure distribution of Figure 4.8b while taking into account that regions of high total pressure coincide with those of high mass flow, some conclusions can be drawn. Should the mass flow average of this distribution be calculated, it is evident that it would be heavily influenced by the region of high total pressure. Furthermore, projecting the rake tube locations of Figure 4.8a onto this distribution and imagining an area average being calculated as described above, it is understood why this value would be significantly smaller than the mass flow weighted average. Clearly, the distortion and skewness of the total pressure distribution is the reason as to why the area and mass flow averages differ. When considering the subcritical region, these coincide due to the very low, associated flow distortion. In summary, as the total pressure distortion is made larger, the average as predicted by the test and model results deviate to a greater extent. Therefore, in the supercritical region, the tests are able to predict a lower range of total pressure recovery than the model. Hence, it cannot be concluded that the intake flow as predicted by the model deviates in any way from the intake flow present in any physical test. It can only be concluded that the means by which the total pressure recovery is estimated in the tests and in the model are methodically different.

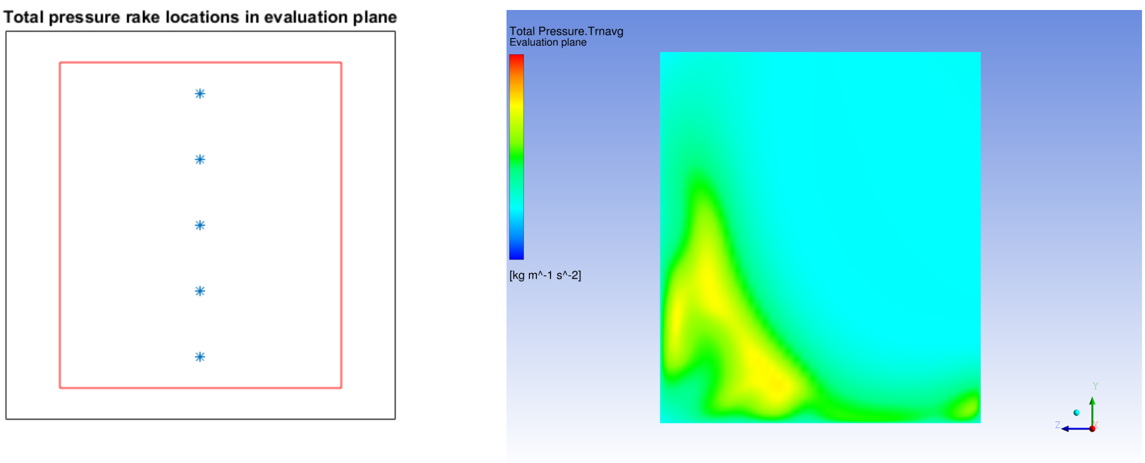

(a) *Total pressure rake locations in wind tunnel tests.*

(b) *Example of distorted total pressure distribution as predicted by model.*

Figure 4.8: *Procedures of estimating the total pressure in the evaluation plane.*

Another general conclusion of the validation study is that the model solutions obtained in the subcritical range were unstable and unsatisfactory, in general. As the intake back pressure was increased beyond critical values, the terminating normal shock of the intake flow was pushed upstream of the aerodynamic throat section. Such a shock is unsteady within the converging part of the intake, causing it to gradually move upstream and redirect the incoming, free-stream mass flow to the exterior. The result is an *unstart* of the intake. Judging from the investigated intake back pressure range, the stability margin is very small when transitioning from the critical point to the subcritical range.

As the validation study was completed, it was concluded that the model was sound and best suited to study Mach numbers at and below the design Mach number of the intake geometry. Several topics of discussion that were outside the primary scope of the study arose and will be treated in Chapter 5. The primary question relates to whether the wind tunnel testing or the CFD model provides the best estimation of total pressure recovery in the supercritical range. Secondary subjects include turbulence and boundary layer modelling.

4.3 Results of Parametric Study

On the basis of the validated CFD model, the secondary objective was to perform a parametric study of a real-size, generic intake featuring two distinctly different ramp configurations. These are illustrated in Figure 4.2. The first is the reference geometry of the intake, uniformly scaled. The second is an alternative design in which two straight ramp segments replace the continuous curve, such that the initial and total deflection angles of the ramp are the same. In the forthcoming sections, *IR* (Isentropic Ramp) and *DR* (Discrete Ramp) are the short names used to reference the different geometries. A decision was made to use the same reference intake geometry that was used in the validation study. This was done for two primary reasons. Firstly, the time window of the project did not allow for the creation of an entirely new geometry. Secondly, using the same geometry for both small-scale and large-scale simulations would allow for a direct comparison between the two, in terms of the studied performance. This would ultimately allow for conclusions to be drawn relating to the dynamic similarity of the intake. Based on a typical engine mass flow requirement of a real-size intake at the design Mach number and flight altitude, the scaling factor was calculated as $SF \approx 37$, following the procedure of Section 3.6. Before proceeding to the results of the parametric study, it should be noted that some modifications were made to the CFD model after the conclusion of the validation study. Firstly, the employed mesh was a modified version of the fine mesh, as described in Section 2.3.3. Secondly, in order to make the interior outlet boundary condition more robust, the extension that was added to the subsonic diffuser section was made significantly longer. This was done to avoid the problems of instability described in Section 2.2.1. The disadvantage of this increase of extension length proved to be an increase of the number of iterations that was required by steady-state simulations to obtain a fully developed flow, due to the increased propagation distance of the boundary condition.

When proceeding to the parametric study, the flight altitude was also changed from ground level to an intake design, stratospheric altitude. In addition to studying the characteristic intake response in terms of engine mass flow and total pressure recovery, aerodynamic forces have been predicted by the model. The results are presented in Sections 4.3.1 and 4.3.2, respectively. The extent of the parametric study, shown in Table 4.2, is similar to that of the validation study in terms of the implemented range of Mach numbers and intake back pressures. Due to the three-dimensional nature of the flow, it has proven difficult to identify the range to which certain simulations belong. The reader is therefore encouraged to take these attributes lightly, as they are listed in Table 4.2. Note that the Mach numbers investigated in the parametric study are different than those of the validation study, with the exception of $M_{V,1} = M_{P,1}$. Also, due to the increase of flight altitude, the imposed intake back pressures are not the same in absolute terms. Although, while individual values were slightly modified, the range in terms of the relative static pressure increase of the intake was maintained.

4.3.1 Mass Flow and Total Pressure Recovery

As the simulations of the respective geometries were completed, predictions of engine mass flow and total pressure recovery were extracted using the same procedure as in the validation study. The results are presented in Figures 4.9-4.12. Note that since $M_{V,1} = M_{P,1}$, Figure 4.9 includes reference curves pertaining to the wind tunnel tests and small-scale simulations. The abbreviations *ss* (small-scale) and *ls* (large-scale) are introduced.

Table 4.2: Simulations of parametric study.

Case	Comments	
Geometry	*IR*	*DR*
$M_{P,1}$	Off-design operation, $M_{P,1} < M_d$	
$p_{1,1}$	Supercritical range	Supercritical range
$p_{1,2}$	Supercritical range	Supercritical range
$p_{1,3}$	Critical point	Critical point
$p_{1,4}$	Subcritical range	Subcritical range
$p_{1,5}$	Subcritical range	Subcritical range
$M_{P,2}$	Off-design operation, $M_{P,2} < M_d$	
$p_{2,1}$	Supercritical range	Supercritical range
$p_{2,2}$	Supercritical range	Supercritical range
$p_{2,3}$	Critical point	Critical point
$p_{2,4}$	Subcritical range	Subcritical range
$p_{2,5}$	Subcritical range	Failed due to instability
$M_{P,3}$	On-design operation, $M_{P,3} = M_d$	
$p_{3,1}$	Supercritical range	Supercritical range
$p_{3,2}$	Supercritical range	Supercritical range
$p_{3,3}$	Critical point	Critical point
$p_{3,4}$	Subcritical range	Subcritical range
$M_{P,4}$	Off-design operation, $M_{P,4} > M_d$	
$p_{4,1}$	Supercritical range	Supercritical range
$p_{4,2}$	Supercritical range	Supercritical range
$p_{4,3}$	Failed due to instability	Supercritical range
$p_{4,4}$	Failed due to instability	Critical point

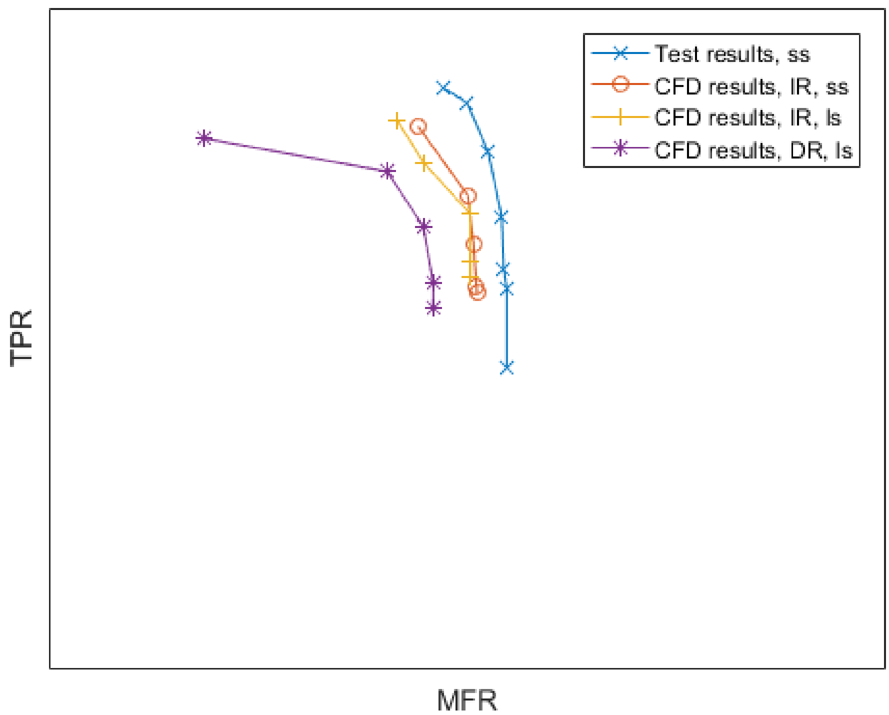

Figure 4.9: *Mass flow versus total pressure recovery for large-scale intake, $M = M_{P,1}$*

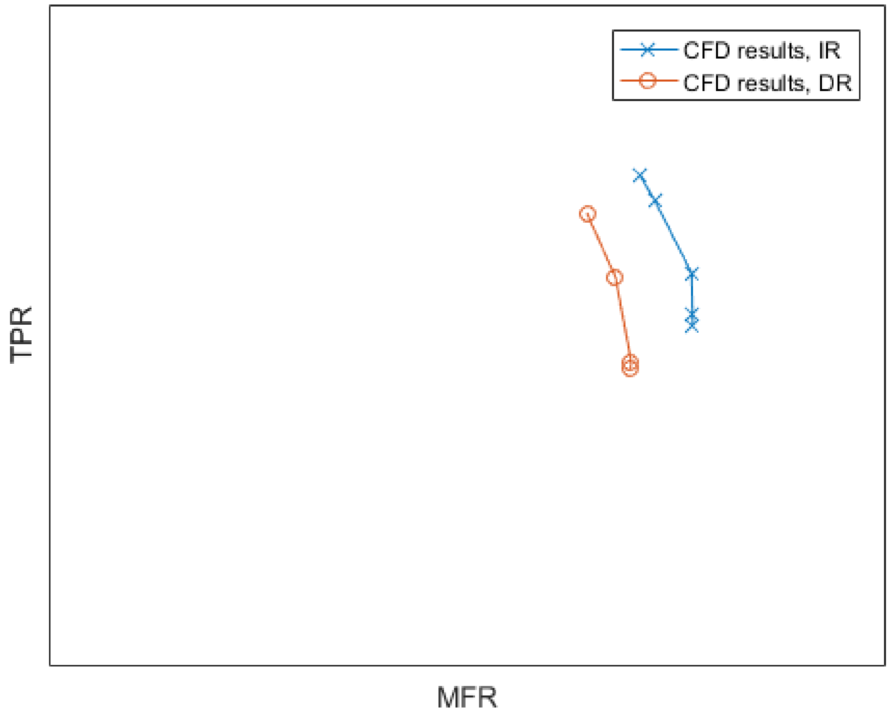

Figure 4.10: *Mass flow versus total pressure recovery for large-scale intake,* $M = M_{P,2}$

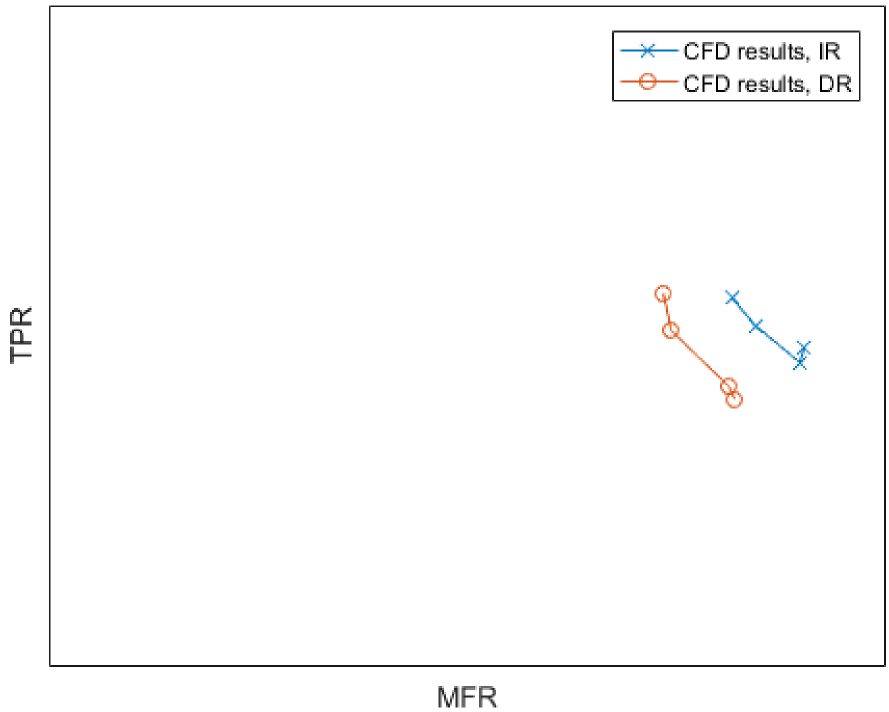

Figure 4.11: *Mass flow versus total pressure recovery for large-scale intake,* $M = M_{P,3}$

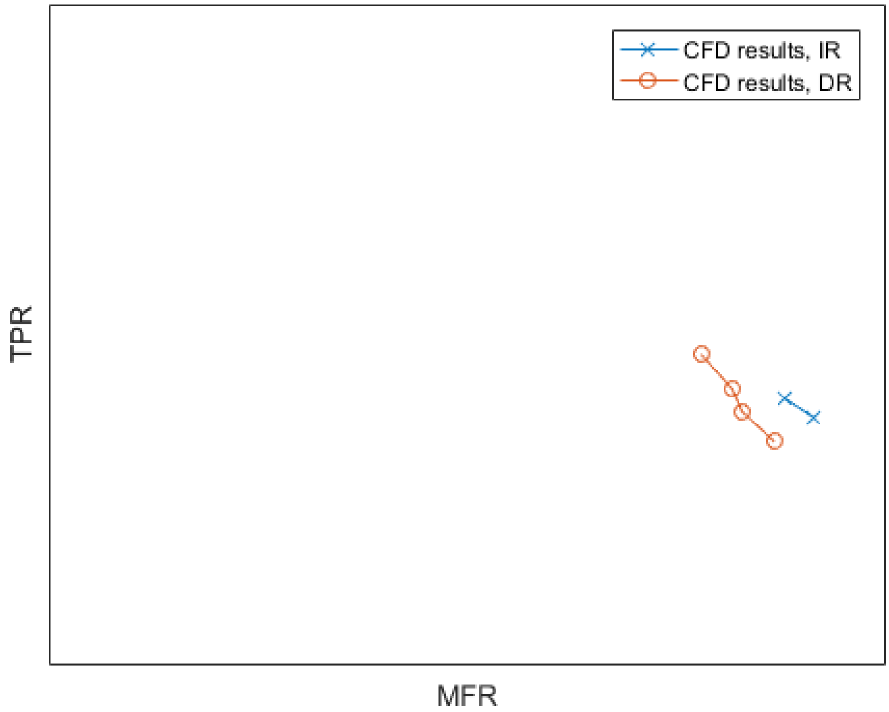

Figure 4.12: *Mass flow versus total pressure recovery for large-scale intake, $M = M_{P,4}$*

Mach $M = M_{P,1}$

The results of simulations run at $M_{P,1}$ are shown in Figure 4.9. The first observed trend is that the scaling of the intake has a negligible influence on the global performance in terms of mass flow and total pressure recovery. Even though the Reynolds number is increased at a large scale, the resulting decrease of total pressure losses associated to viscous effects appears to be negligible. The primary study, however, concerns the differences in performance relating to the different geometries, and will be the subject moving forward. Flow fields pertaining to the different operating ranges at the current Mach number, for the two geometries, are illustrated in Appendix E. The most distinct difference between the respective geometries is the mass flow swallowed by the intake. This is attributed to the characteristics of the external compression phase, where the oblique shock waves at the discrete ramp dictate that a larger mass flow spillage occurs. Furthermore, the steady flow prior to the aerodynamic throat section is independent of downstream pressure conditions in the critical and supercritical range, hence the rather constant offset of mass flow at these conditions. When increasing the back pressure enough to reach the subcritical range, it appears that the mass flow of the *DR* geometry deteriorates rapidly. From Appendix E.2, it is obvious that a significant portion of the mass flow is diverted into the bleed channel by the impulse of a skewed, adverse pressure gradient. This is likely a case of a very small stability margin in terms of increasing the downstream static pressure. Since the flow leaving the ramp of the *IR* configuration has a higher momentum due to the decreased mass flow spillage and more efficient compression, a larger impulse is required to divert this flow into the bleed channel. This is a potential explanation as to why this rapid diversion of flow into the bleed channel appears to be delayed when comparing to the *DR* configuration.

The second general observation is that while the mass flow is significantly different between the two geometries, the difference in overall total pressure recovery is very small. While the external compression fan of the isentropic ramp causes negligible total pressure losses, there is a distinct total pressure loss associated to the corresponding oblique shock waves of the discrete ramp. However, due to the increased interior mass flow and velocities of the *IR* geometry, the losses attributed to the terminating normal shock are larger in this case. Consequently, the global levels of total pressure recovery differ very slightly.

Mach $M = M_{P,2}$

As the Mach number is increased to $M_{P,2}$, slightly below the design Mach number M_d, the same general observations as for $M_{P,1}$ are made. The swallowed mass flow differs significantly between the geometries and the total pressure recovery levels differ very slightly. The exception to the latter is the supercritical range, where it appears that the levels are noticeably smaller for the *DR* geometry. For the same reasons discussed in Section 4.2.2, the total pressure recovery converges towards a minimum value as the back pressure is reduced. The supercritical range of this Mach number is illustrated in Appendix F. Another interesting tendency that is observed is that separation is initiated on different sides of the subsonic diffuser, depending on the ramp configuration. As the separation is initiated at locations of oblique shock wave reflections, this behavior is likely very sensitive to the shock structure. The reader is encouraged to also observe the small separation bubbles that occur at wave reflections prior to the the ultimate separation. An additional, general trend is that separation propagates from the cross-sectional corners of the subsonic diffuser geometry due to end-wall effects. These propagating separation wakes merge and cause the skewed and distorted distribution of properties at the engine face.

Mach $M = M_{P,3}$

An increase to the design Mach number $M_{P,3} = M_d$ is made evident by the angle of the initial, oblique shock wave, as illustrated in Appendix G. This angle is such that this shock wave will reflect on the tip of the lip wedge of the intake. For the *IR* geometry, this means that mass flow spillage over the lip wedge is eliminated, maximizing the swallowed mass flow. Due to the second oblique shock wave present in the *DR* configuration, which is significantly stronger than the initial one, mass flow spillage is still present in this case. Hence, the difference in swallowed mass flow between the geometries is at a maximum at this Mach number. In the subcritical range, when moving the sonic transition upstream from the throat section, the recirculating flow causes a significant portion of the mass flow to bleed to the exterior. When reducing the adverse pressure gradient by means of lowering the intake back pressure, the flow leaving the ramp is forced to expand and accelerate over the trailing edge of the bleed channel, eliminating bleed spillage by means of circulatory flow. Hence, a wide range of engine mass flows is predicted due to the undesired feature of re-circulation in the subcritical range.

Mach $M = M_{P,4}$

Increasing the Mach number to a value $M_{P,4}$, greater than the design Mach number M_d, minimizes the deviation of mass flow between geometries, as the secondary oblique shock of the *DR* configuration now causes a very small spillage over the lip wedge, as can be seen in Appendix H. The external compression fan of the *IR* configuration now has a focal point that deviates to the interior from the lip wedge. Hence, a normal shock is undergone by the remainder of the capture area mass flow. The result is an additional shear layer being ingested in the interior of the intake, adding to the complexity of the flow both physically and numerically. Despite numerous attempts using different sizes of time steps, ramping of boundary conditions and numerical schemes, no converged solutions were obtained for the *IR* configuration at high intake back pressures.

4.3.2 Aerodynamic Forces

Apart from studying the performance of the intake in terms of total pressure recovery and ingested mass flow, a large interest was put on the aerodynamic forces acting on the intake due to the various pressure and shear stress distributions arising at the different operating conditions. Definitions of lift, drag and pitch torque were introduced in Section 3.7, along with a classification of contributory sources. It was argued that the lift generated by the intake is not of interest, since it is not its primary task. Furthermore, the drag, which is of essential interest to intake design, was divided into sources of pressure and shear forces. Finally, the pitch torque, acting about the z axis as depicted by Figure 4.1, was calculated while neglecting the contribution of shear forces. This was done at two locations and the intermediate range was obtained by means of linear interpolation, which is sufficient due to the expected linear response of torque along the axial direction. Using the coordinate system of Figure 4.1, these locations were chosen to be (x_1, y_m), (x_2, y_m). The pair x_1 and x_2 was chosen as the leading and trailing edge of the intake, respectively. Also, y_m was chosen as the y coordinate of the subsonic diffuser symmetry plane. Hence, an axial distribution of pitch torque was obtained for the whole length of the intake. The sign convention is such that this quantity is defined positive in the counter-clockwise direction.

Intake drag

The pressure-induced drag exerted on the intake at the different operating conditions is presented in Figures 4.13a-4.13d below. At this stage, two things are repeated. Firstly, the internal contribution is the drag acting on all the surfaces encompassing the mass flow that ultimately enters the engine. The external contribution is the drag on all exterior surfaces, also including those of the bleed channel. Consequently, the spillage drag is represented implicitly as the relative change of external drag. Secondly, observing these graphs, the sizes of the drag forces are omitted. A reference *0* is kept to highlight the change of sign. Still, all graphs feature the same range of drag forces, allowing for a comparison between results of different Mach numbers in relative terms. The levels of back pressure are also omitted, with the individual ranges being defined by *LP* (low pressure) and *HP* (high pressure).

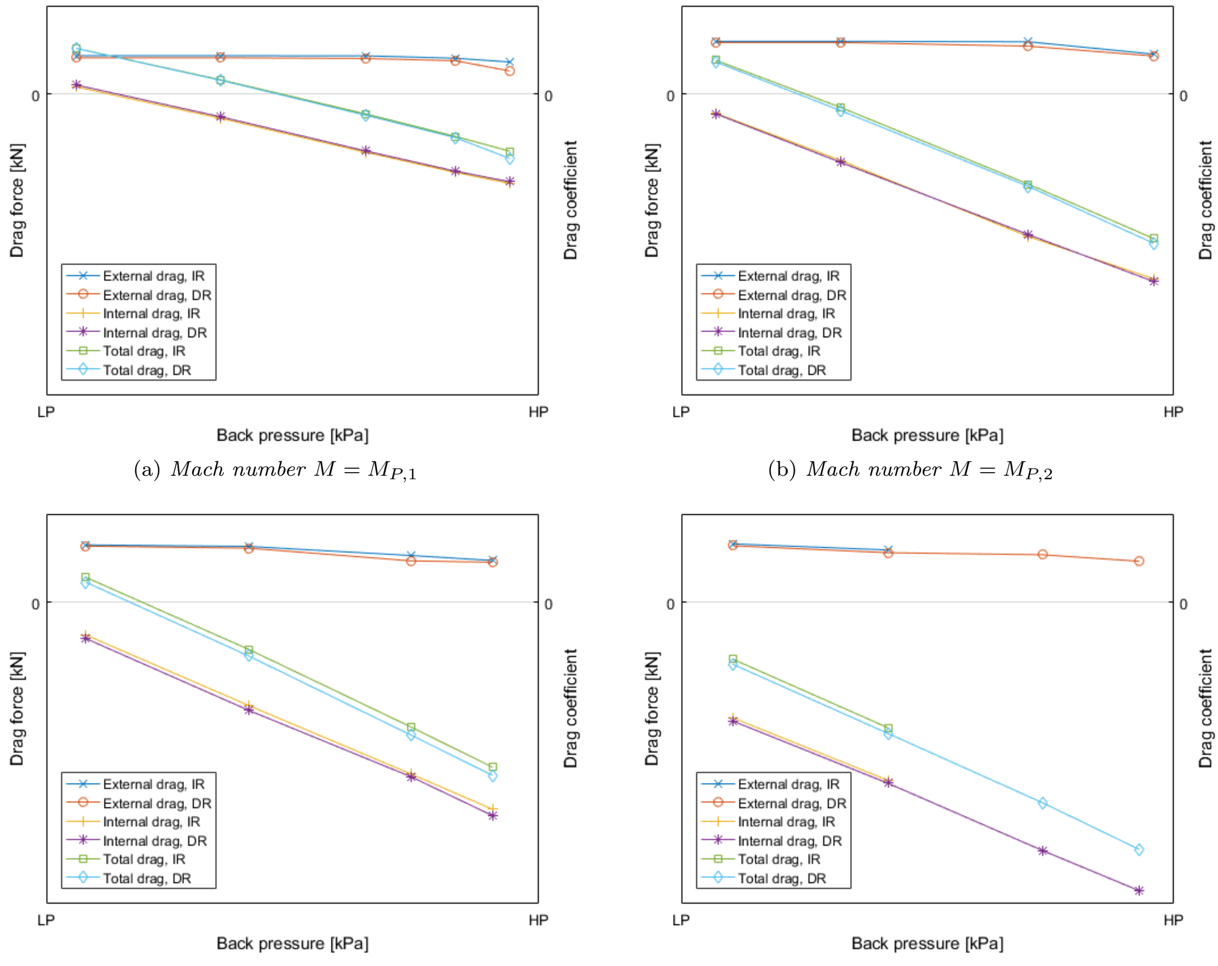

(a) *Mach number $M = M_{P,1}$*

(b) *Mach number $M = M_{P,2}$*

(c) *Mach number $M = M_{P,3}$*

(d) *Mach number $M = M_{P,4}$*

Figure 4.13: *Pressure-induced drag acting on intake for the different conditions of flight.*

For the sake of fluidity in the forthcoming analysis, the number of references to individual simulations in appendices will be kept at a minimum. Hence, the reader is encouraged to independently consult these. On the basis of the results shown in Figure 4.13, the first observation is that the shape of the ramp has a negligible influence on the drag in a global perspective. The second observation made is that the external drag seems to be fairly constant and independent of the intake back pressure. Knowing that the external drag for a given Mach number case can only vary by means of increasing the mass flow spillage to the exterior, two sources would potentially cause deviations. These are the mass flow spillages over the lip wedge and in the bleed channel.

Now, since a significant redistribution of mass flow and pressure on the exterior is only possible by means of pushing the terminating normal shock outside of the intake, an unstart would be required to significantly increase spillage drag. Since this phenomenon lies well into the subcritical range and outside the range of model stability, it is not accounted for. Hence, the only source in the range of model stability that causes a deviation to the external drag is that of mass flow bleed. Moreover, spillage through the bleed channel is caused by two different mechanisms; expansion over the trailing edge of the ramp or re-circulation of flow due to a mismatch of the actual and effective throat area. The former is the way in which the bleed channel is supposed to operate while the latter is an undesired feature. Two examples of flow situations featuring these mechanisms are shown in Appendices E.1 and G.1, respectively. When considering the first scenario, the flow quickly expands to the ambient pressure of the bleed channel after leaving the trailing edge of the ramp. Hence, no additional drag is exerted on the intake as it aligns with the back surface of the bleed channel. In the second scenario, the recirculating flow aligns with the front surface to provide a marginal reduction of the induced drag.

Finally, the drag component that exhibits the largest dependence on back pressure is the internal contribution. In the supercritical range, the force exerted on the intake is acting in terms of conventional drag, opposing the direction of movement. However, when raising the back pressure enough, a change of sign is observed and the exerted force is acting in terms of thrust rather than drag. To explain this behavior, the simplification of a convergent-divergent duct can be considered. Considering the external compression phase as the convergent section, a relatively constant, positive drag contribution is made. In the subsonic diffuser section, representing the divergent part, a negative drag contribution is made. When the adverse pressure gradient and the overall pressure levels of this section is increased, it is natural that this contribution is made larger. Furthermore, increasing the operating Mach number enables larger overall pressure ratios due to the increase of converted kinetic energy. Hence, the exerted force in terms of thrust acting on the intake is increased as the Mach number is increased. On a final note, the pressure thrust in the high-back-pressure, subcritical regions are comparable to the momentum thrust of the engine on which the intake scaling was based.

Next, the drag resulting from viscous forces are considered and the results are shown in Figure 4.14.

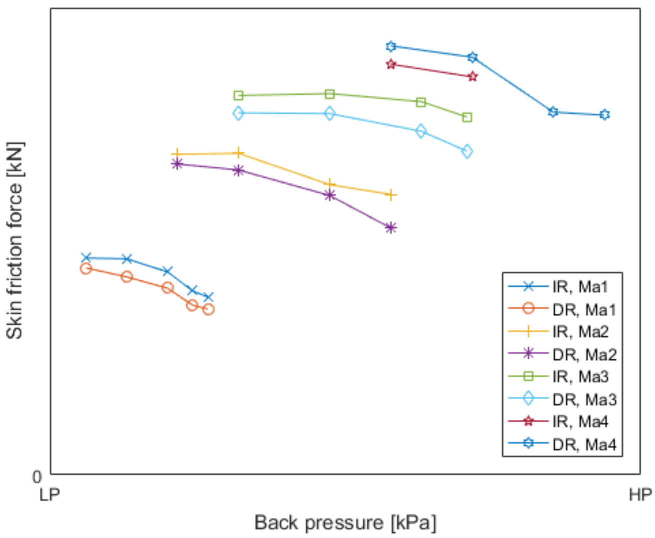

Figure 4.14: *Shear-induced drag acting on intake.*

Here, three key tendencies are identified and attributed to the velocity distribution inside the intake. When increasing the velocity along walls, the adverse velocity gradient is made larger as a result of the implemented *No Slip* boundary condition. This ultimately increases the flow shear and the resulting forces. Consequently, increasing the free stream Mach number increases the shear drag of the intake. Furthermore, the skin friction drag is reduced by means of increasing the back pressure, allowing for subsonic flow throughout the subsonic diffuser. When evaluating differences between forces of the different geometries, the *DR* configuration exhibits slightly smaller forces for each Mach number case, with the exception of $M_{P,4}$. A potential explanation to this is the increased mass flow spillage and less efficient external compression of the *DR* configuration, limiting the momentum and ultimately the velocities of the interior flow. At $M_{P,4}$, the supersonic tail entering the intake of the *IR* geometry has a significantly smaller contact area with the intake, interior walls. Hence, the forces are marginally smaller at this Mach number for the *IR* configuration. On a final note, the predicted viscous forces are an order of magnitude smaller than the pressure forces.

Pitch torque

When considering supersonic intakes of the rectangular kind, non-symmetric pressure and shear stress distributions also give rise to an induced torque. Hence, as a secondary study, the axial distribution of pitch torque has been predicted by the model, as previously described. No major differences were identified between the results of different geometries. For the sake of conciseness, only the results pertaining to the Mach numbers $M_{P,1}$ and $M_{P,3}$ are presented. The abbreviations *LE* (leading edge) and *TE* (trailing edge) are introduced, referring to the axial position of the intake.

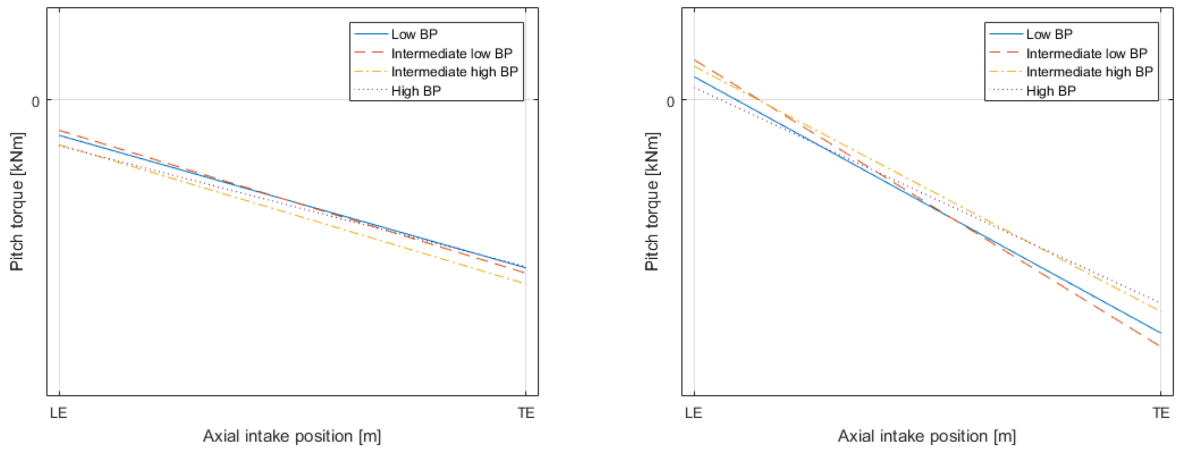

(a) *IR geometry*, $M = M_{P,1}$.

(b) *IR geometry*, $M = M_{P,3}$

Figure 4.15: *Axial distribution of pressure-induced pitch torque.*

While no apparent trend is identified relating to back pressure variations, a change of sign occurs at a point of equilibrium close to the leading edge of the intake. For the case of $M_{P,1}$, this is realized by extrapolating the linear response upstream of the intake leading edge. The Mach number variation indicates that the point of equilibrium is moved further downstream as the Mach number is increased. Furthermore, as one moves further downstream, the pitch torque grows in the clockwise direction. While the pressure force distribution of the subsonic diffuser section is relatively symmetric, the non-symmetric distribution of the ramp gives rise to the increase of torque towards the engine face. Finally, it can also be concluded that the wedge denoted as *B-C* in Figure 1.1 is likely integrated to reduce the size of the induced pitch torque.

4.3.3 Conclusions of Parametric Study

Concluding the parametric study, the aerodynamic performance of the intake was evaluated at the different operating conditions. This was done in terms of primary objectives of ingested mass flow and total pressure recovery, and secondary objectives of intake drag and pitch torque. The most distinct difference observed between the different geometries is that of significantly increased mass flow spillage using the *DR* geometry. This effect is mostly pronounced for Mach numbers at and below the design Mach number. Furthermore, having two discrete oblique shock waves in the external compression phase rather than a continuous compression fan results in significantly higher, local total pressure losses. However, due to the decrease of ingested mass flow and momentum, the total pressure losses associated with the terminating shock structures inside the intake are made smaller. Hence, the global levels of total pressure recovery differ only slightly between geometries. Following the same reasoning of a decrease of ingested mass flow and momentum, some secondary effects are observed. Firstly, the stable range in the subcritical region is reduced using the *DR* geometry. This tendency was pronounced at $M = M_{P,1}$ where the ingested mass flow would quickly deteriorate as significant portions were diverted into the bleed channel, but also at $M = M_{P,2}$ where high back pressure simulations failed due to instability. However, at $M = M_{P,4}$ above the design Mach number, the opposite was observed. Due to the flow complexity resulting from the presence of several shear layers, the *IR* geometry featured a smaller stability range in the subcritical range of this Mach number.

Relating to the secondary design objective of reducing flow distortion in the engine face, distortion coefficients of total pressure were also calculated at the large scale. The results are shown in Figure 4.16. This is the same behavior that was observed on the small scale, discussed in Section 4.2.2. Still, another tendency is identified when extended to geometry variations. Using the *DR* geometry, the distortion is slightly reduced.

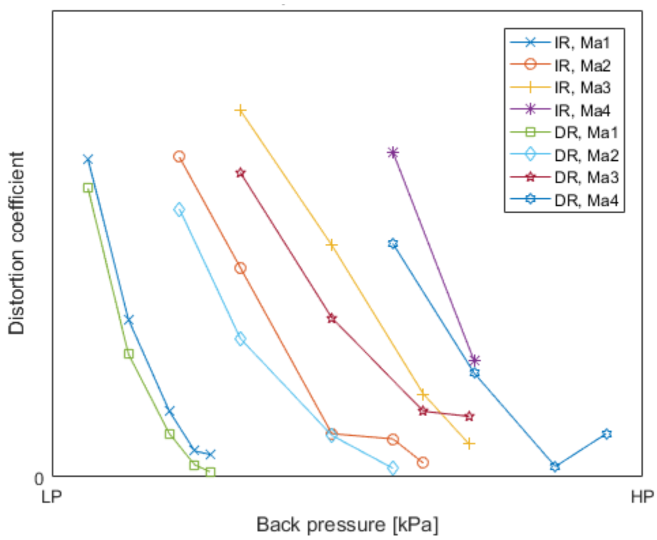

Figure 4.16: *Distortion of total pressure in evaluation plane for large-scale intake.*

Proceeding to the evaluation of intake drag, a negligible deviation was observed between the geometries. In the range of model stability, the external drag acting on the intake was rather constant and spillage drag was considered to be negligible. Finally, the internal drag varied greatly as a function of the intake back pressure. At the critical point of operation of each Mach number case, a favorable pressure distribution in the subsonic diffuser section was obtained, such that the exerted forces on the intake were in terms of thrust. While values of these forces were omitted due to confidentiality, it can be concluded that the pressure thrust at these operating conditions is comparable to the momentum thrust of the typical engine that was the basis of the intake scaling. Caution is however advised. Due to the simplified model isolating the intake, this effect can be misunderstood. The effect of a thrust contribution from the static pressure distribution of the intake is likely partially or completely cancelled out by the subsequent components of the engine unit.

5 Discussion

After the conclusion of the project, a lot of interesting topics of discussion have arisen. Following the validation study, the drawbacks of the CFD model and the wind tunnel testing have been considered. On the basis of the parametric study, some design guidelines have been identified. Also, the applicability of preliminary design tools such as shock relations has been assessed. Considering numerical aspects, boundary layer and turbulence modelling is critical to the fidelity of the CFD model, but also very heavy in terms of computational efforts.

Following the conclusions of the validation study, it was evident that the primary model uncertainty was that of total pressure recovery estimation in the supercritical range. The one-dimensional pressure rake distribution in the wind tunnel testing would be unable to account for the three-dimensional flow, as predicted in the small-scale, CFD study. Hence, the question arose whether the wind tunnel testing equipment needs to be extended or if the separation-induced skewness and distortion of CFD simulations are unrealistic. Numerous authors, of which [24] is one, point to the tendency of overestimating the onset of separation while using the SST model. Thus, the argument can be made that the level of distortion is unrealistic. However, the results of this study consolidates those of experimental wind tunnel tests as well as RANS simulations [16], which have proved supersonic intake flow to be highly three-dimensional. This also extends to rectangular intakes under symmetric, free-stream conditions. On the contrary, the argument can thus also be made that the present wind tunnel testing equipment is insufficient to account for such flow structures.

When considering the separation behavior observed in these studies, the common trend is that the large variety of distorted flows is a result of separation caused by case-dependent, oblique shock wave reflections and end-wall effects. The latter seems quite ambiguous, seeing as the end-wall separation regions seem to choose a side even though the geometry, mesh and free-stream conditions are symmetric. It is likely that this tendency is a result of small-scale non-symmetries in the mesh. Although, no indication of this has been found. However, the locations of oblique shock wave reflections causing separation are likely very independent of the mesh, seeing as the strong impulses resulting from adverse pressure gradients across shocks do not depend on the local, spatial resolution to such an extent. Consequently, it is reasonable to suspect that while the level of distortion likely would be unaffected by increasing the boundary layer resolution, the skewing induced by end-wall effects could be. On the topic of flow distortion, the final conclusion is that the complex, supercritical flow scenarios predicted by this model would be highly disadvantageous to blade design in subsequent compressor blade rows. This design procedure heavily relies on the assumption of axially uniform upstream flow.

On the topic of turbulence modelling, a variety of factors influenced the choice of turbulence model. Primarily, the time window of the project did not allow for models that were heavier in terms of computational efforts by requiring a higher resolution in time. Selecting the SST model and employing the strategy of transient, time-averaged solutions, CFL numbers in unsteady and turbulent regions were kept safely below 100 by the choice of time step size. The two additional parameters affecting the computational requirements of the simulations were considered to be the choice of mesh sizes and physical simulation time. These choices were discussed in Chapter 2. It was estimated that the simulations of this project, including steady-state and unsuccessful simulations, have required 100 000-150 000 CPU hours. Consequently, using turbulence models such as *LES* (Large Eddy Simulation), that likely would require CFL numbers to approach unity, would not be feasible. In summary, the choice of the SST model was made due to its praised ability of dealing with wall-bound, adverse-pressure-gradient flow and of predicting separation. The choice of the parameters discussed above was made to obtain a representative time average by mainly resolving the low-frequency components of the flow and filtering the high-frequency components.

After the conclusion of the parametric study, some general design guidelines were made. The first relates to the design of the ramp, which is chosen such that the capture area mass flow is completely ingested by the intake at the design Mach number. When considering discrete and straight ramp segments, there is an optimality condition corresponding to maximizing the total pressure recovery for a discrete set of shock waves. Cited by many authors [20], the total pressure recovery of the shock system is maximized if all shocks of the considered system are of equal intensity. The problem with implementing this condition in the *DR* geometry of this study was that the initial shock wave of the two-wave system is significantly weaker than the secondary shock, in general terms. If the initial shock wave were to be made stronger, the mass flow spillage would be significantly increased. Hence, the maximization of total pressure recovery in the external compression is secondary to maximizing mass flow at the design Mach number. On the subject of ramp design, shock relations are an excellent tool to accurately predict wave angles and estimate property ratios across individual waves. The applicability is limited in the sense that when interactions of shock waves and viscous effects are considered, CFD analysis is required. Another general observation relating to design is that the aerodynamic throat section could be subject to improvement or optimization across the Mach number range, adapting it to the effective throat area of the flow. This would likely reduce or eliminate recirculating flow in the throat section and increase the efficiency of the bleed channel. Differential continuity relations introduced in Chapter 3 allow an intuitive understanding of how this effective throat section area varies with free stream Mach number. The applicability as a preliminary design tool is however likely limited due to the violation of the assumption of quasi one-dimensional, isentropic flow that precedes the derivations of these relations.

Some recommendations for future work are formed from the conclusions of the project. For the sake of structure, they are listed below, in no particular order.

1. On the topic of CFD model uncertainty, useful insight would likely be gained by performing a validation study on one or more cases using alternative turbulence models and increasing the resolution in time.

2. The practical advantage of having a discrete-segment ramp configuration is that it allows the user to implement active control of the deflection angles. It would thus be interesting to optimize the discrete-type ramp design for each Mach number case, simulate and compare the results to those of geometries featuring the continuous-curve type ramp.

3. The aerodynamic throat section could be subject to improvement or optimization across the Mach number range, as discussed above.

4. When considering free-stream conditions, a future study could include angles of attack and yaw, resulting from maneuverability of the aircraft.

5. One of two major factors contributing to the distortion and skewness of diffuser flow is its cross-sectional shape. A key to limiting these unwanted features could be to perform an investigation into potential shapes that could more efficiently avoid the induction of end-wall turbulence that ultimately causes heavy separation.

6. It is likely that a more efficient mesh, in terms of minimizing unnecessary, spatial resolution in the far-field domain, could be obtained by adopting an unstructured meshing approach.

References

[1] J. D. Anderson. *Fundamentals of Aerodynamics.* 2nd ed. McGraw-Hill Higher Education, 1991.

[2] J. D. Anderson. *Modern Compressible Flow: With Historical Perspective.* 3rd ed. McGraw-Hill Higher Education, 2004.

[3] N. Andersson. "A Study of Subsonic Turbulent Jets and Their Radiated Sound Using Large-Eddy Simulation". PhD thesis. Chalmers University of Technology, 2005, pp. 11-12.

[4] *ANSYS Help Viewer.* Version 18.1.0. ANSYS, 2017.

[5] C. Bourdeau, M. Blaize, and D. Knight. Performance Analysis for High-Speed Missile Inlets. *Journal of Propulsion and Power* **16**.6 (2000), pp. 1125-1126.

[6] C. Bourdeau et al. Three Dimensional Optimization of Supersonic Inlets. *35th AIAA/ASME/SAE/ASEE Joint Propulsion Conference and Exhibit* (1999), pp. 1-2.

[7] J. R. Colville. "Axisymmetric Inlet Design for Combined Cycle Engines". MA thesis. University of Maryland, 2005, pp. 1-3.

[8] S. Dixon and C. Hall. *Fluid Mechanics and Thermodynamics of Turbomachinery.* 7th ed. Elsevier Inc., 2014.

[9] A. Gaiddon and D. D. Knight. Multicriteria Design Optimization of Integrated Three-Dimensional Supersonic Inlets. *Journal of Propulsion and Power* **19**.3 (2003), pp. 456-462.

[10] A. Gaiddon, D. D. Knight, and C. Poloni. Multicriteria Design Optimization of a Supersonic Inlet Based upon Global Missile Performance. *Journal of Propulsion and Power* **20**.3 (2004), p. 542.

[11] N. J. Georgiadis, D. A. Yoder, and W. A. Engblom. Evaluation of Modified Two-Equation Turbulence Models for Jet Flow Predictions. *AIAA Journal* **44**.12 (2006), pp. 3-4.

[12] E. L. Goldsmith et al. *Air Intakes for High Speed Vehicles.* Tech. rep. Advisory Group for Aerospace Research Development, 1991, p. 5.

[13] T. Grönstedt. *Lecture notes in Gas Turbine Theory.* Sept. 2016.

[14] P. Malan and E. F. Brown. Inlet Drag Prediction for Aircraft Conceptual Design. *Journal of Aircraft* **31**.3 (1994), pp. 616-622.

[15] F. R. Menter. Zonal Two Equation k-ω Turbulence Models for Aerodynamic Flows. *24th Fluid Dynamics Conference* (1993), pp. 1-5.

[16] X. Montazel, Y. Kergaravat, and M. Blaize. Navier-Stokes Simulation Methodology for Supersonic Missile Inlets. *13th ISABE* (1997).

[17] J. S. Mount. Effect of Inlet Additive Drag on Aircraft Performance. *Journal of Aircraft* **2**.5 (1965), p. 374.

[18] G. L. Muller and W. F. Gasko. Subsonic-Transonic Drag of Supersonic Inlets. *Journal of Aircraft* **4**.3 (1967), p. 231.

[19] D. Pagan and A. Gaiddon. Design Methodology for Supersonic Air Intakes. *37th Joint Propulsion Conference and Exhibit* (2001).

[20] H. Ran and D. Mavris. Preliminary Design of a 2D Supersonic Inlet to Maximize Total Pressure Recovery. *AIAA 5th Aviation, Technology, Integration, and Operations Conference* (2005), p. 2.

[21] H. I. H. Saravanamuttoo, G. F. C. Rogers, and H. Cohen. *Gas Turbine Theory.* 6th ed. Pearson Education Limited, 2009.

[22] G. Saravanan, R. Kumar, and A. V. Kumar. Performance Analysis of a Two-Dimensional Supersonic Diffuser. *Journal of Advances in Mechanical Engineering and Science* **2**.2 (2016), p. 42.

[23] M. R. Soltani et al. Numerical Simulation and Parametric Study of Supersonic Intake. *Journal of Aerpspace Engineering* **227**.3 (2012), p. 467.

[24] R. Tharwat, M. El-Samanoudy, and A. El-Baz. Considerations of Stress Limiter for the SST Turbulence Model in Dual Throat Nozzle Predictions. *Ninth International Conference on Computational Fluid Dynamics* (2016), pp. 1-4.

[25] J. R. Turner and T. R. Yoos. *Pressure Loss Calculation for High Speed Gas Flow in Ducts.* Tech. rep. DYNATECH Corporation, 1961, p. 10.

[26] Y. Watanabe and A. Murakami. *Control of Supersonic Inlet with Variable Ramp.* Tech. rep. Aviation Program Group, Japan Aerospace Exploration Agency, 2006, p. 1.

[27] F. M. White. *Fluid Mechanics.* 7th ed. McGraw-Hill Higher Education, 2011.

A Validation study simulation, $M_{V,1}$

A.1 Critical operating point, $p_{1,4}$

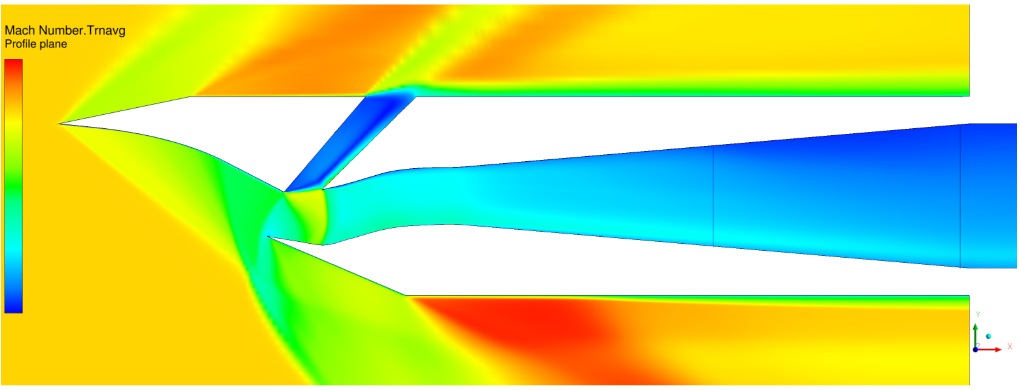

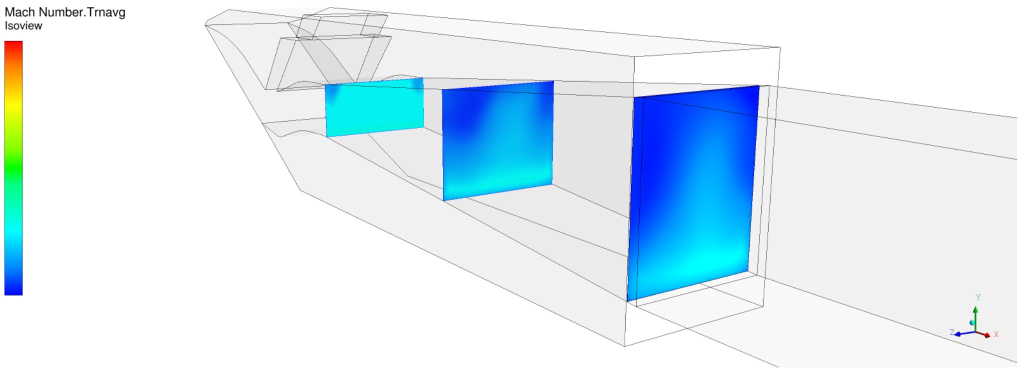

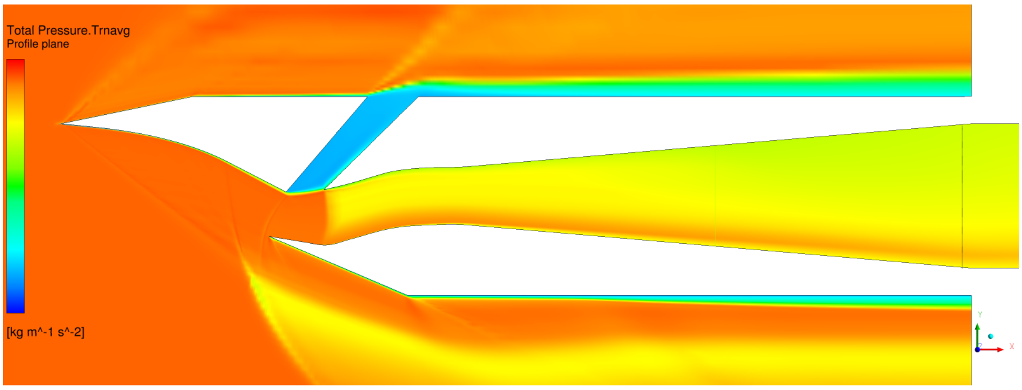

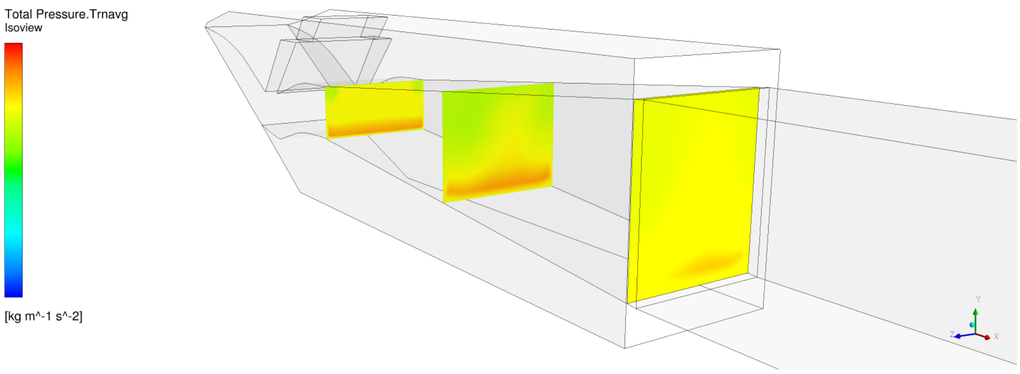

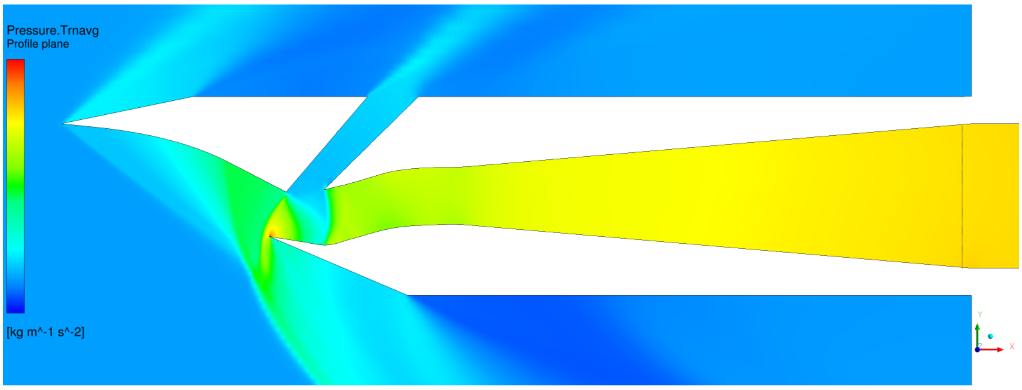
Pressure.Trnavg
Profile plane
[kg m^-1 s^-2]
Y
X

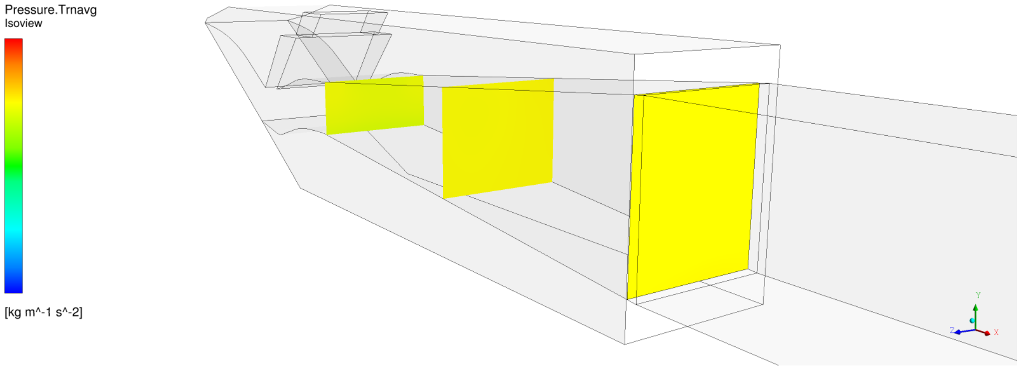
Pressure.Trnavg
Isoview
[kg m^-1 s^-2]
Y
X

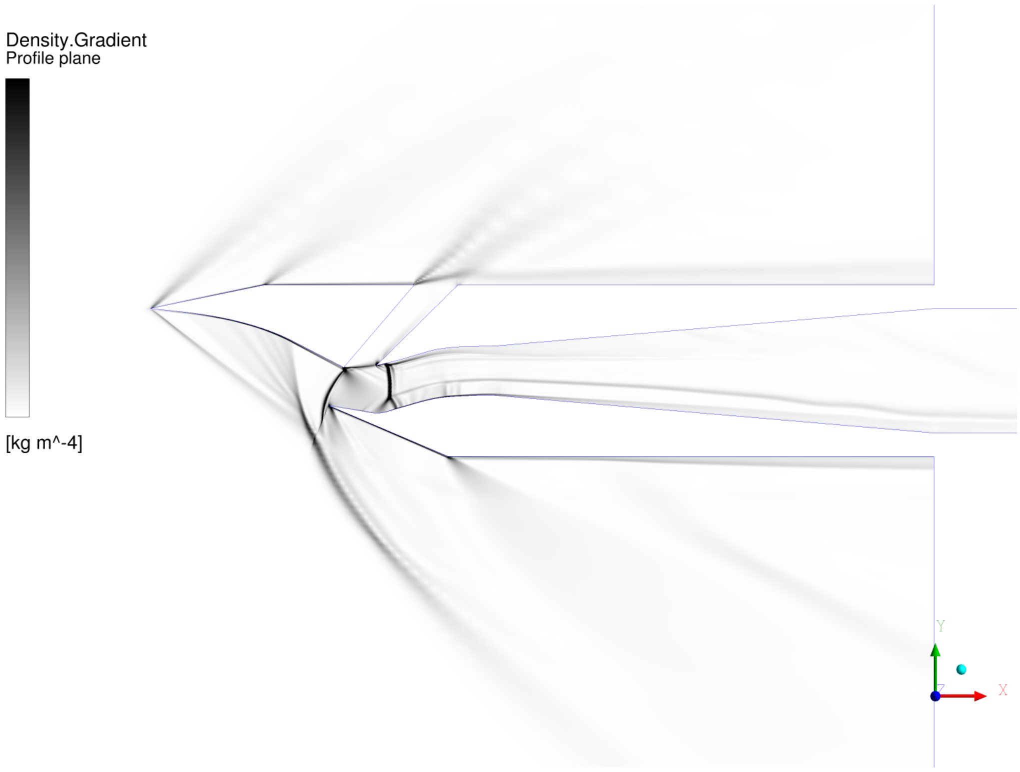
Density.Gradient
Profile plane
[kg m^-4]
Y
X

A.2 Subcritical operating range, $p_{1,5}$

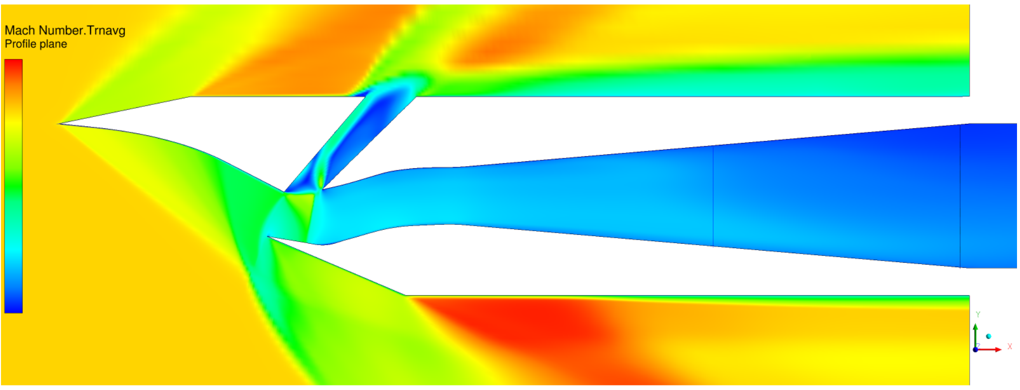

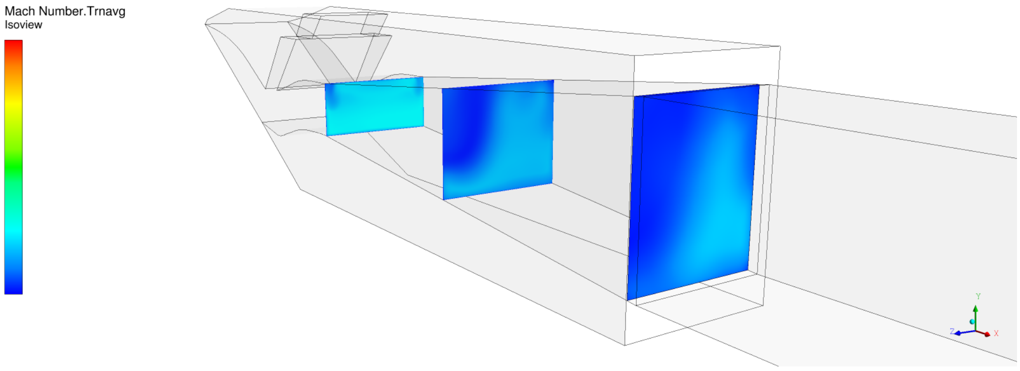

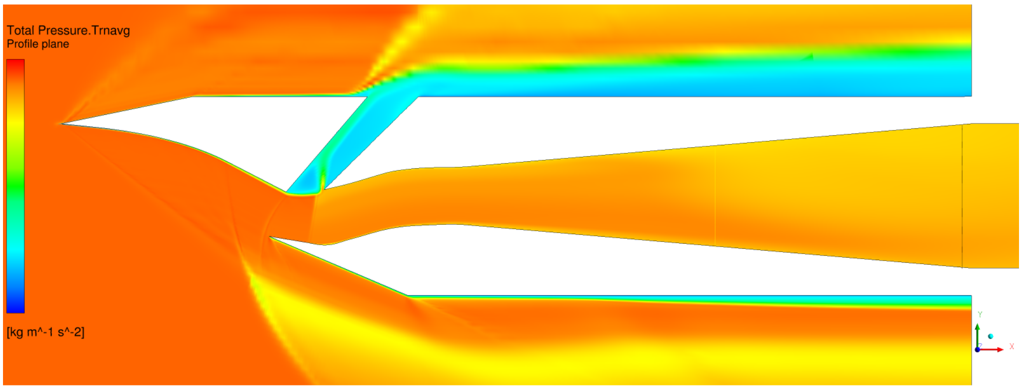

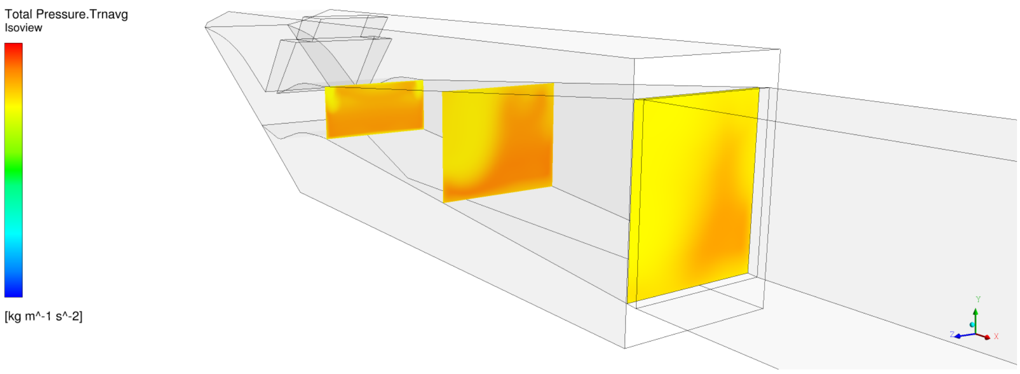

A.3 Supercritical operating range, $p_{1,1}$

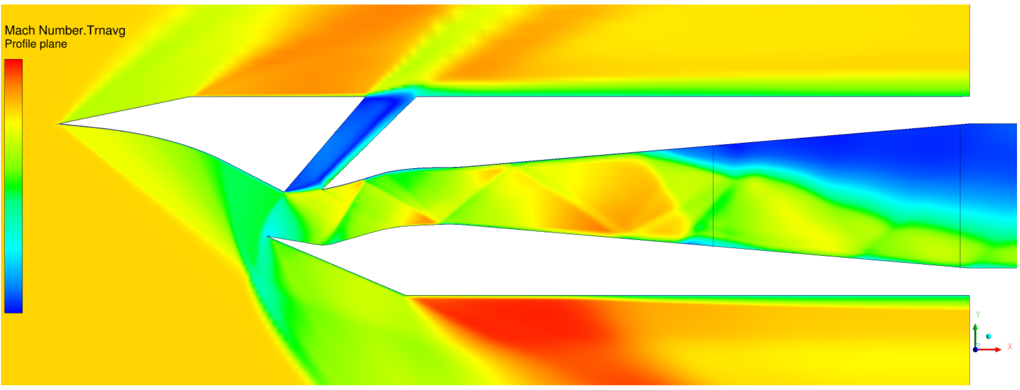

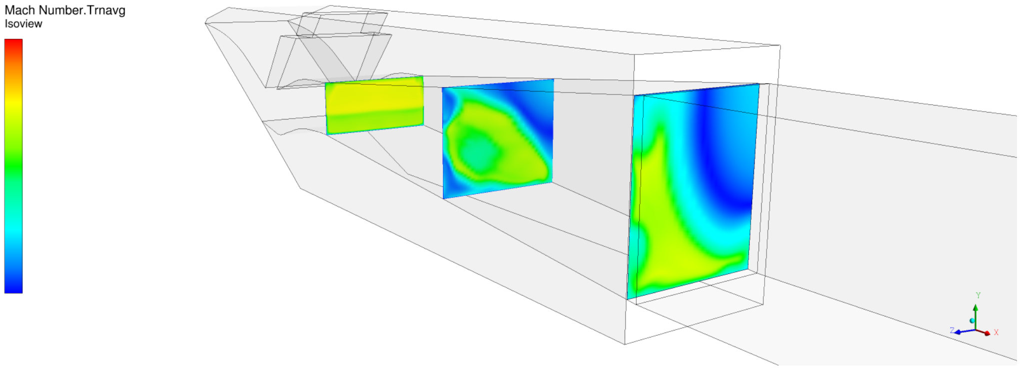

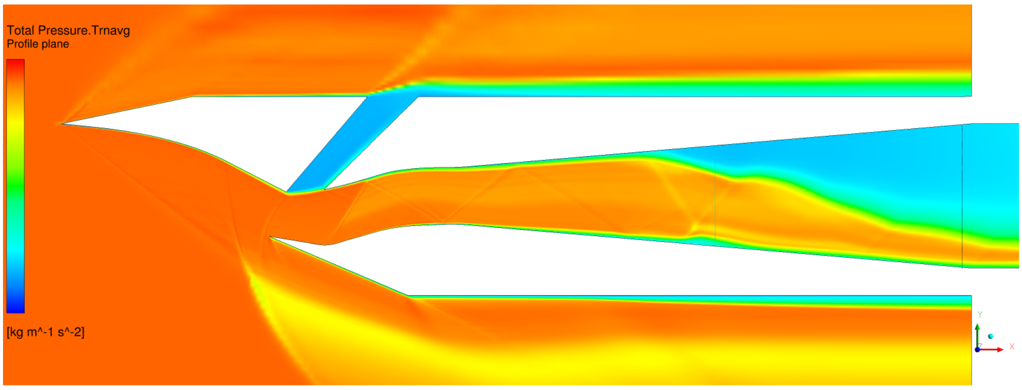

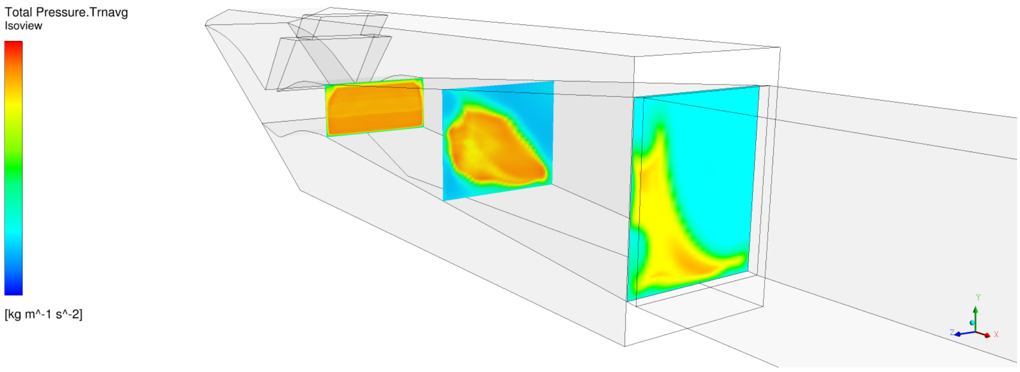

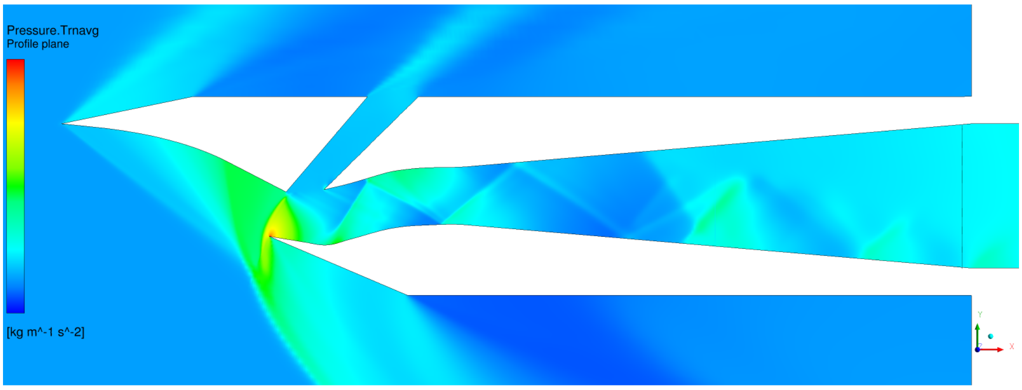
Pressure.Trnavg
Profile plane
[kg m^-1 s^-2]

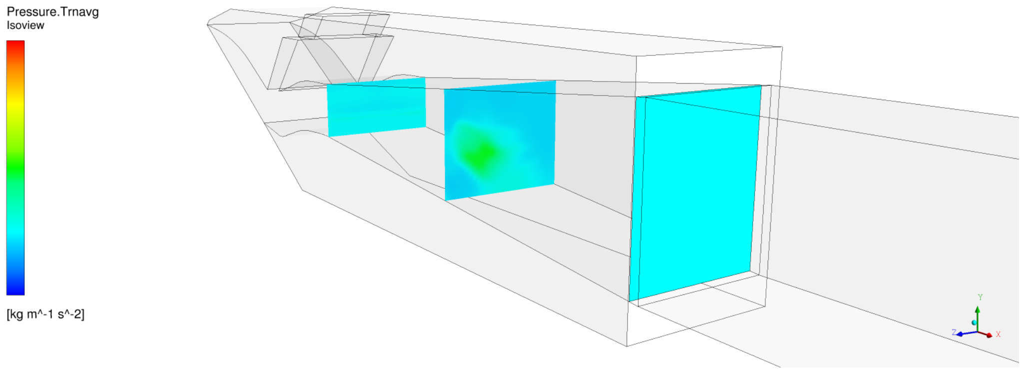
Pressure.Trnavg
Isoview
[kg m^-1 s^-2]

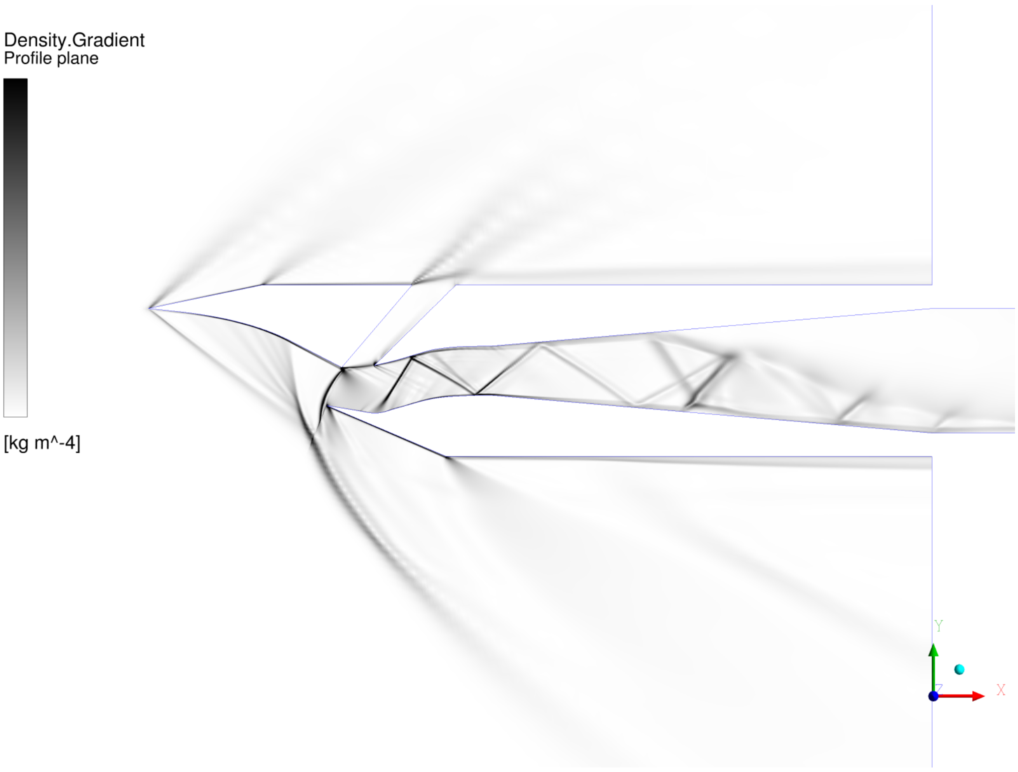
Density.Gradient
Profile plane
[kg m^-4]

B Validation study simulation, $M_{V,2}$

B.1 Critical operating point, $p_{2,4}$

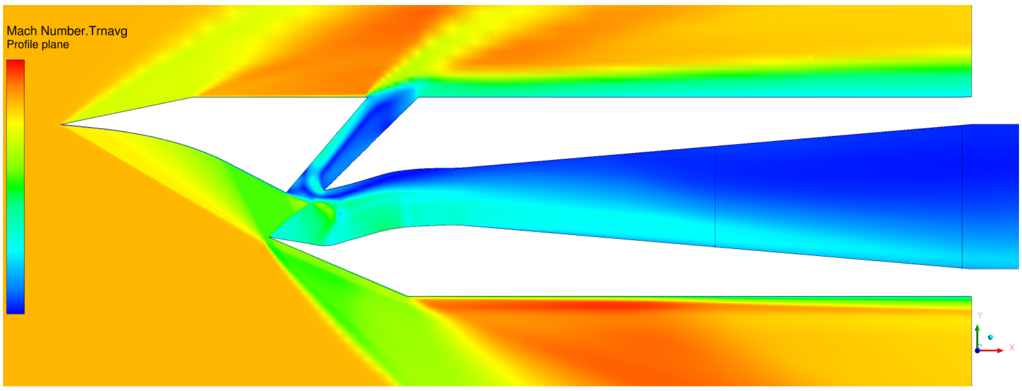

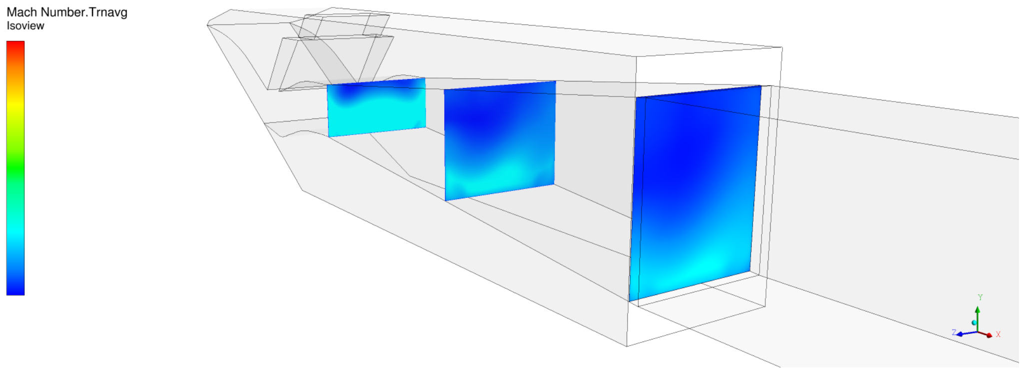

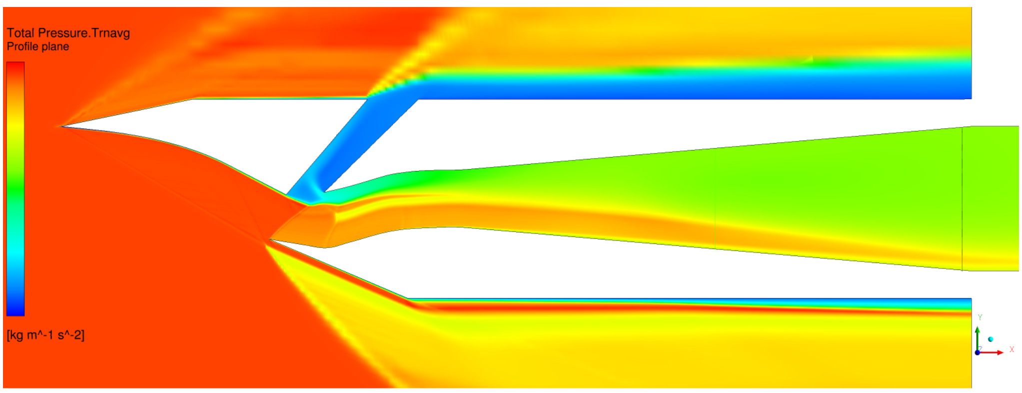

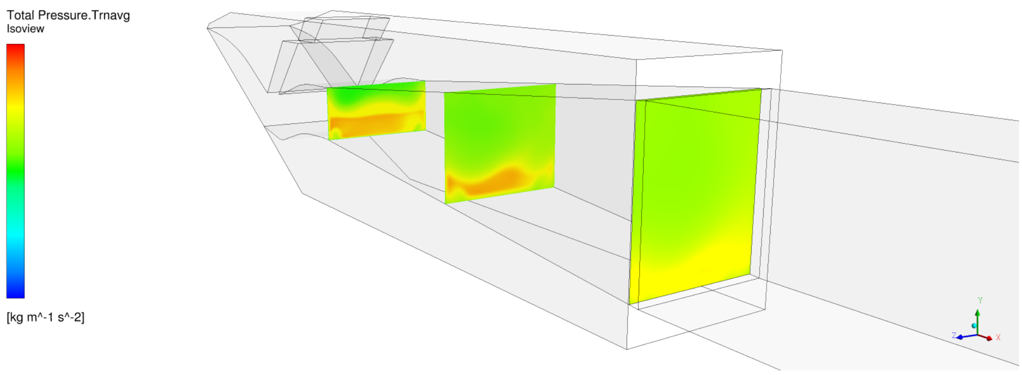

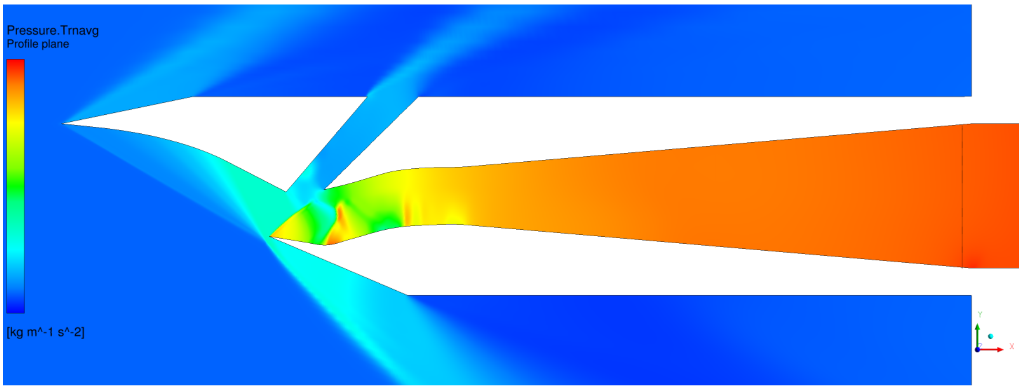
Pressure.Trnavg
Profile plane
[kg m^-1 s^-2]

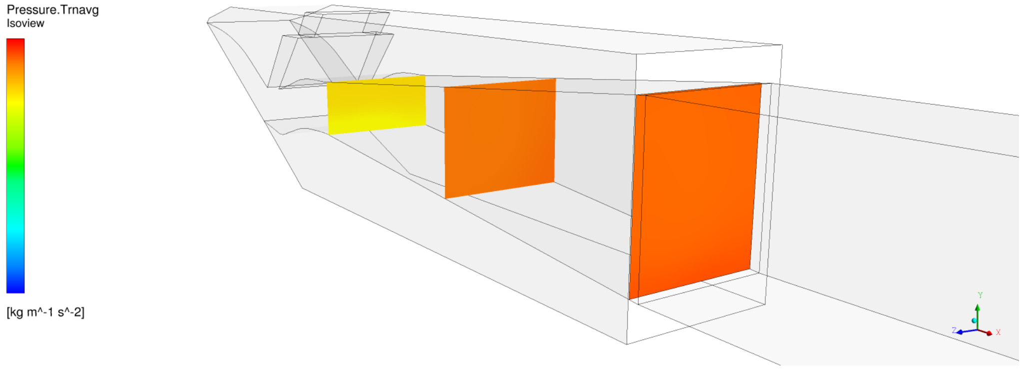
Pressure.Trnavg
Isoview
[kg m^-1 s^-2]

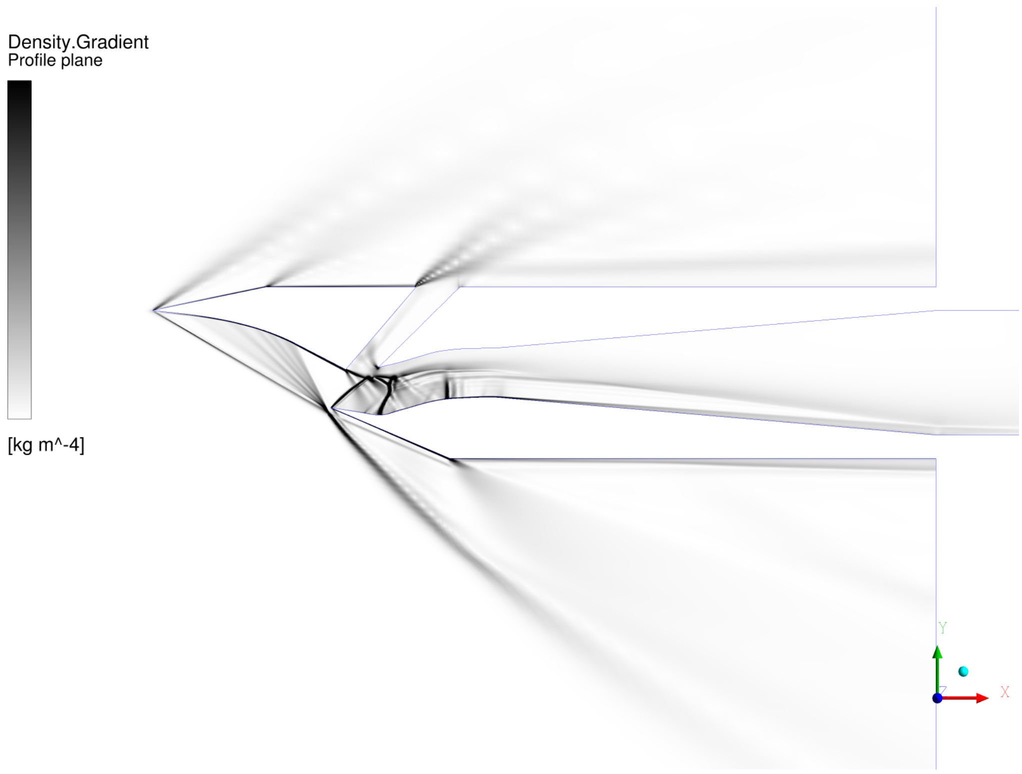
Density.Gradient
Profile plane
[kg m^-4]

B.2 Supercritical operating range, $p_{2,2}$

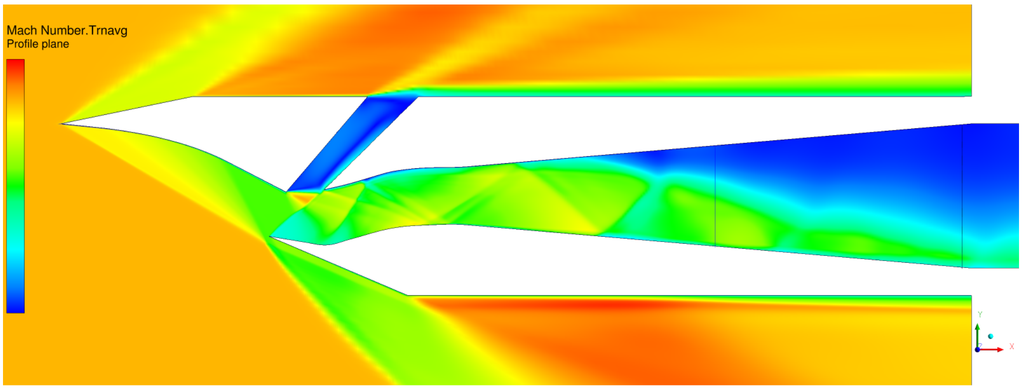

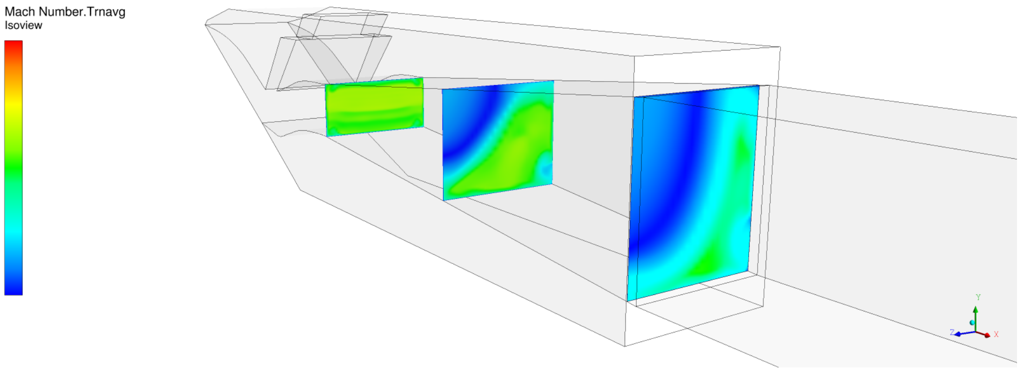

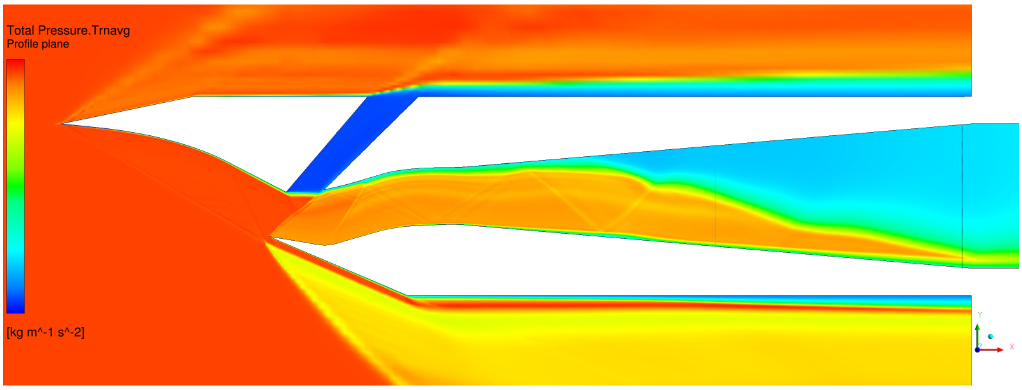

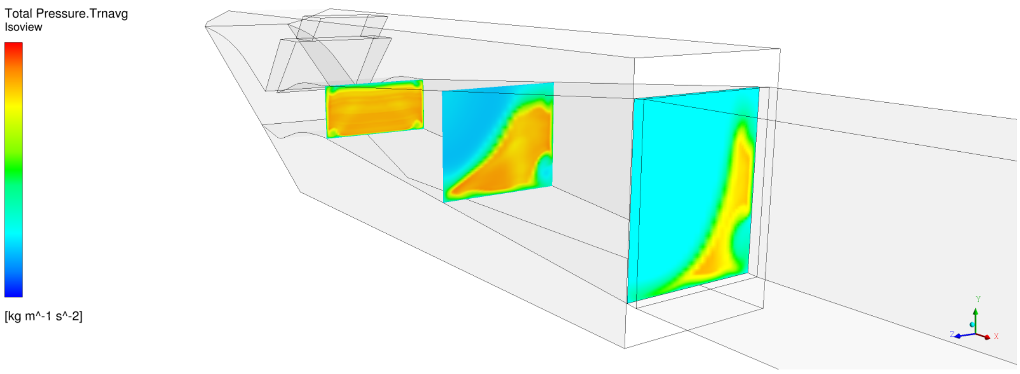

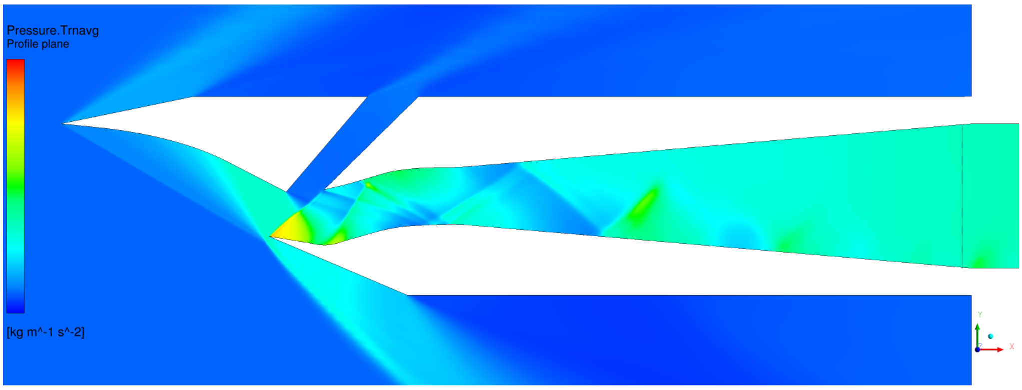
Pressure.Trnavg
Profile plane
[kg m^-1 s^-2]

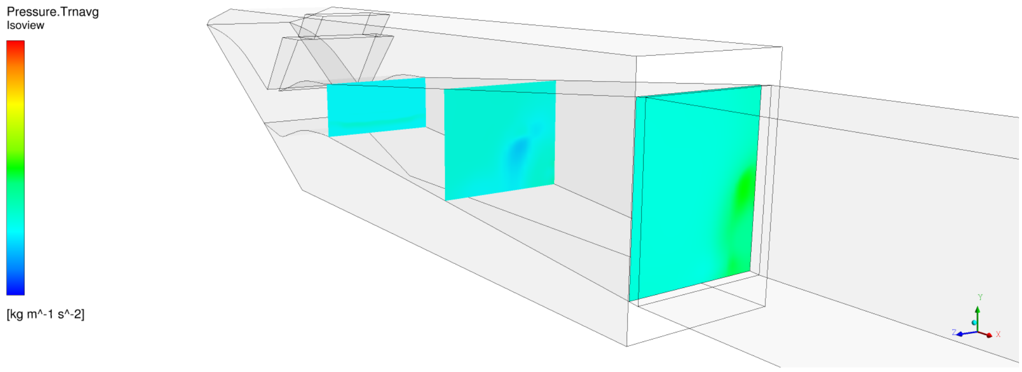
Pressure.Trnavg
Isoview
[kg m^-1 s^-2]

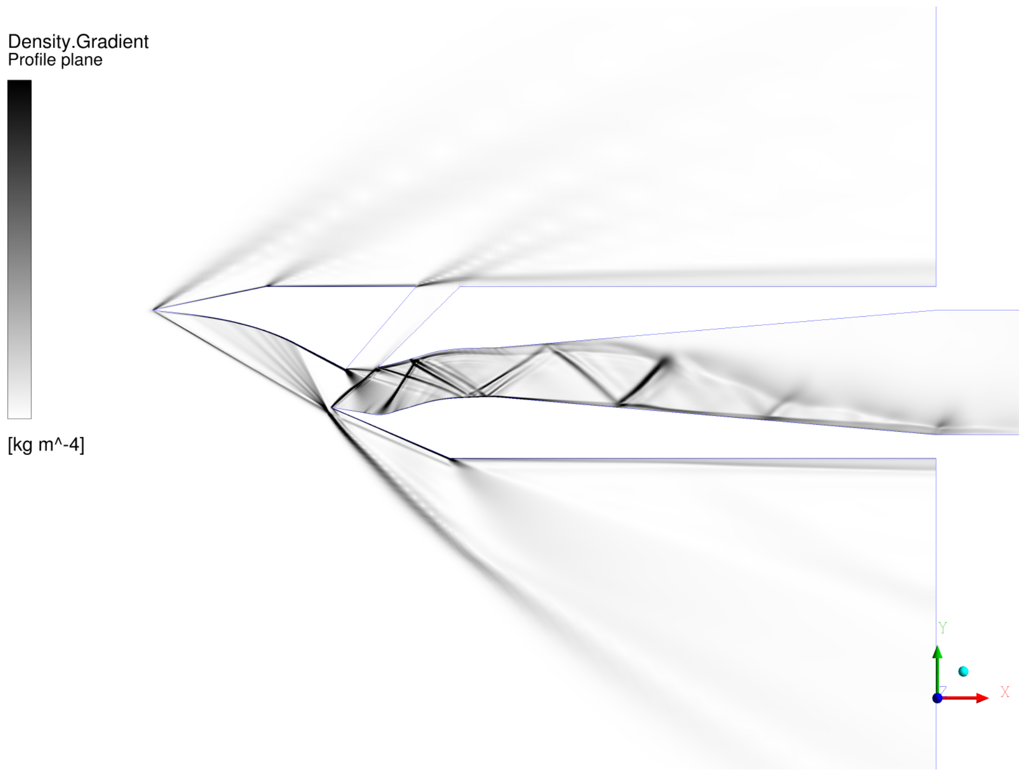
Density.Gradient
Profile plane
[kg m^-4]
Y
X

C Validation study simulation, $M_{V,3}$

C.1 Supercritical operating range, $p_{3,1}$, coarse/fine mesh

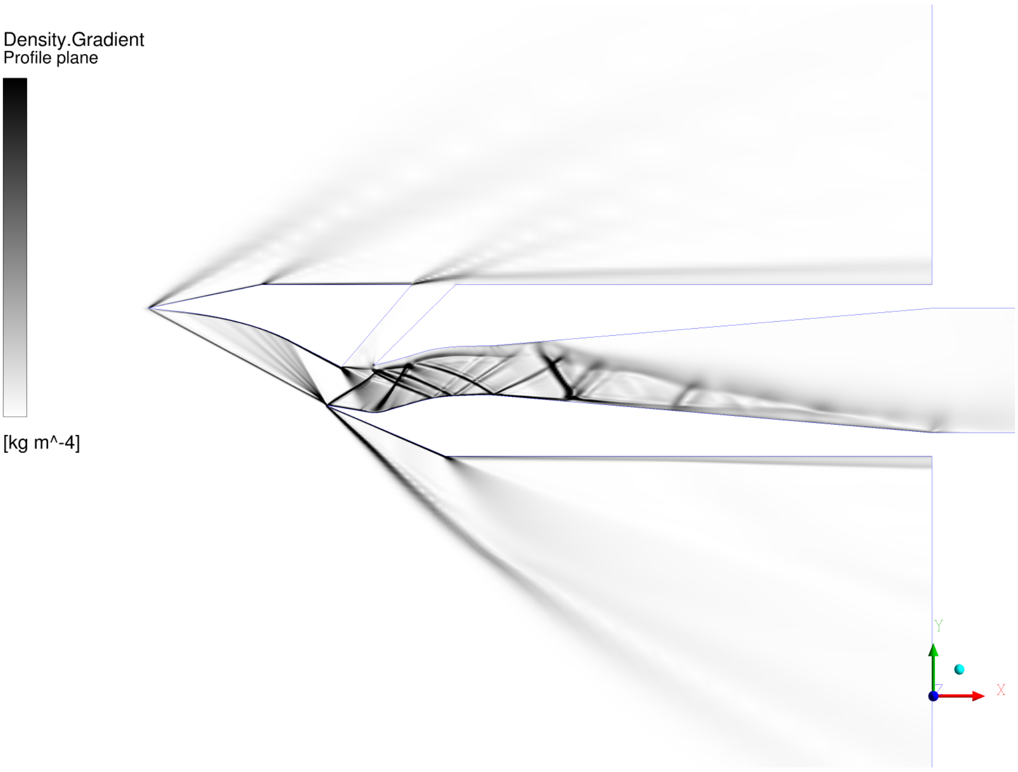

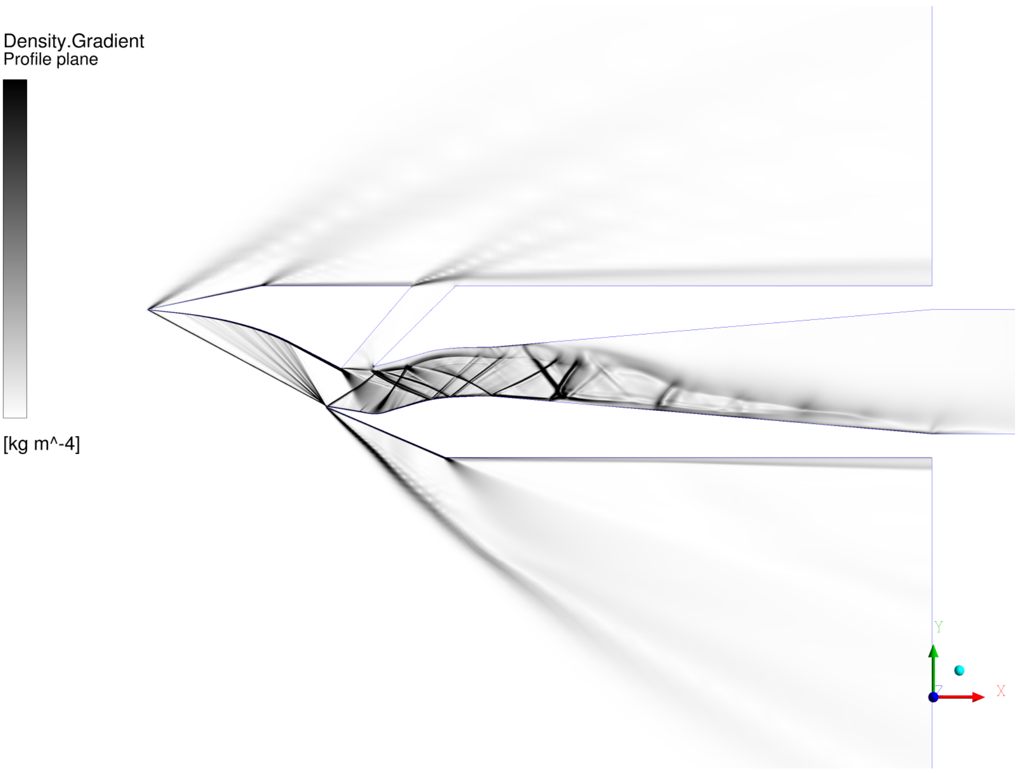

D Validation study simulation, $M_{V,4}$

D.1 Critical operating point, $p_{4,3}$

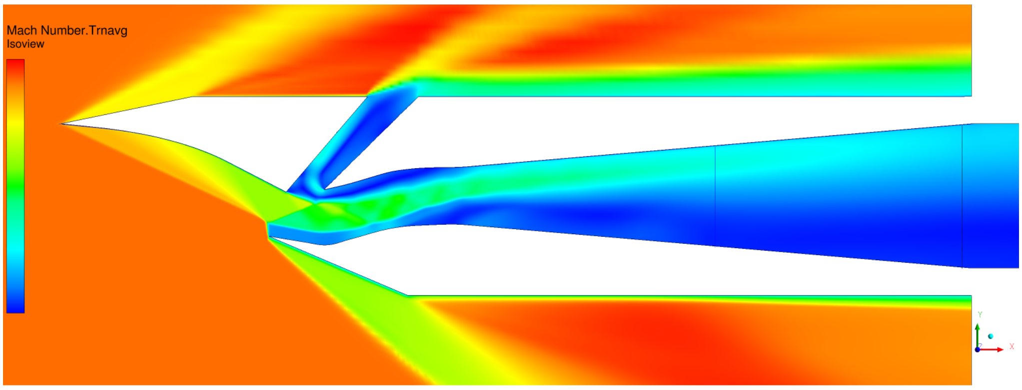

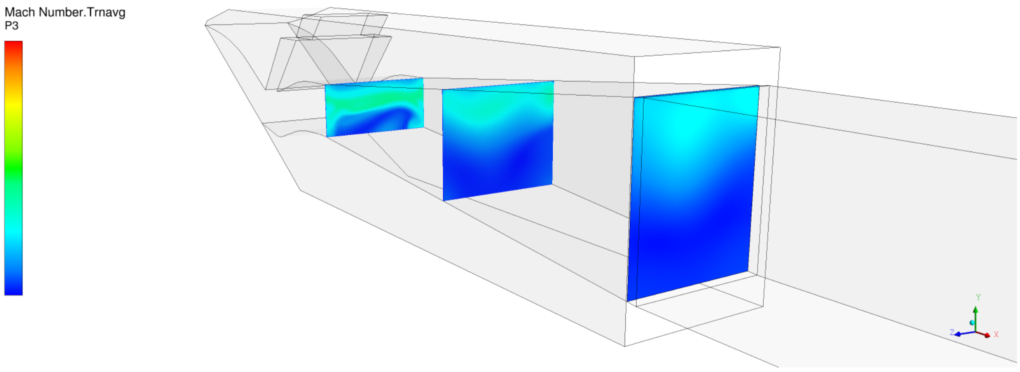

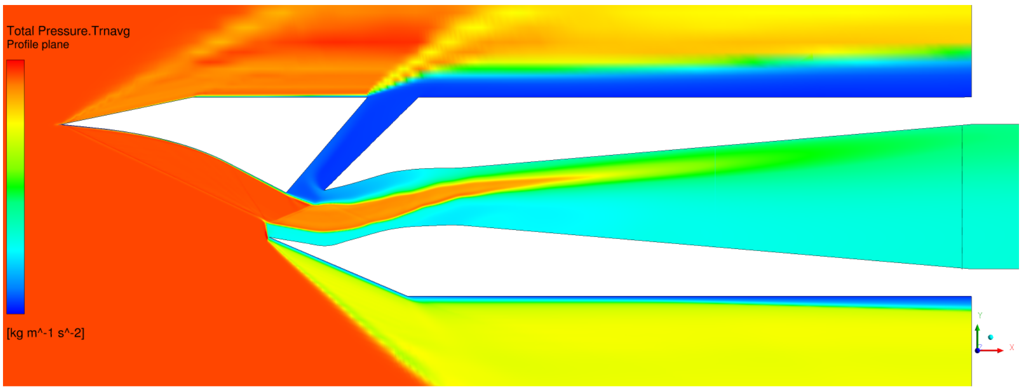

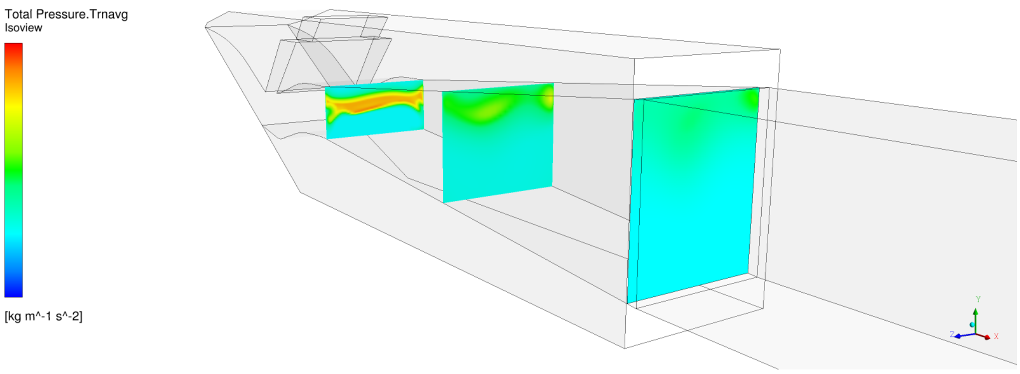

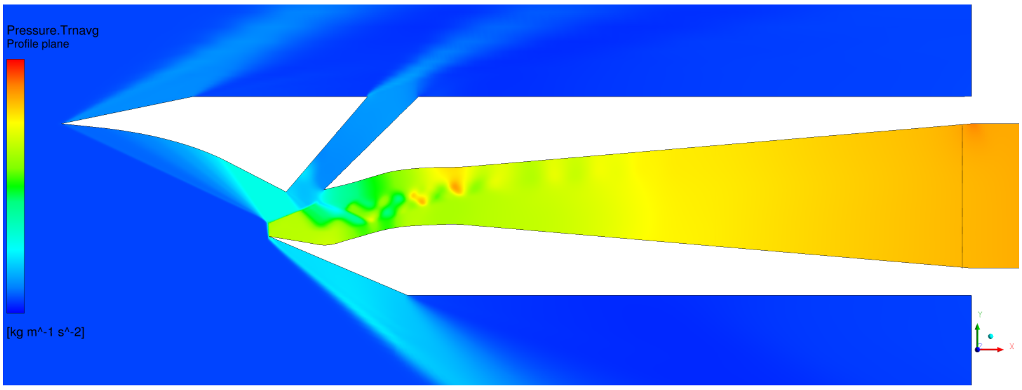
Pressure.Trnavg
Profile plane
[kg m^-1 s^-2]

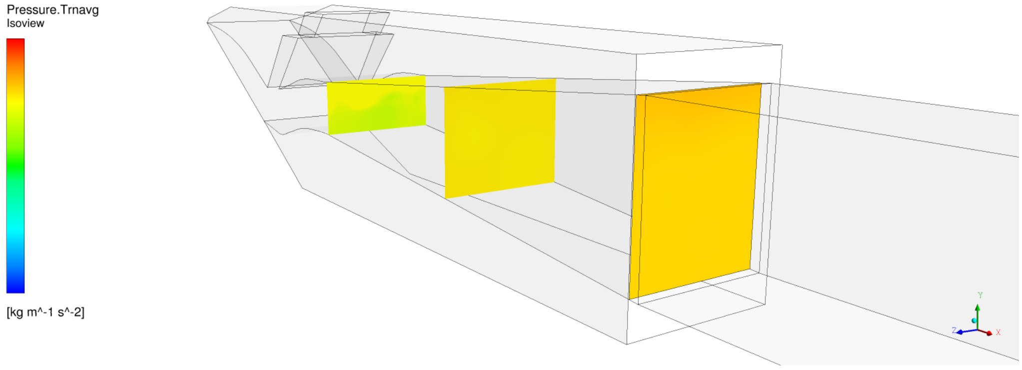
Pressure.Trnavg
Isoview
[kg m^-1 s^-2]

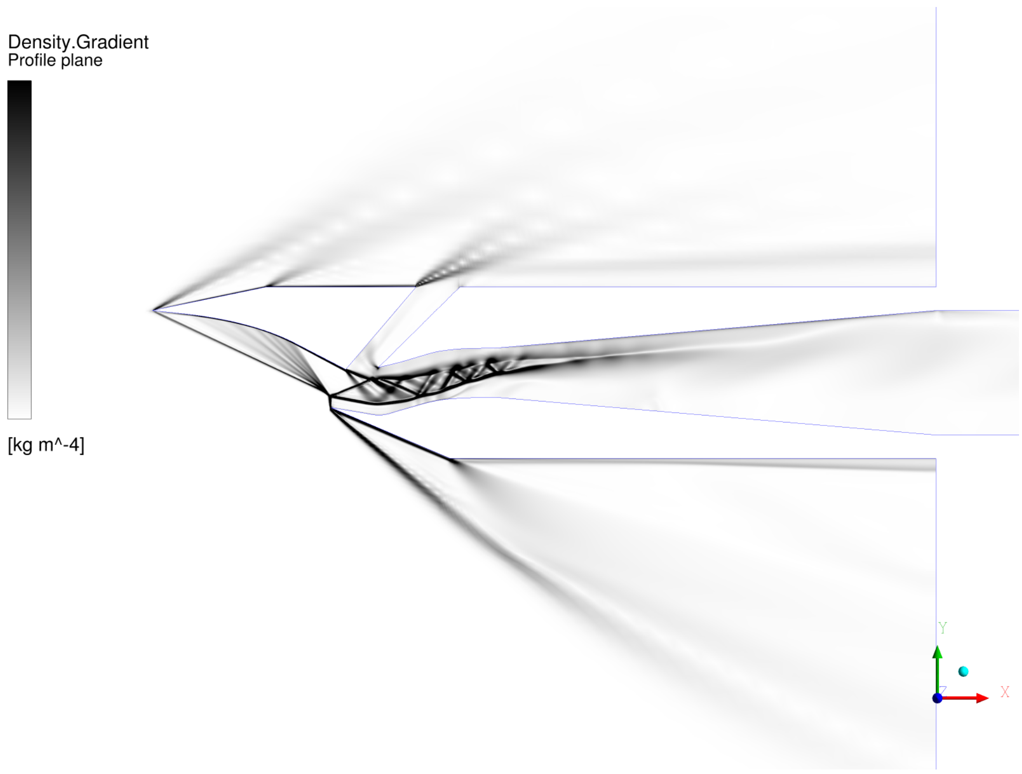
Density.Gradient
Profile plane
[kg m^-4]
Y
X

E Parametric study simulation, $M_{P,1}$

E.1 Critical operating point, $p_{1,3}$

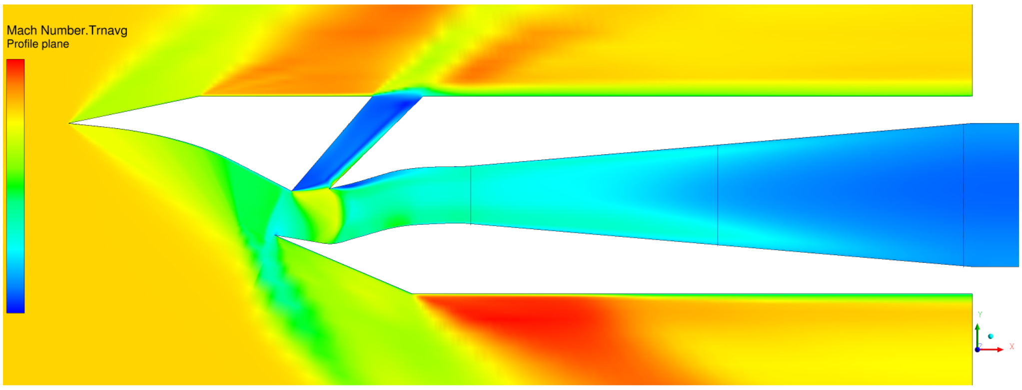

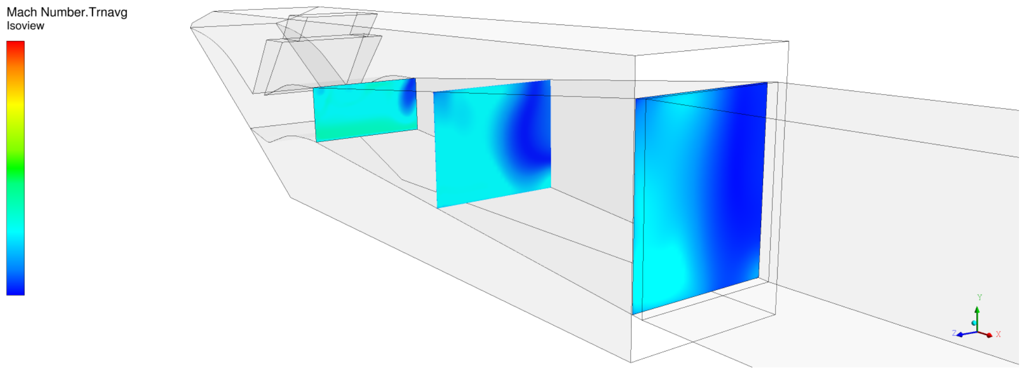

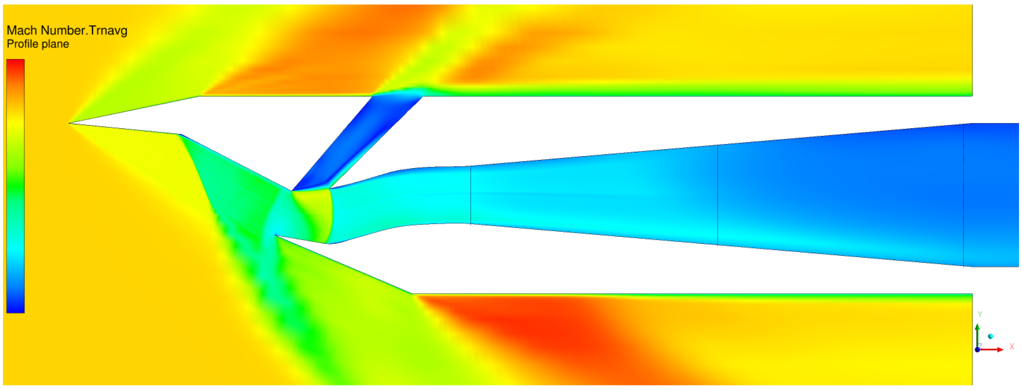

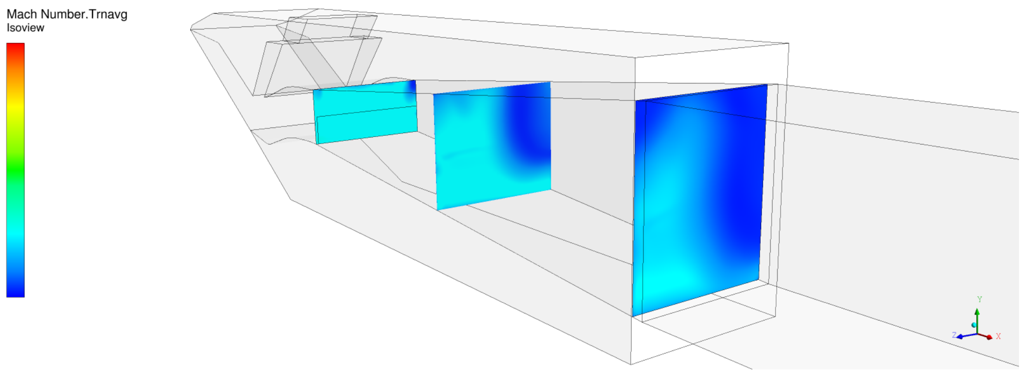

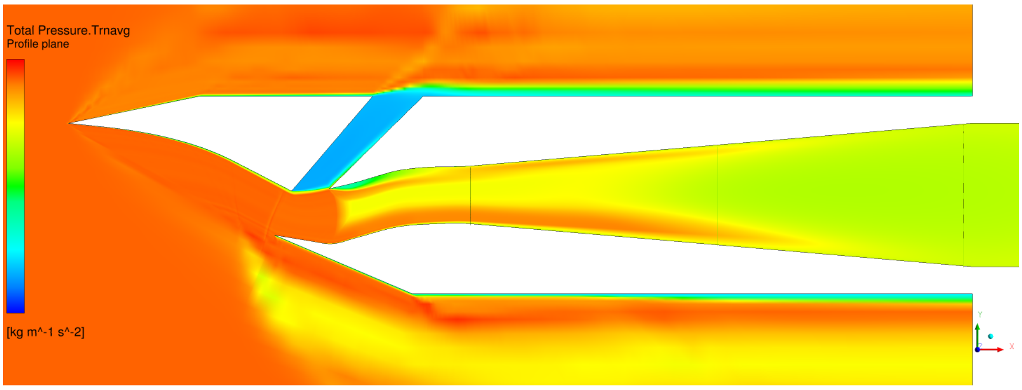
Total Pressure.Trnavg
Profile plane
[kg m^-1 s^-2]

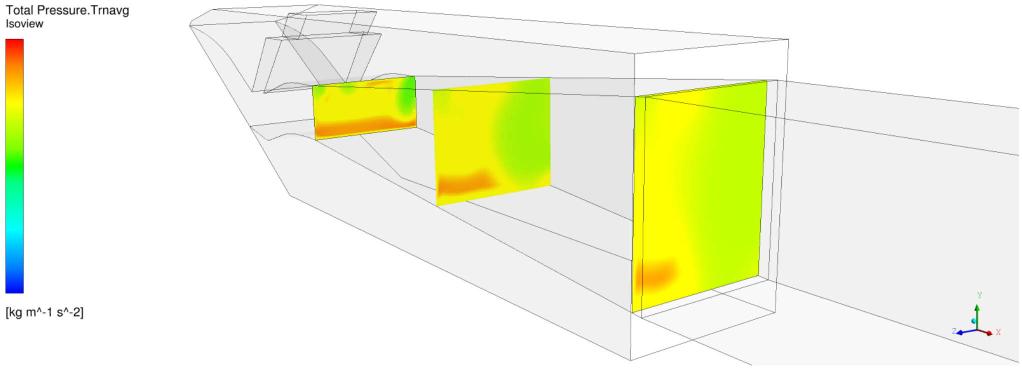
Total Pressure.Trnavg
Isoview
[kg m^-1 s^-2]

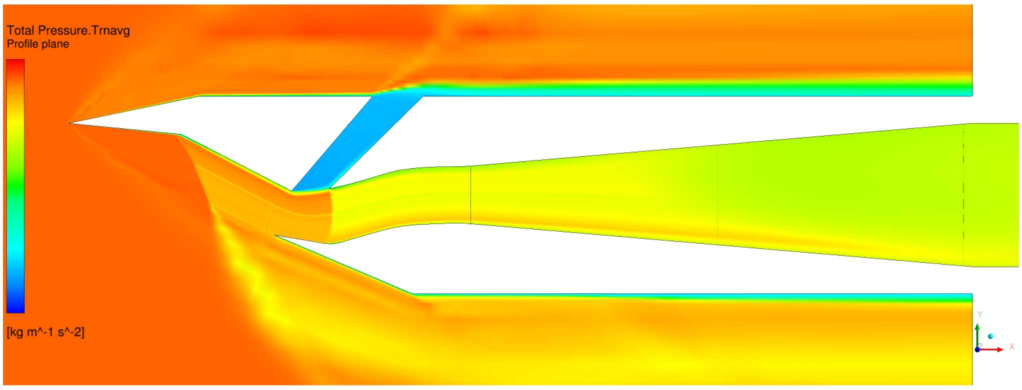
Total Pressure.Trnavg
Profile plane
[kg m^-1 s^-2]

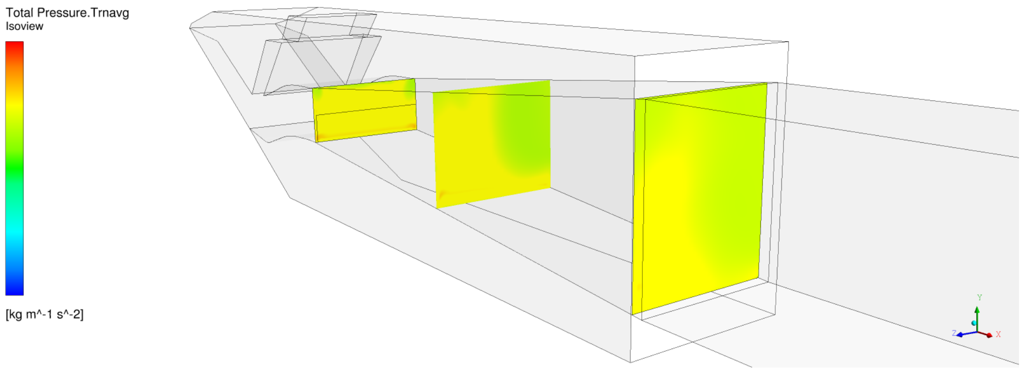
Total Pressure.Trnavg
Isoview
[kg m^-1 s^-2]

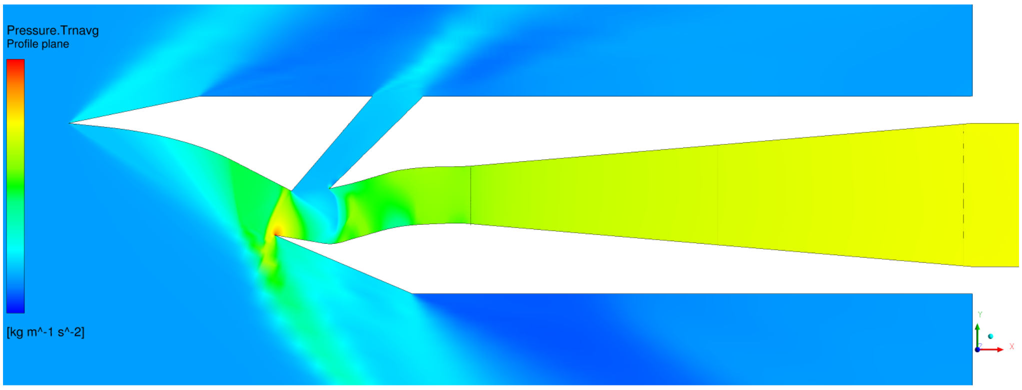
Pressure.Trnavg
Profile plane
[kg m^-1 s^-2]

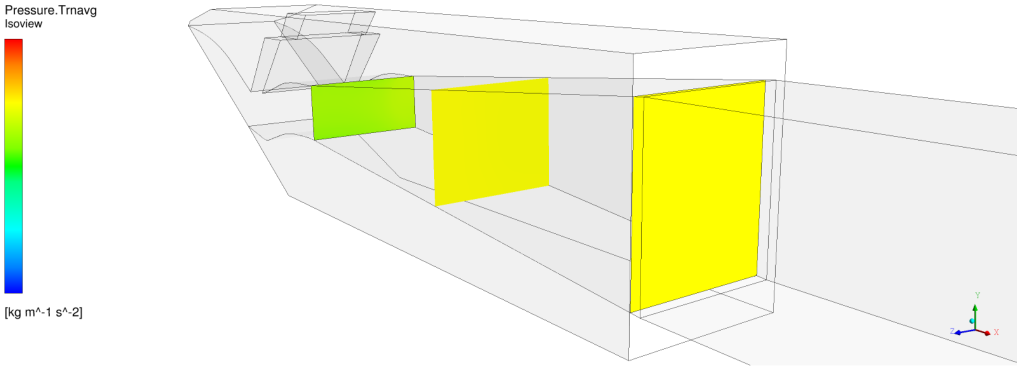
Pressure.Trnavg
Isoview
[kg m^-1 s^-2]

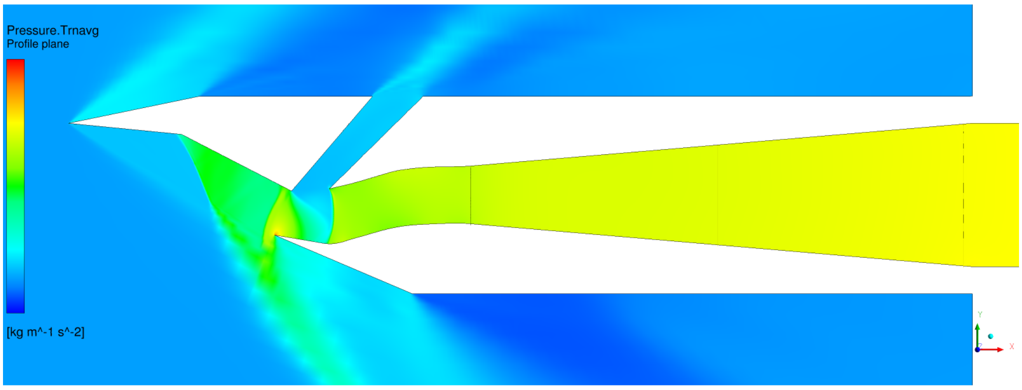
Pressure.Trnavg
Profile plane
[kg m^-1 s^-2]

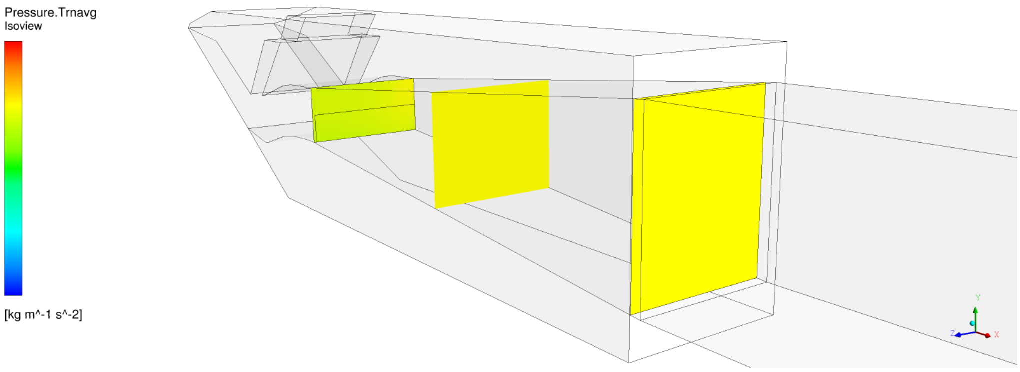
Pressure.Trnavg
Isoview
[kg m^-1 s^-2]

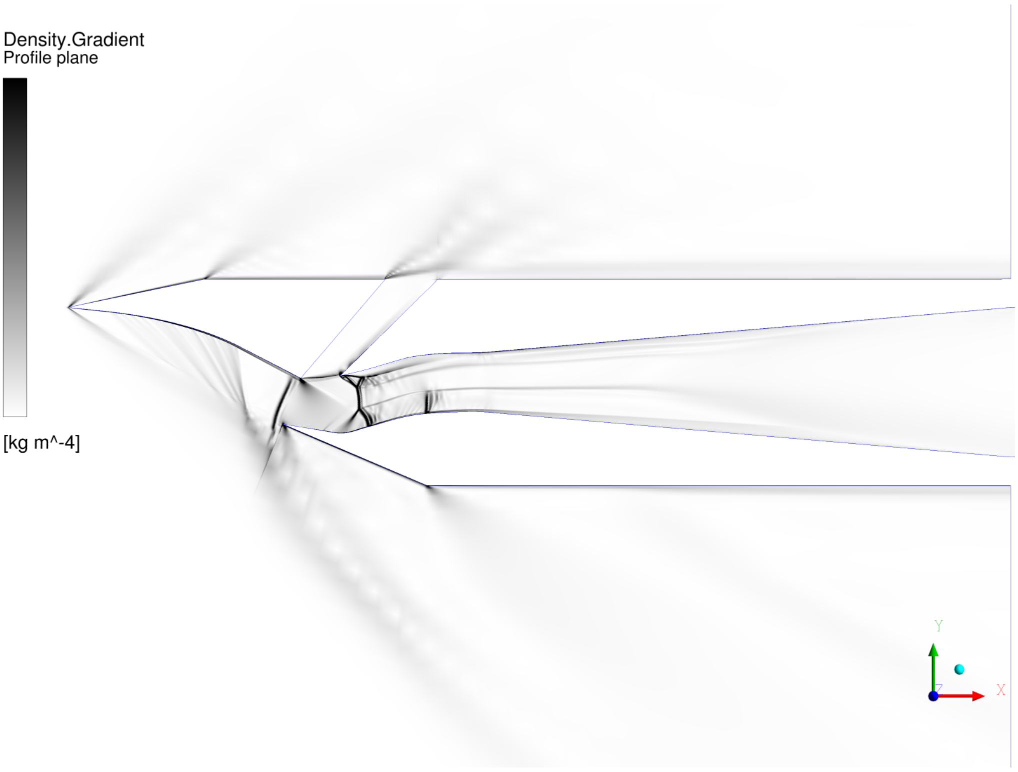
Density.Gradient
Profile plane
[kg m^-4]
Y
X

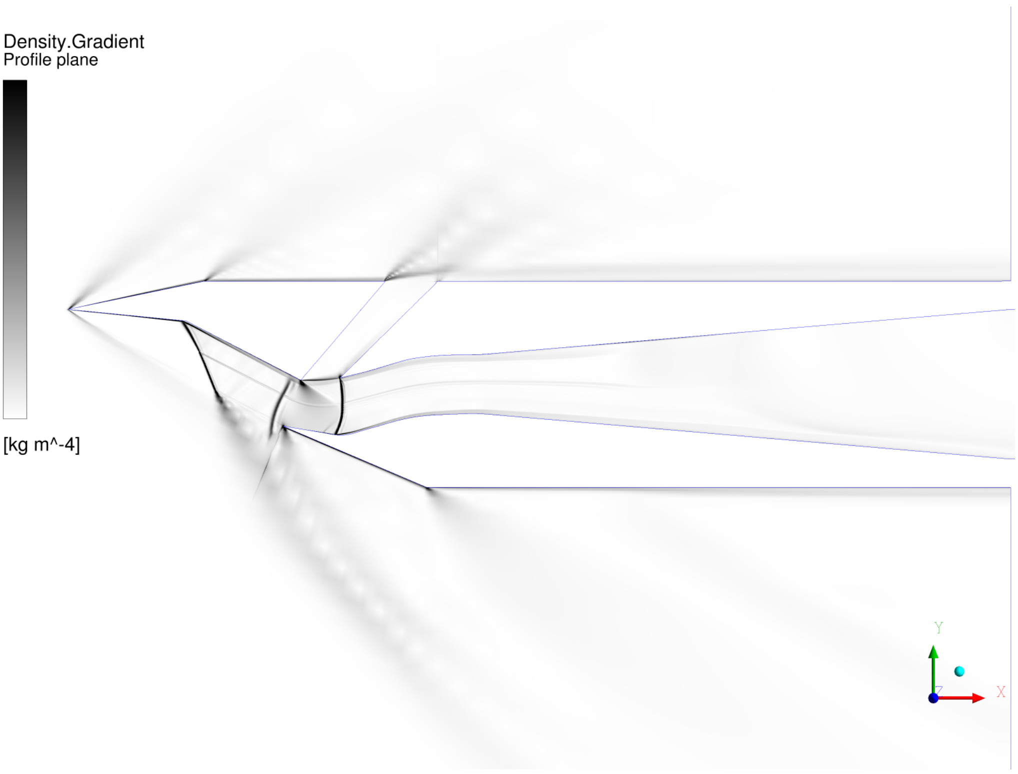
Density.Gradient
Profile plane
[kg m^-4]
Y
X

E.2 Subcritical operating range, $p_{1,5}$

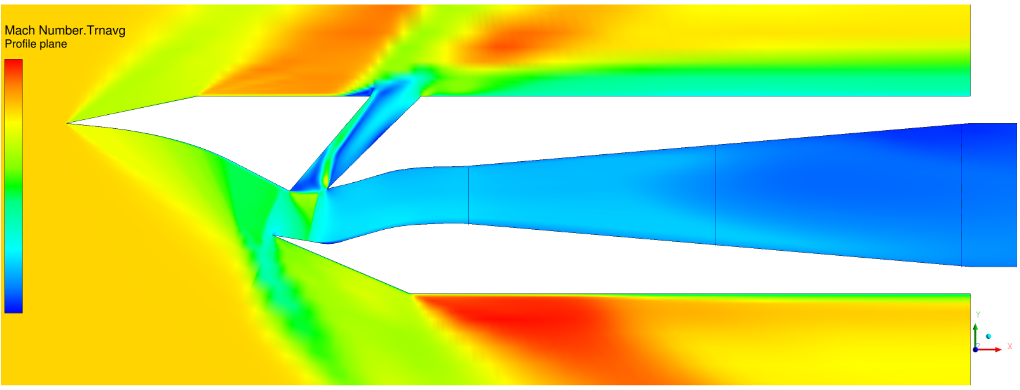

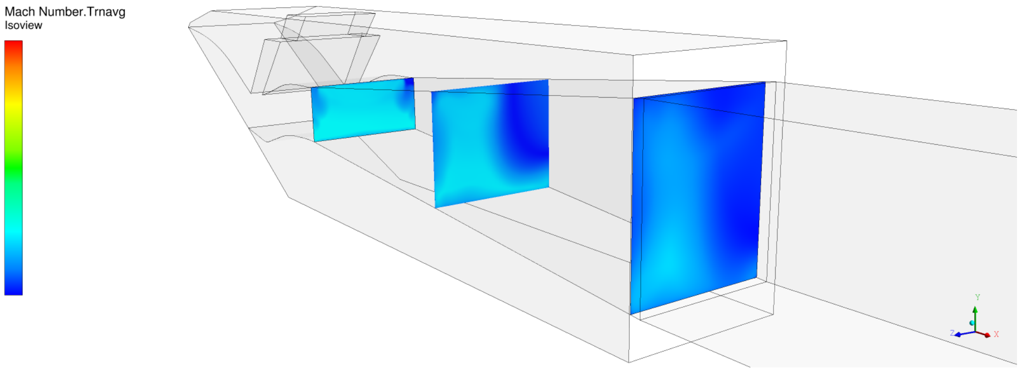

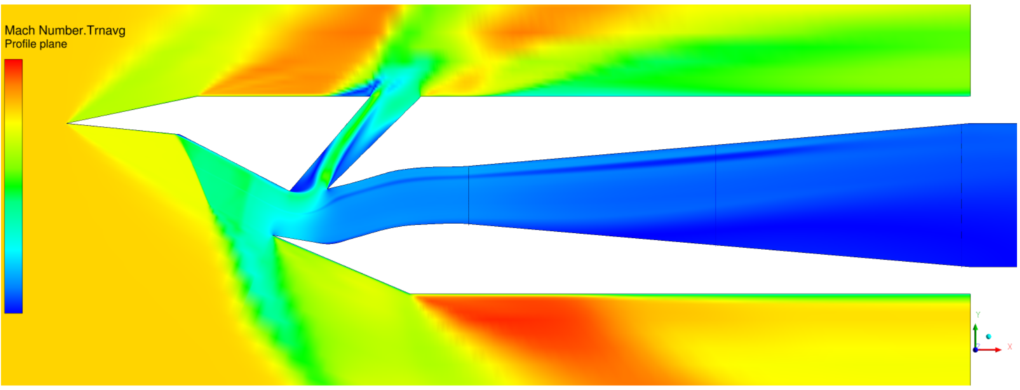

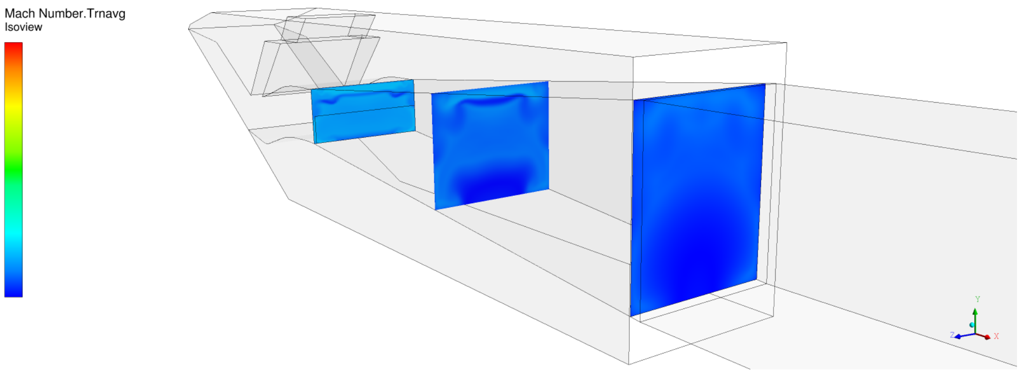

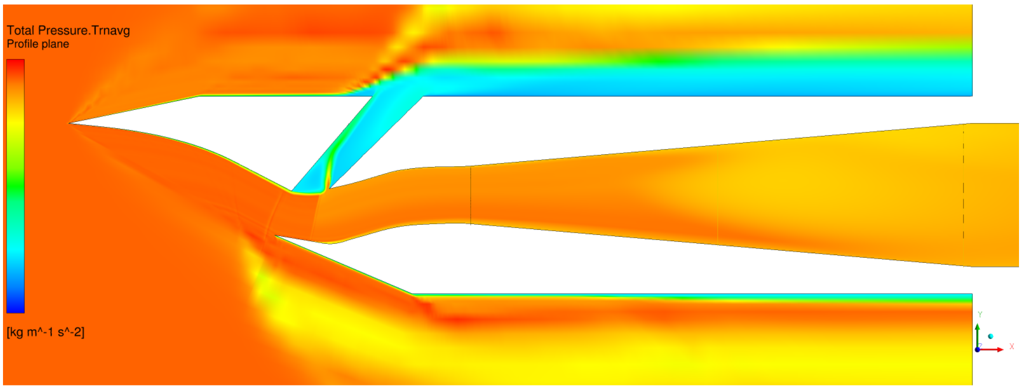
Total Pressure.Trnavg
Profile plane
[kg m^-1 s^-2]

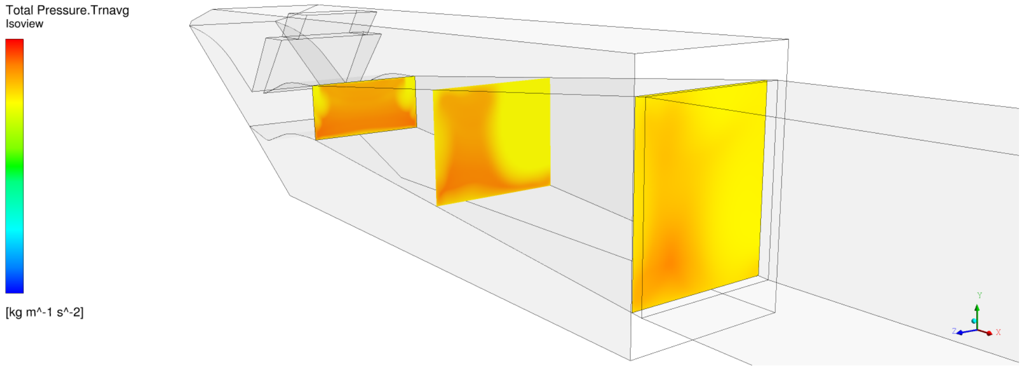
Total Pressure.Trnavg
Isoview
[kg m^-1 s^-2]

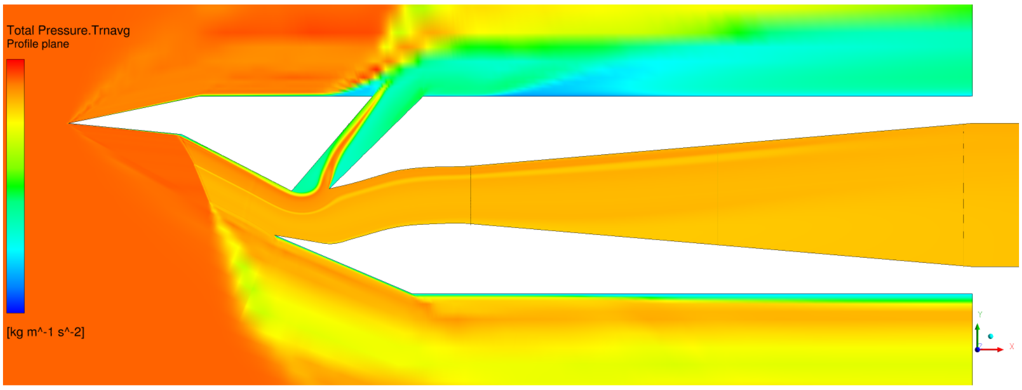
Total Pressure.Trnavg
Profile plane
[kg m^-1 s^-2]

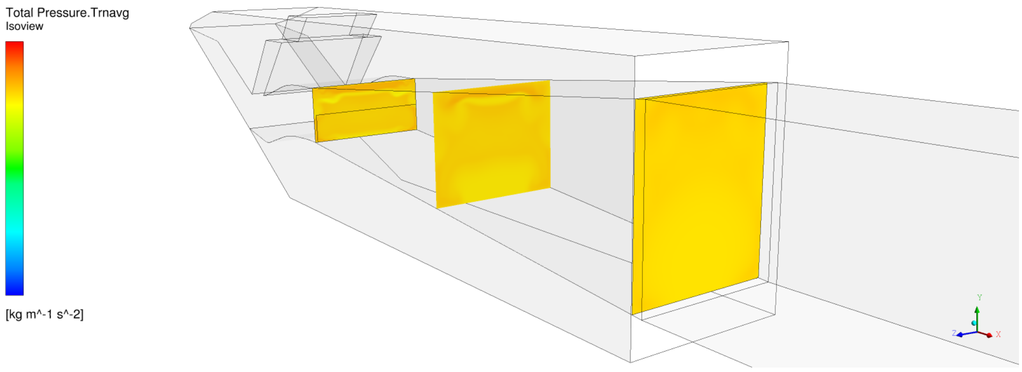
Total Pressure.Trnavg
Isoview
[kg m^-1 s^-2]

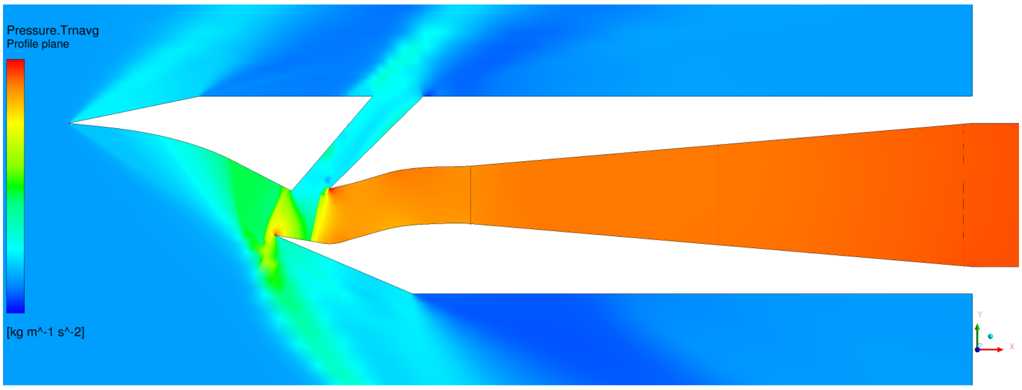
Pressure.Trnavg
Profile plane
[kg m^-1 s^-2]

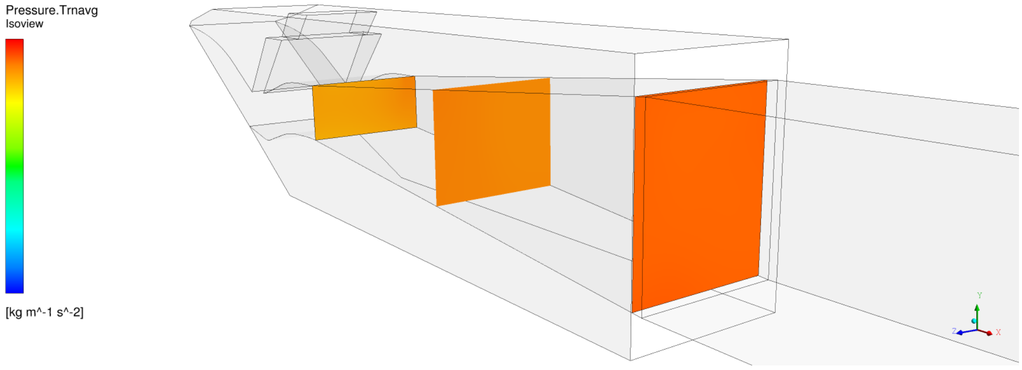
Pressure.Trnavg
Isoview
[kg m^-1 s^-2]

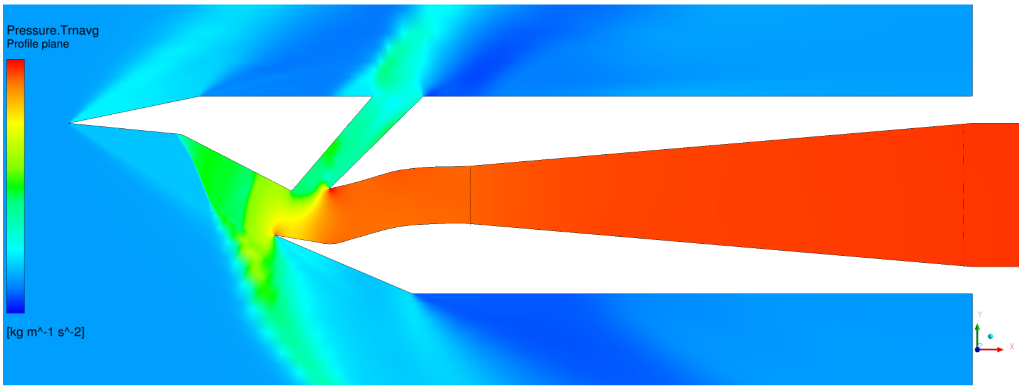
Pressure.Trnavg
Profile plane
[kg m^-1 s^-2]

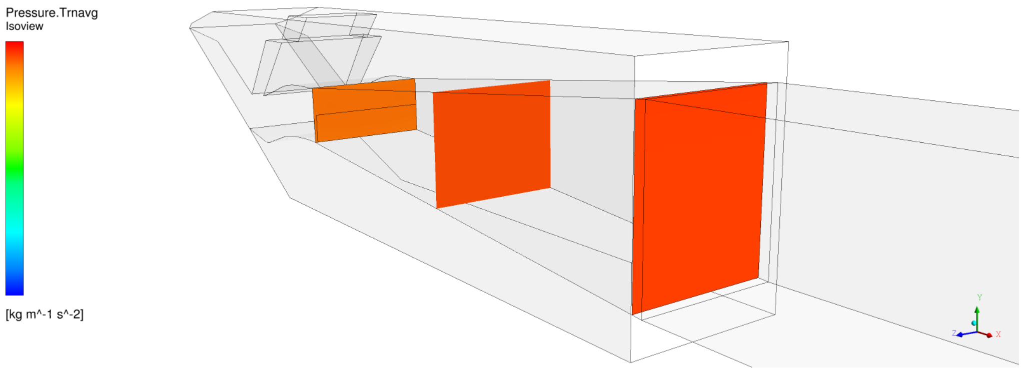
Pressure.Trnavg
Isoview
[kg m^-1 s^-2]

E.3 Supercritical operating range, $p_{1,1}$

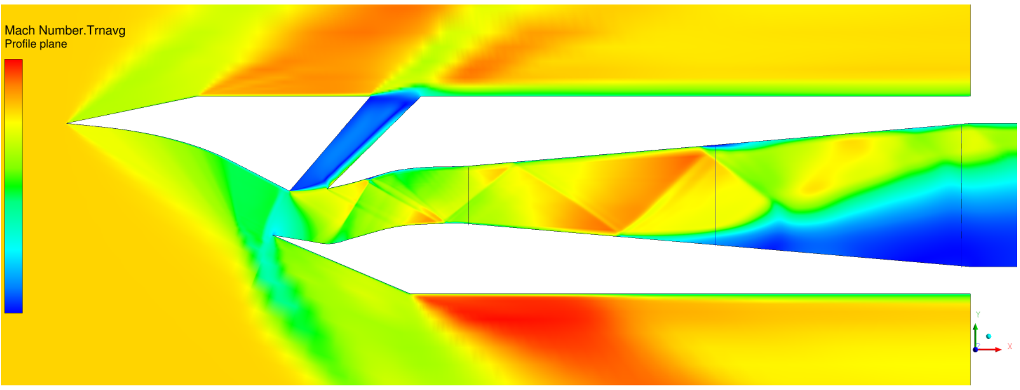

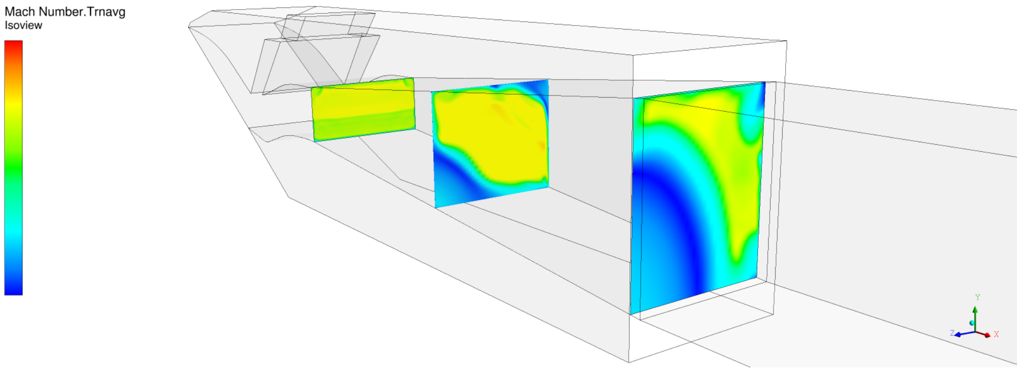

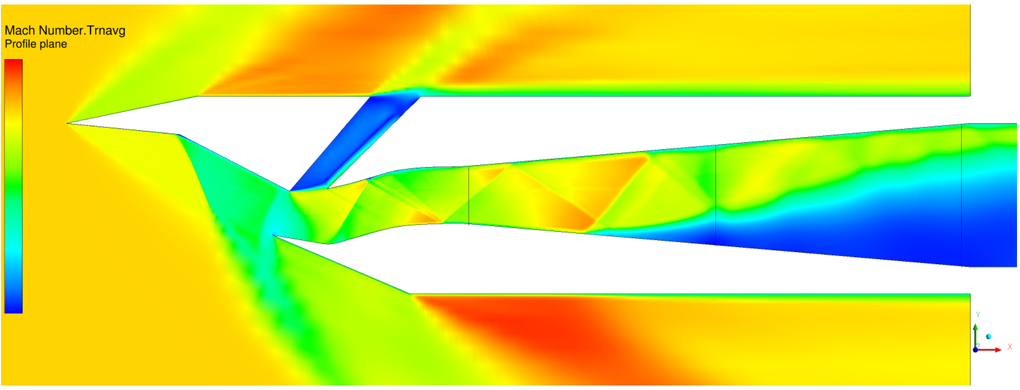

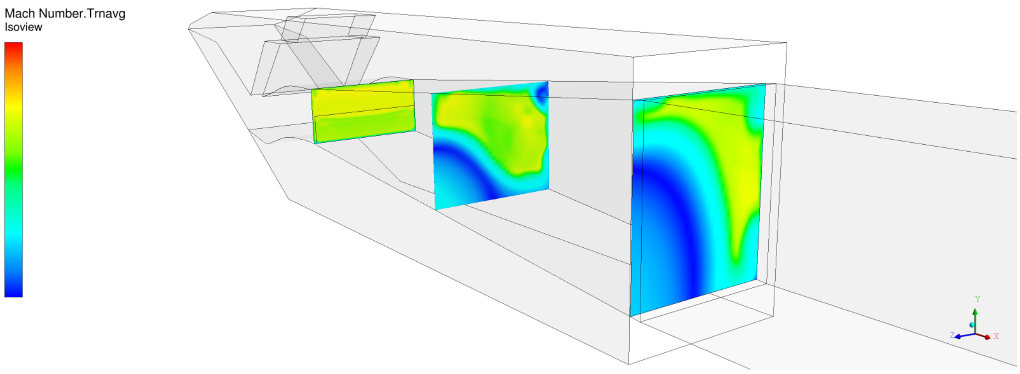

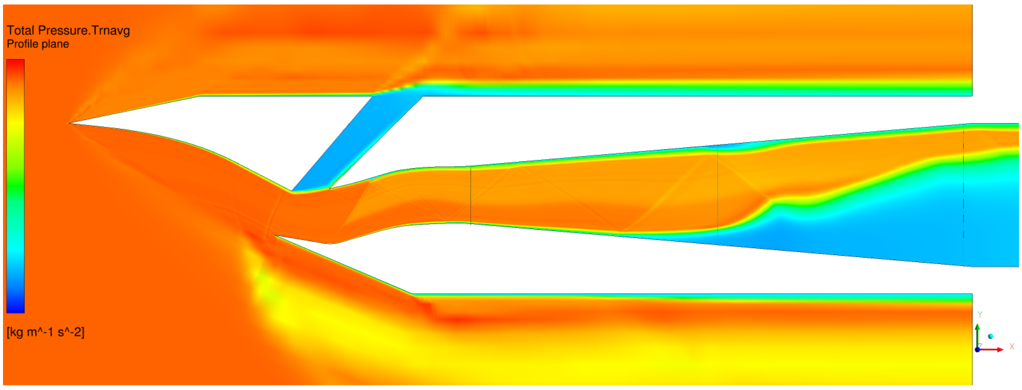
Total Pressure.Trnavg
Profile plane
[kg m^-1 s^-2]

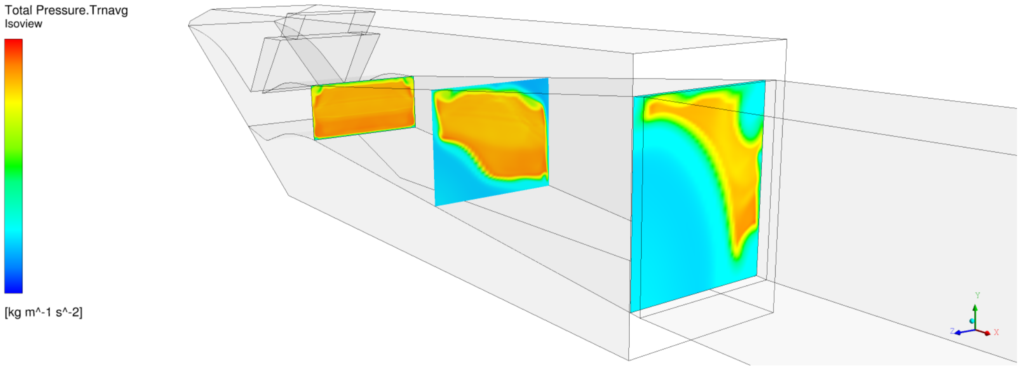
Total Pressure.Trnavg
Isoview
[kg m^-1 s^-2]

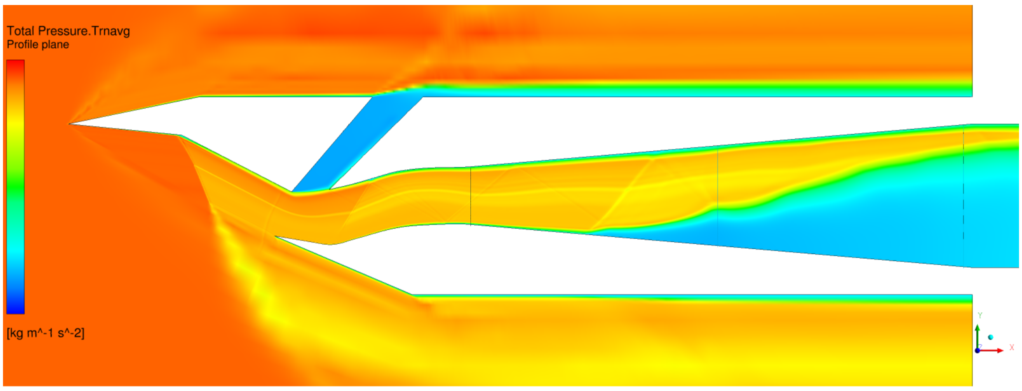
Total Pressure.Trnavg
Profile plane
[kg m^-1 s^-2]

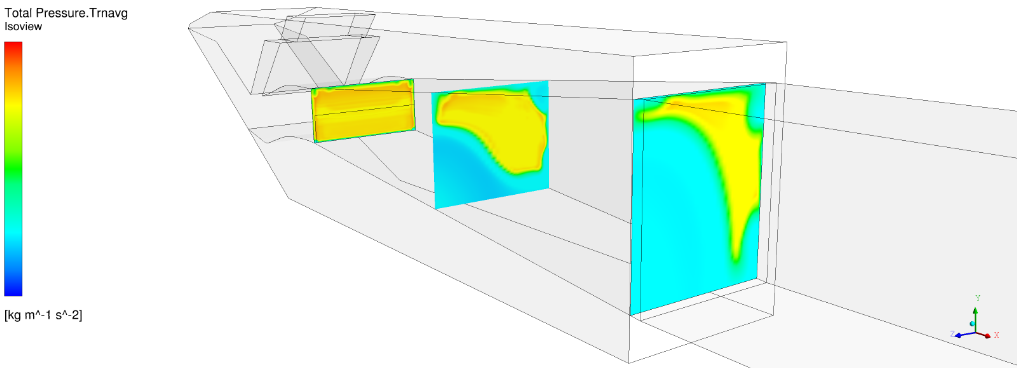
Total Pressure.Trnavg
Isoview
[kg m^-1 s^-2]

F Parametric study simulation, $M_{P,2}$

F.1 Supercritical operating range, $p_{2,1}$

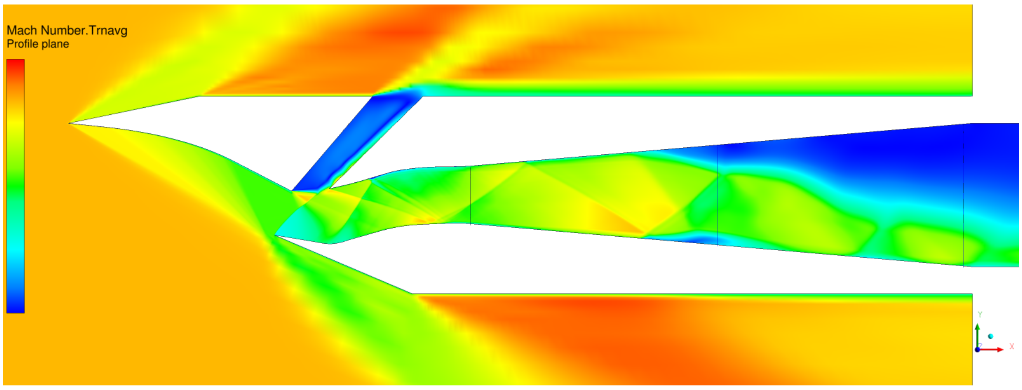

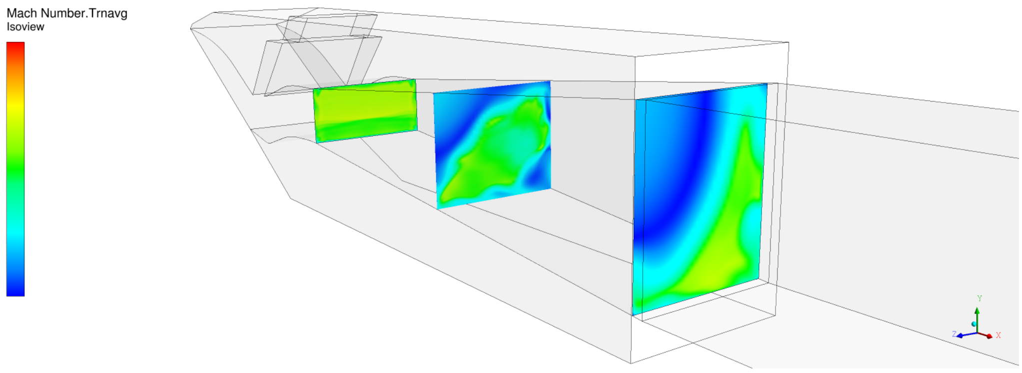

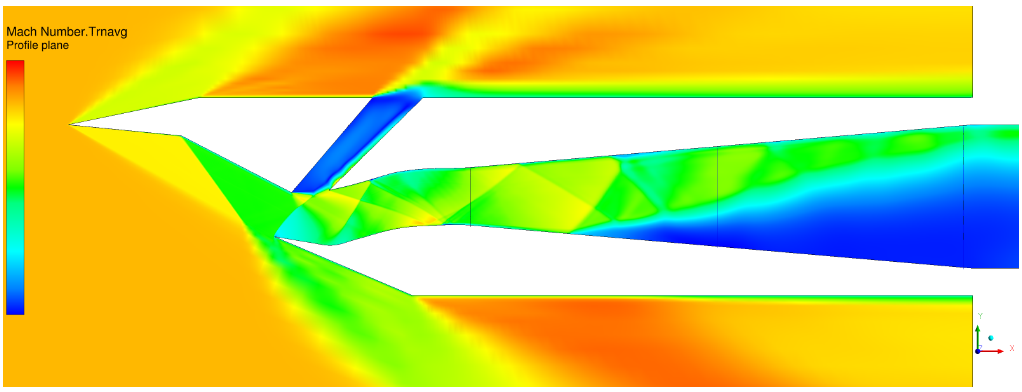

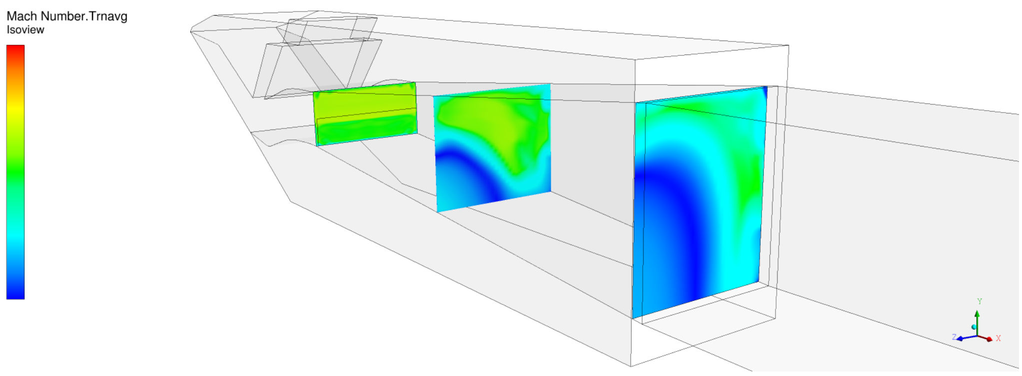

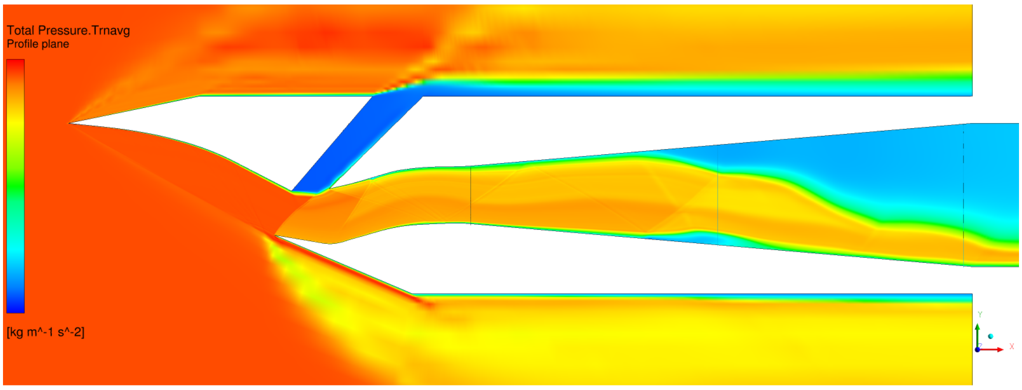
Total Pressure.Trnavg
Profile plane
[kg m^-1 s^-2]

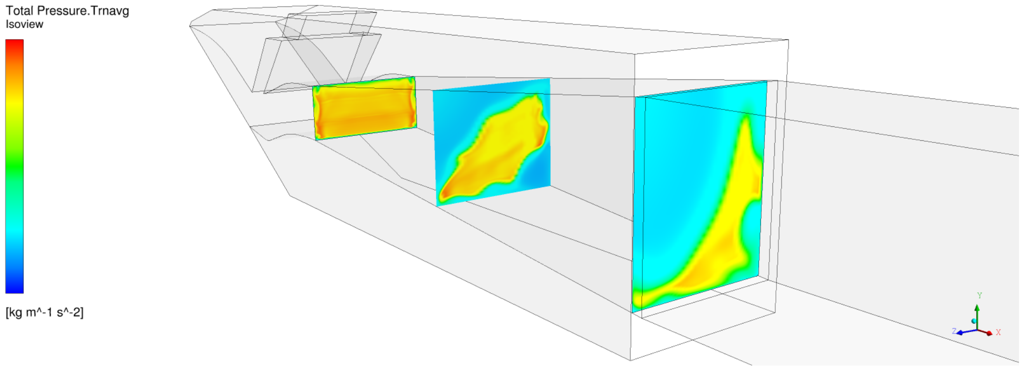
Total Pressure.Trnavg
Isoview
[kg m^-1 s^-2]

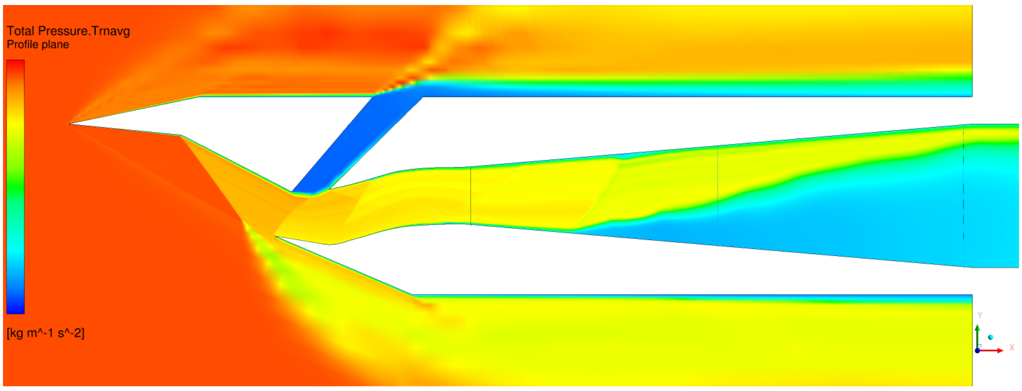
Total Pressure.Trnavg
Profile plane
[kg m^-1 s^-2]

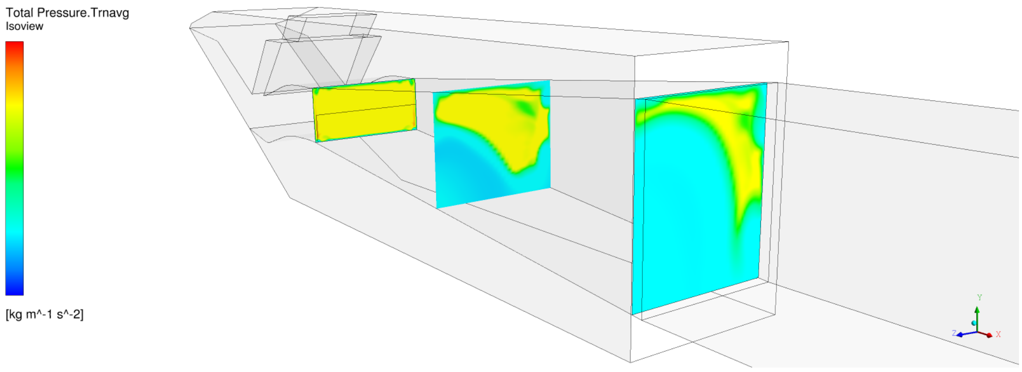
Total Pressure.Trnavg
Isoview
[kg m^-1 s^-2]

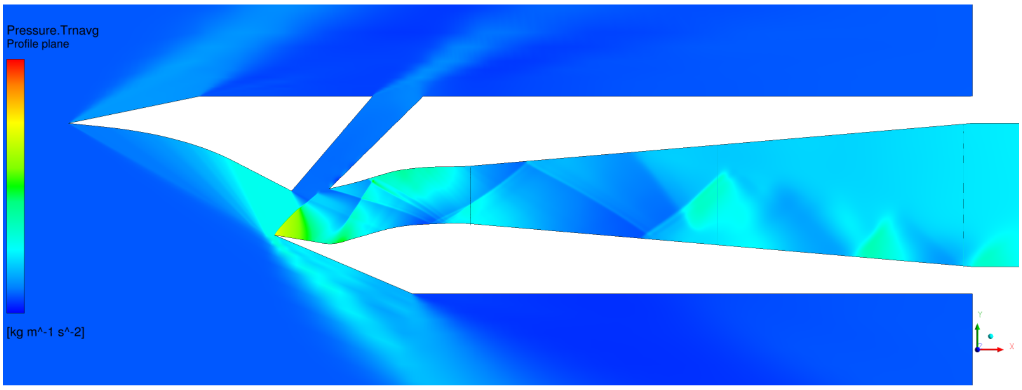
Pressure.Trnavg
Profile plane
[kg m^-1 s^-2]

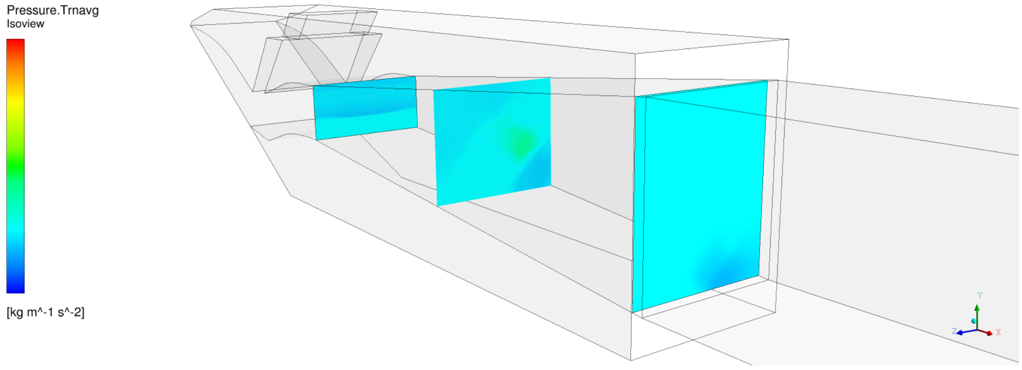
Pressure.Trnavg
Isoview
[kg m^-1 s^-2]

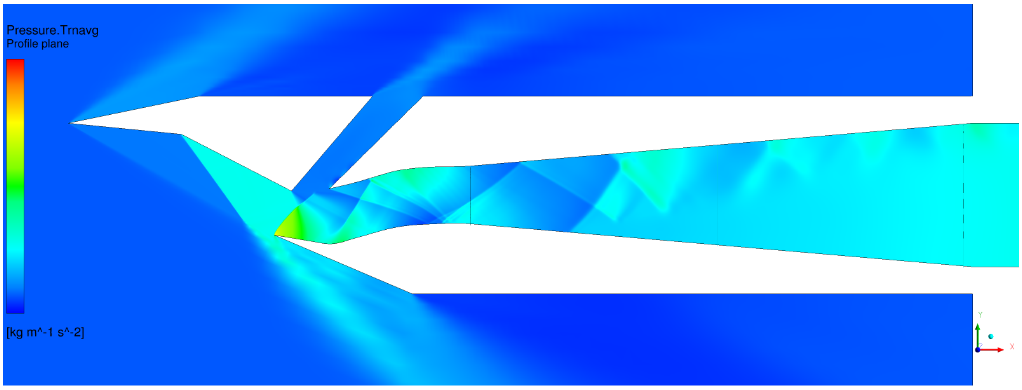
Pressure.Trnavg
Profile plane
[kg m^-1 s^-2]

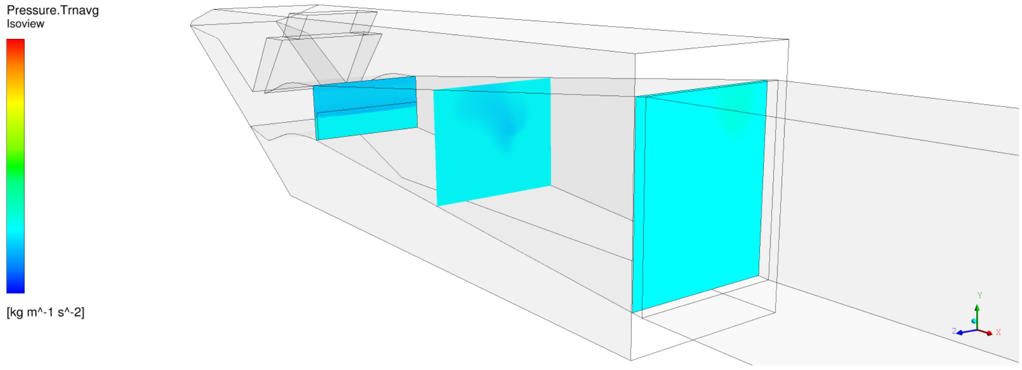
Pressure.Trnavg
Isoview
[kg m^-1 s^-2]

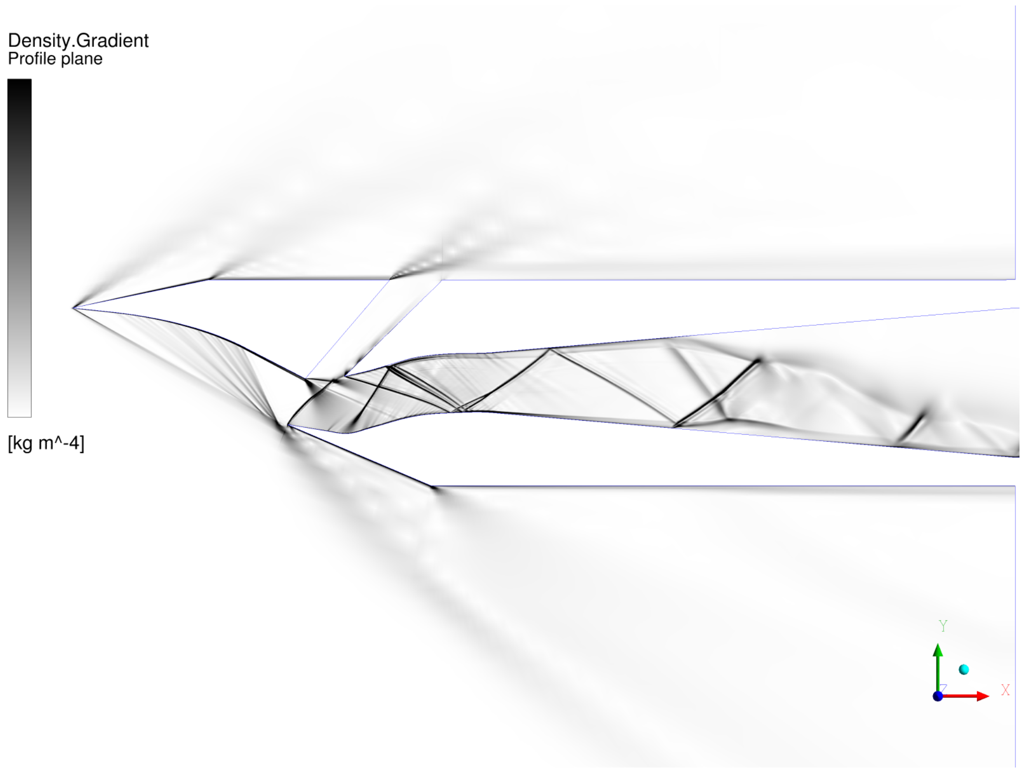

Density.Gradient
Profile plane
[kg m^-4]
Y
X

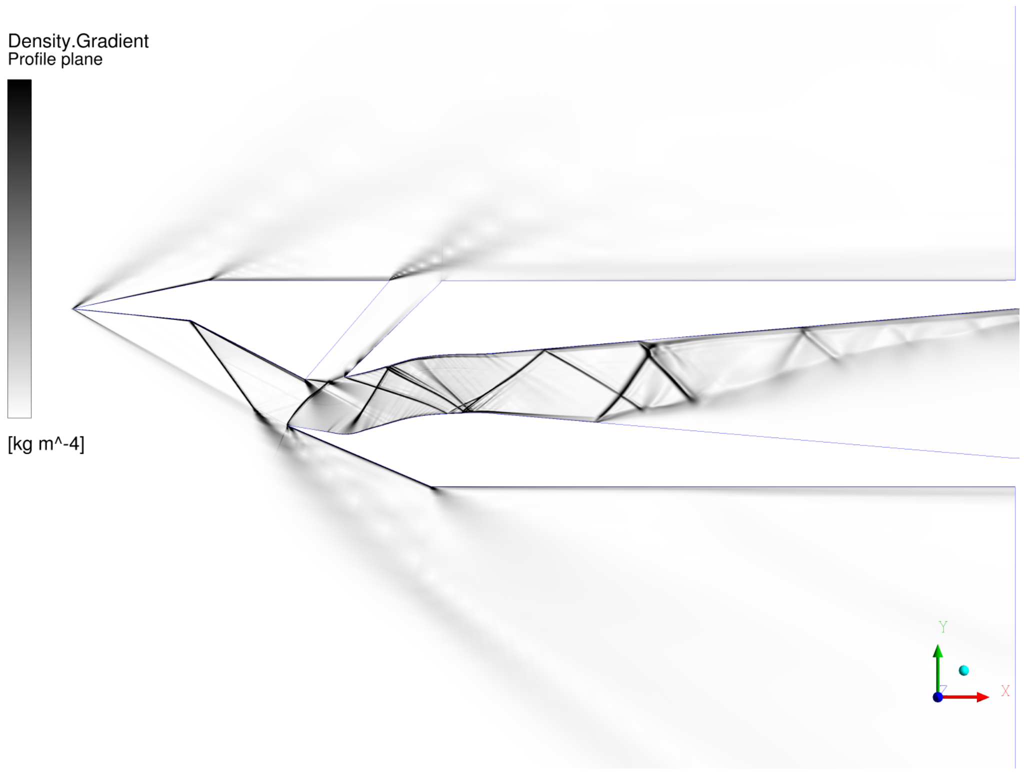

Density.Gradient
Profile plane
[kg m^-4]
Y
X

G Parametric study simulation, $M_{P,3}$

G.1 Subcritical operating range, $p_{3,4}$

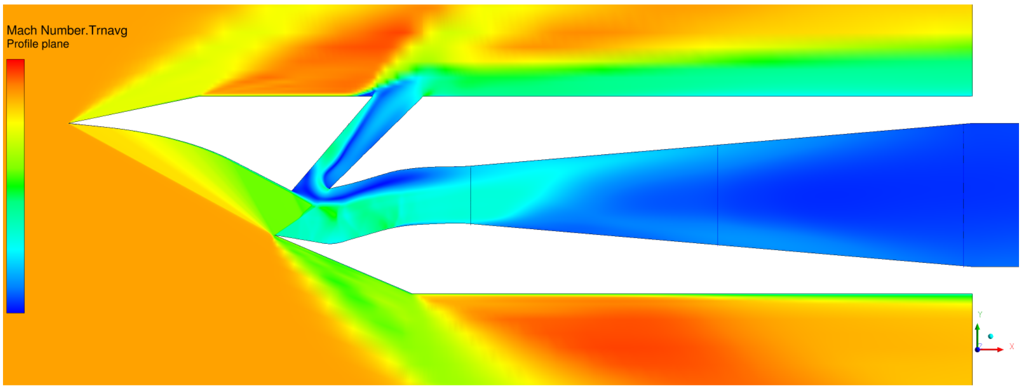

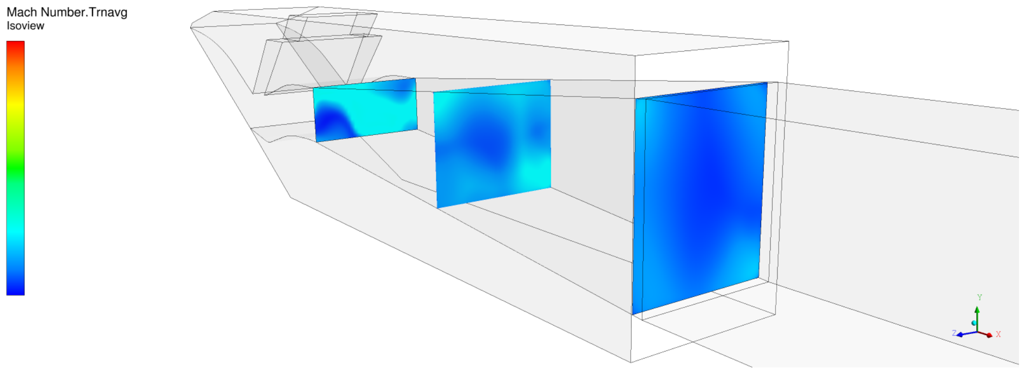

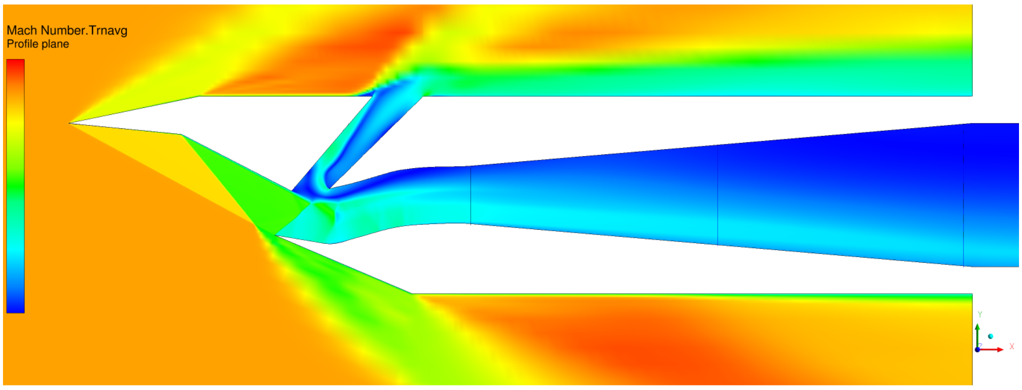

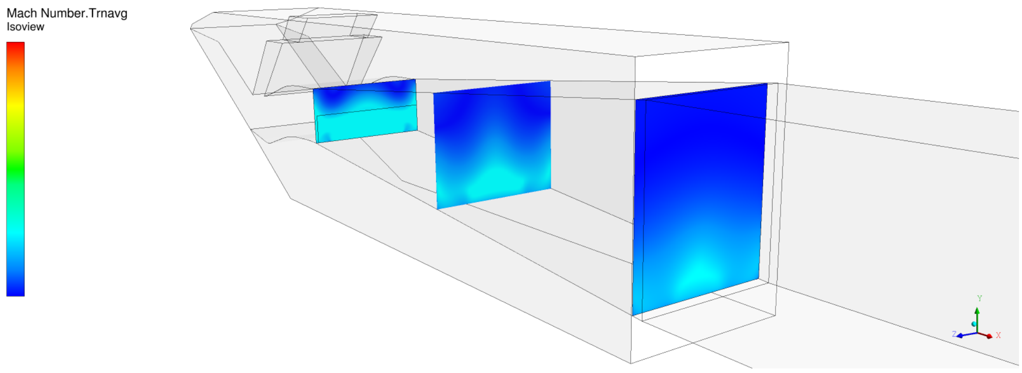

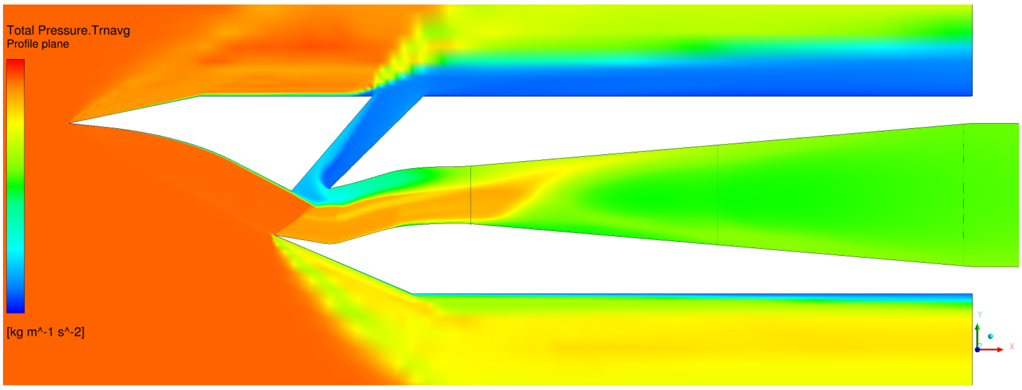
Total Pressure.Trnavg
Profile plane
[kg m^-1 s^-2]

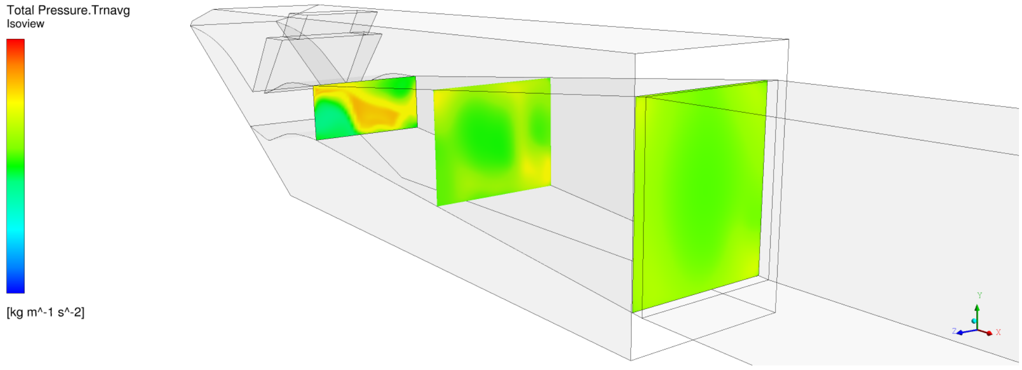
Total Pressure.Trnavg
Isoview
[kg m^-1 s^-2]

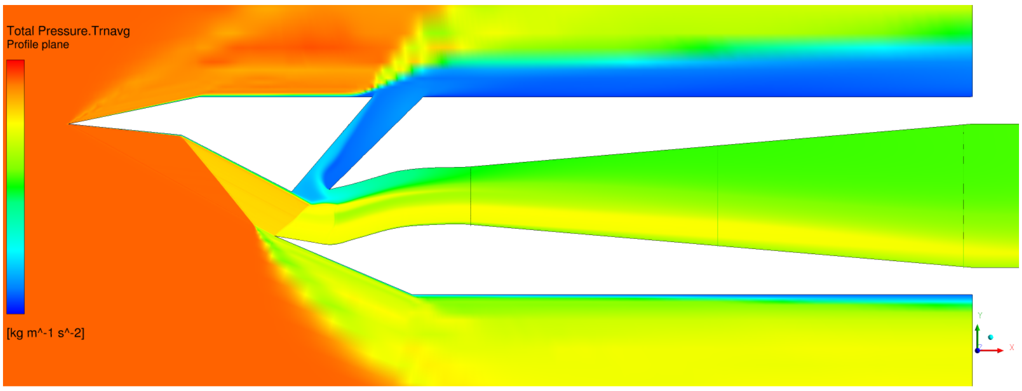
Total Pressure.Trnavg
Profile plane
[kg m^-1 s^-2]

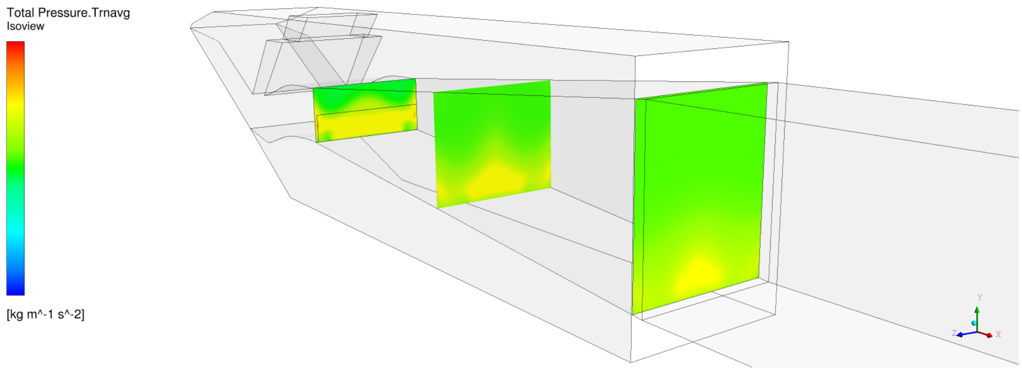
Total Pressure.Trnavg
Isoview
[kg m^-1 s^-2]

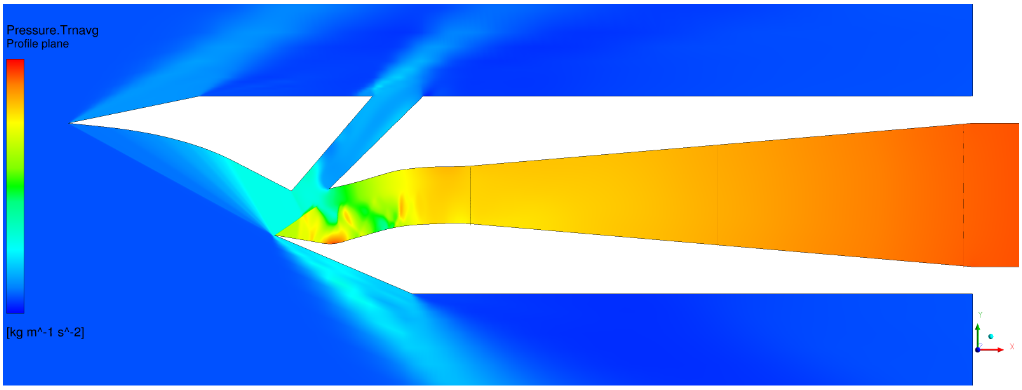
Pressure.Trnavg
Profile plane
[kg m^-1 s^-2]

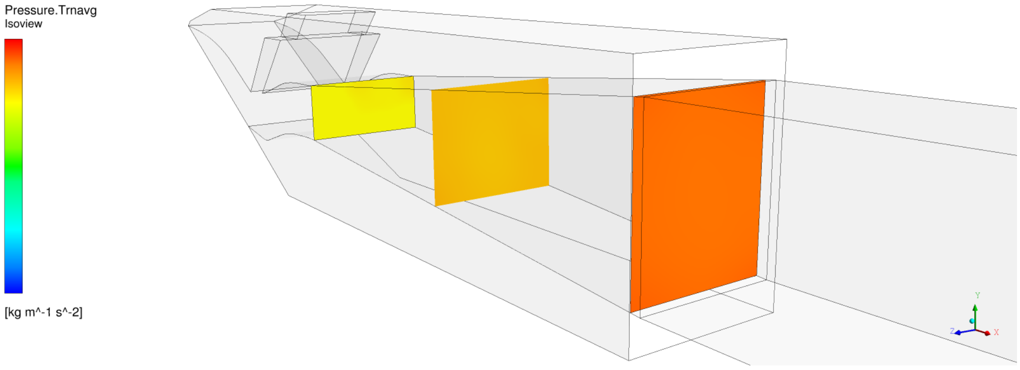
Pressure.Trnavg
Isoview
[kg m^-1 s^-2]

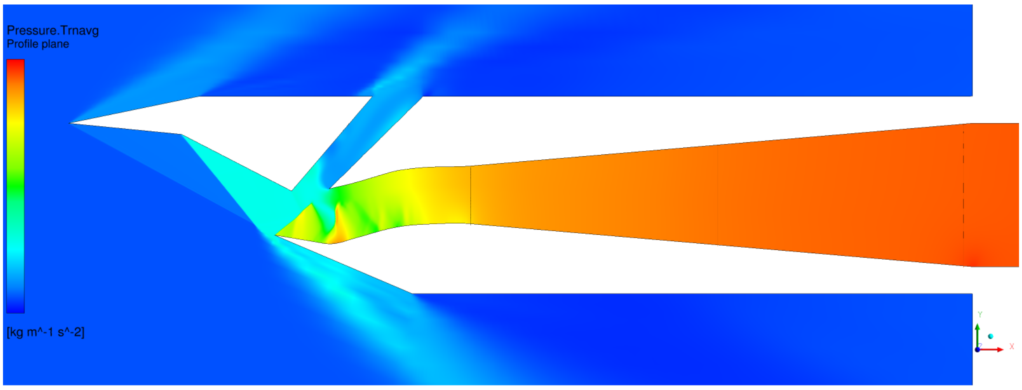
Pressure.Trnavg
Profile plane
[kg m^-1 s^-2]

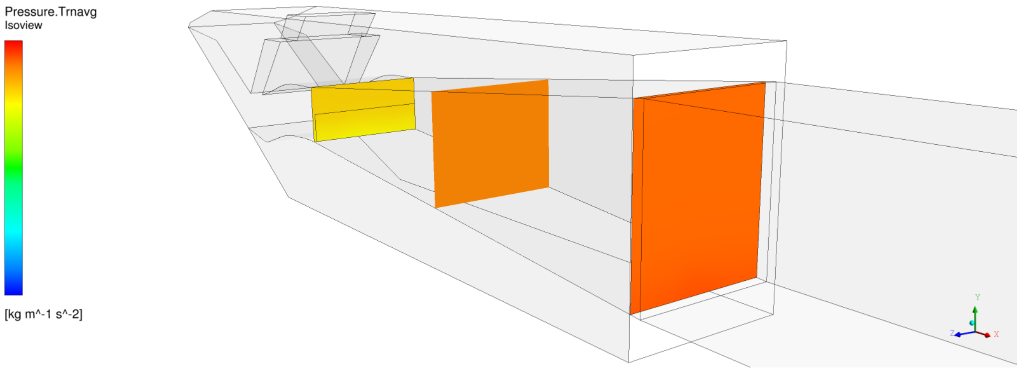
Pressure.Trnavg
Isoview
[kg m^-1 s^-2]

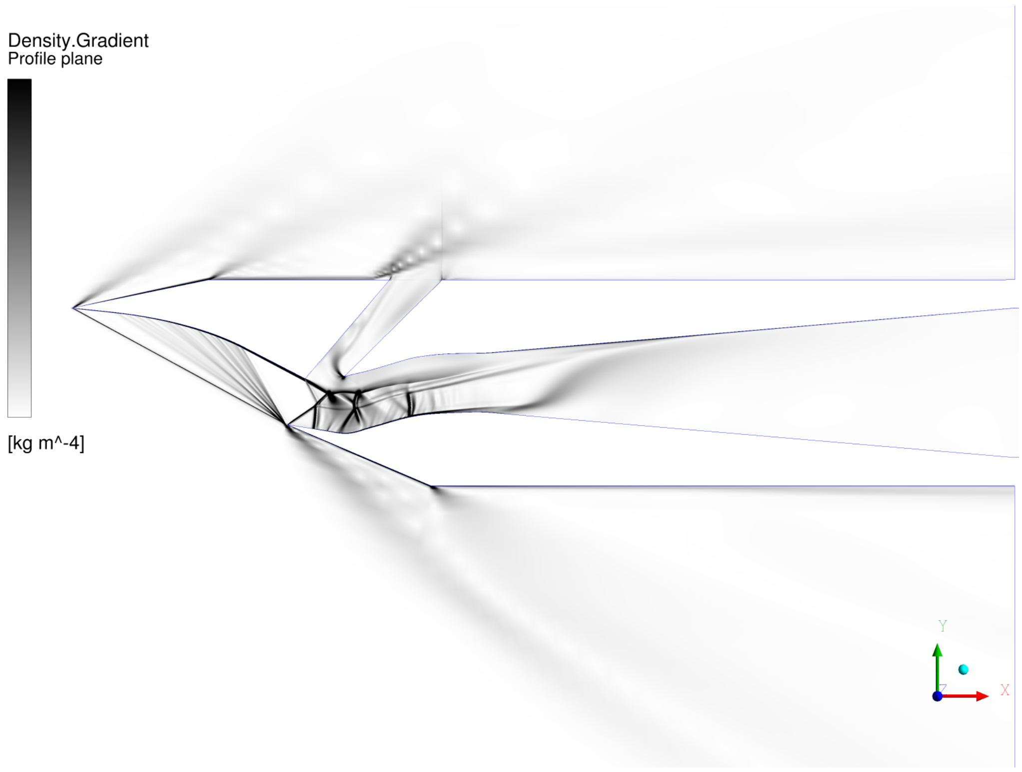
Density.Gradient
Profile plane
[kg m^-4]
Y
X

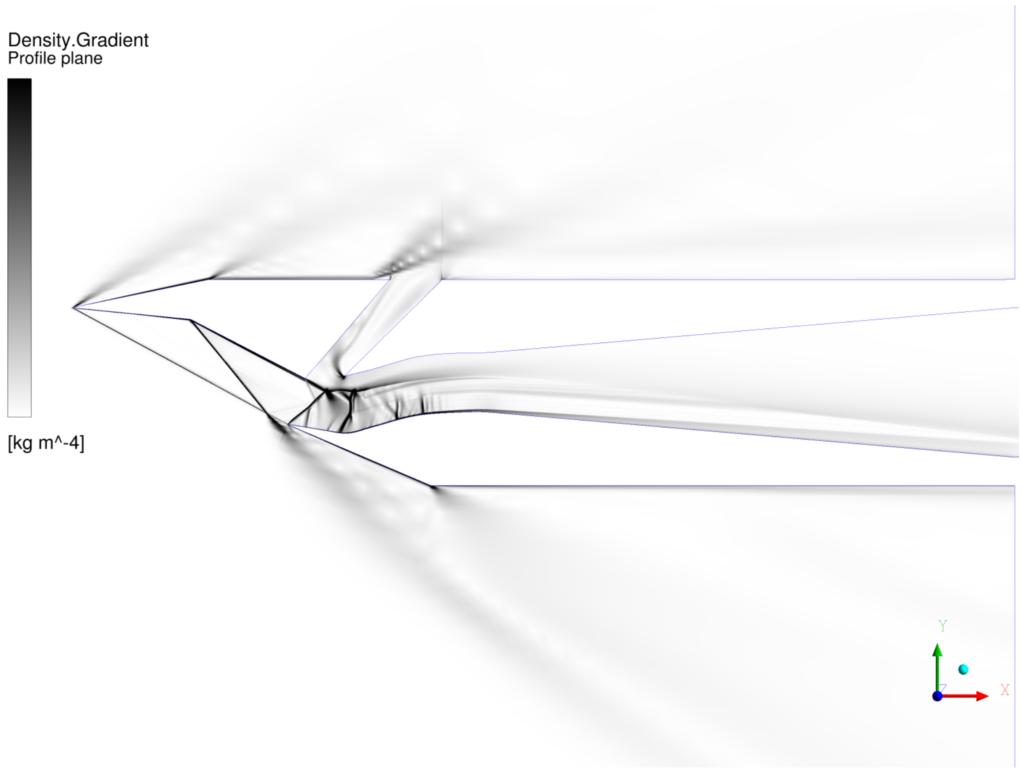
Density.Gradient
Profile plane
[kg m^-4]
Y
X

G.2 Supercritical operating range, $p_{3,1}$

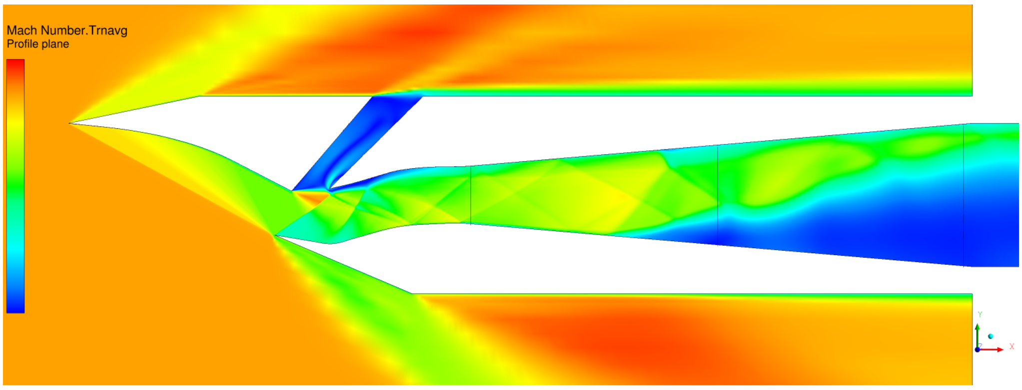

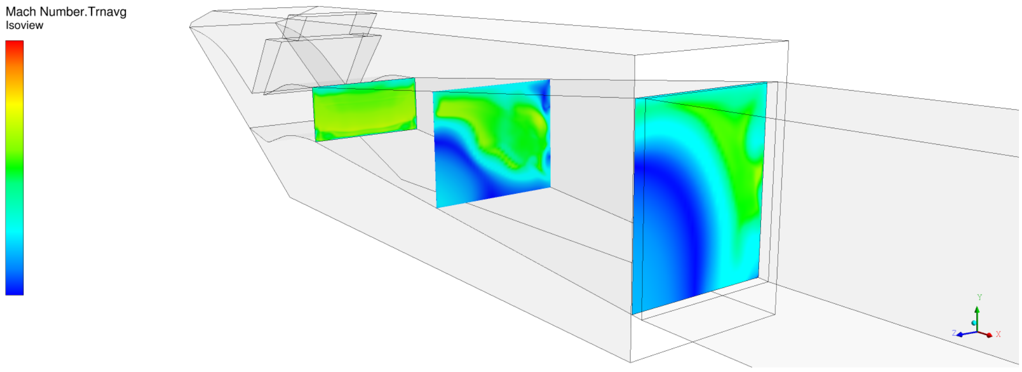

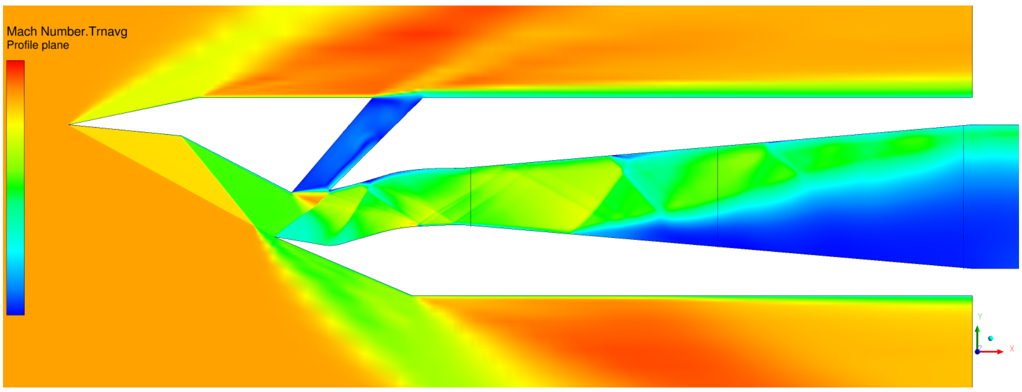

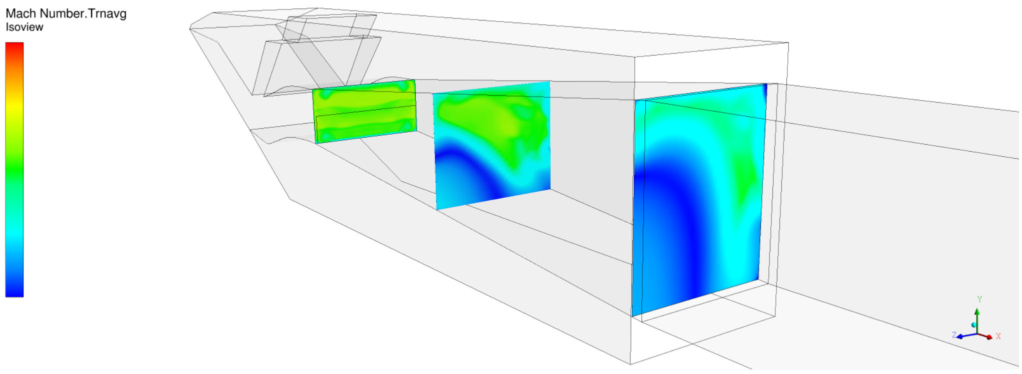

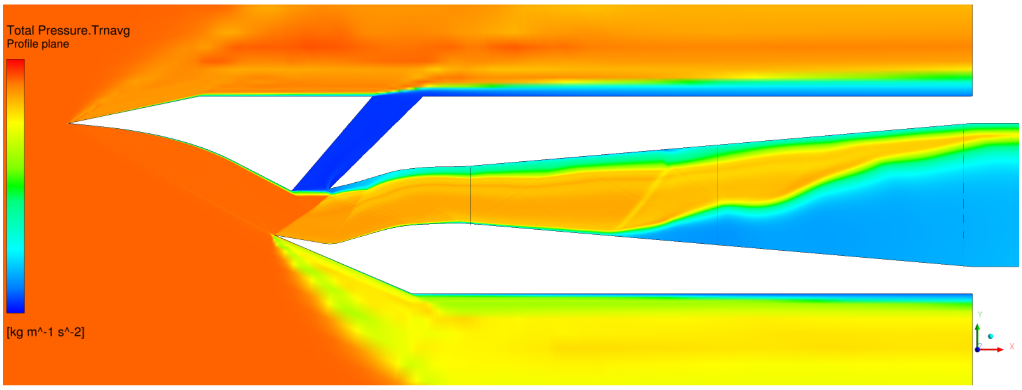
Total Pressure.Trnavg
Profile plane
[kg m^-1 s^-2]

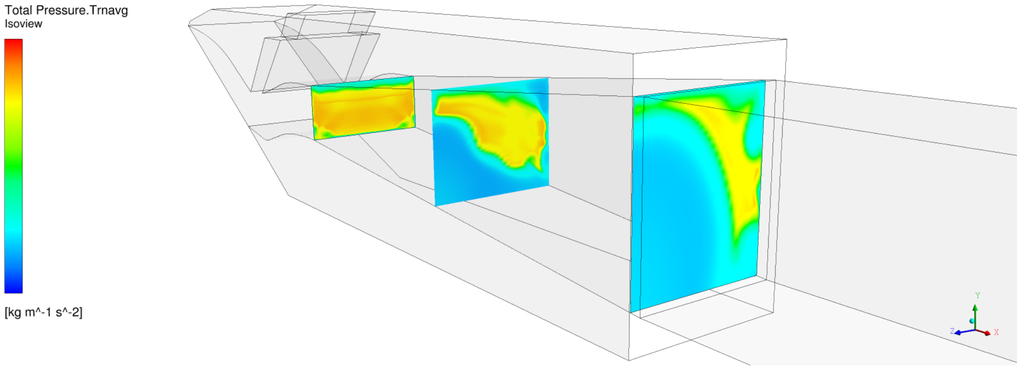
Total Pressure.Trnavg
Isoview
[kg m^-1 s^-2]

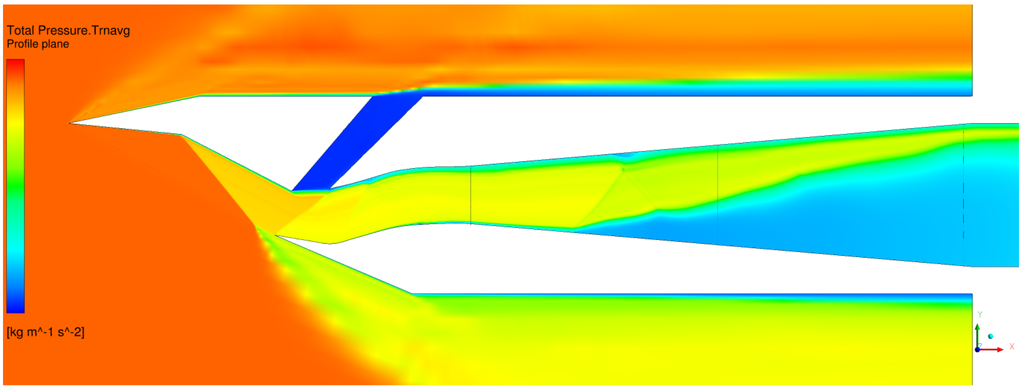
Total Pressure.Trnavg
Profile plane
[kg m^-1 s^-2]

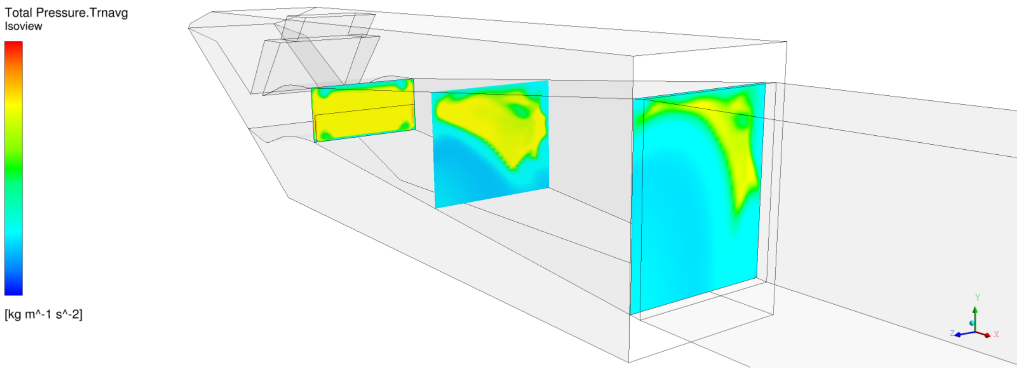
Total Pressure.Trnavg
Isoview
[kg m^-1 s^-2]

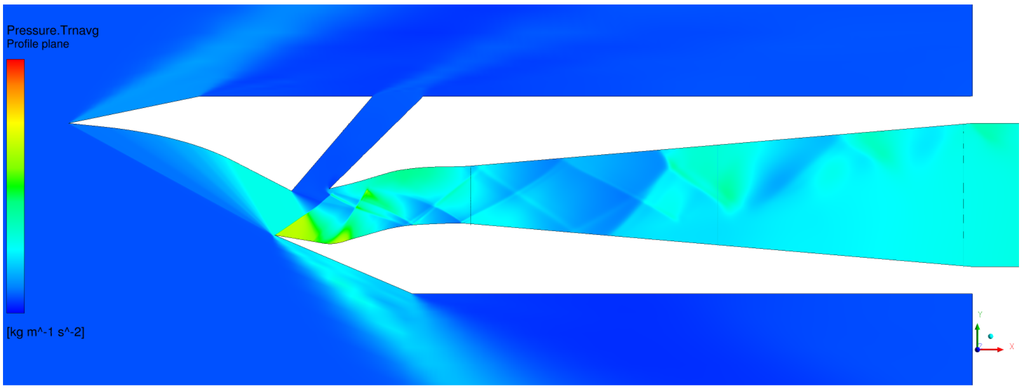
Pressure.Trnavg
Profile plane
[kg m^-1 s^-2]

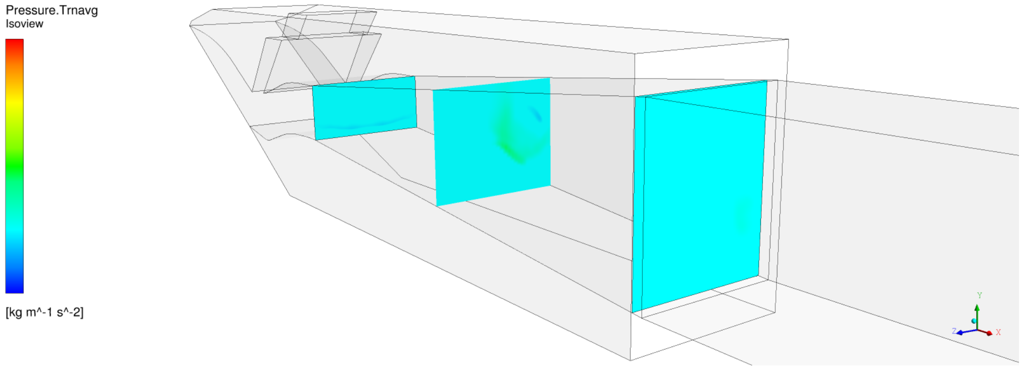
Pressure.Trnavg
Isoview
[kg m^-1 s^-2]

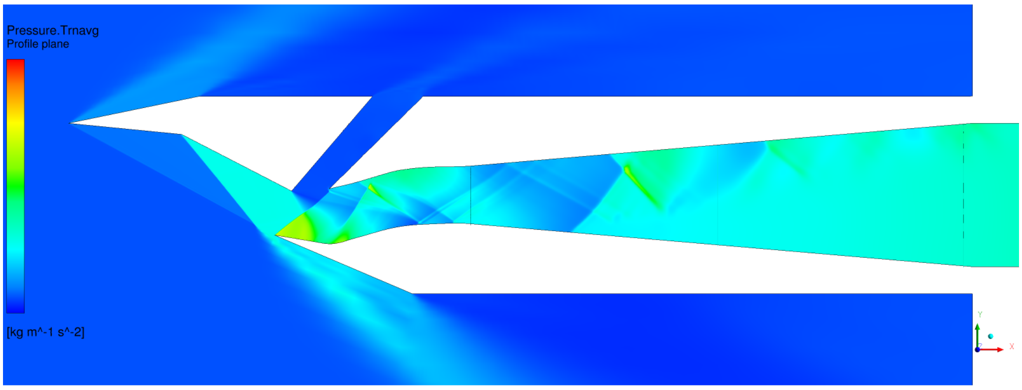
Pressure.Trnavg
Profile plane
[kg m^-1 s^-2]

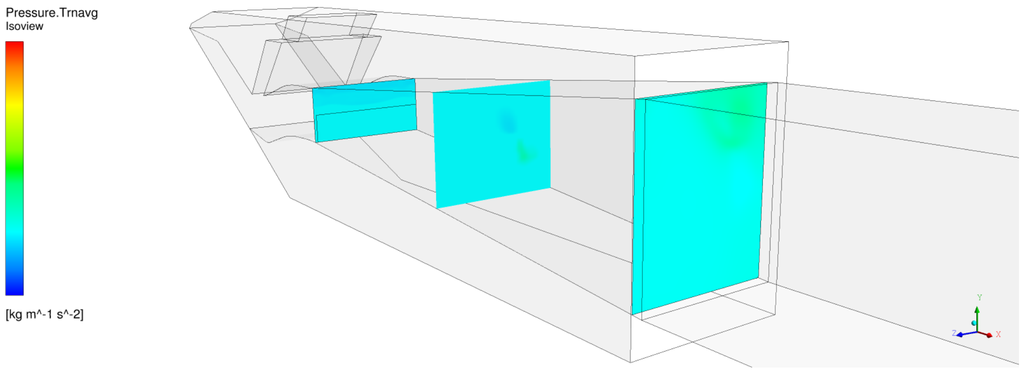
Pressure.Trnavg
Isoview
[kg m^-1 s^-2]

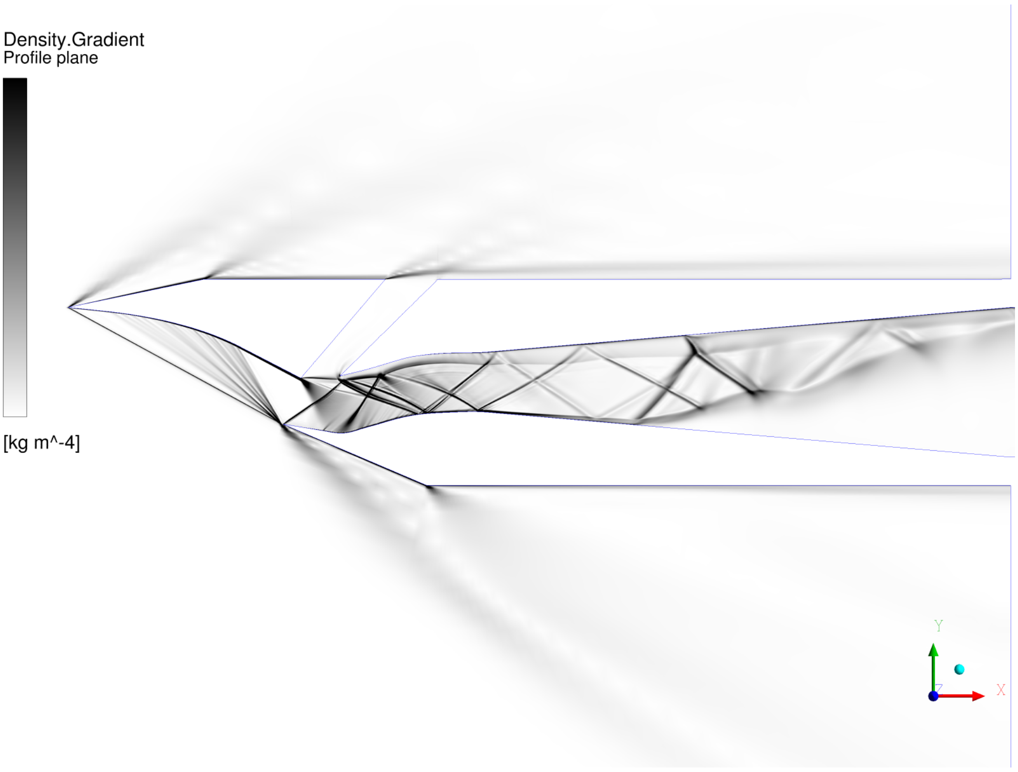
Density.Gradient
Profile plane
[kg m^-4]
Y
X

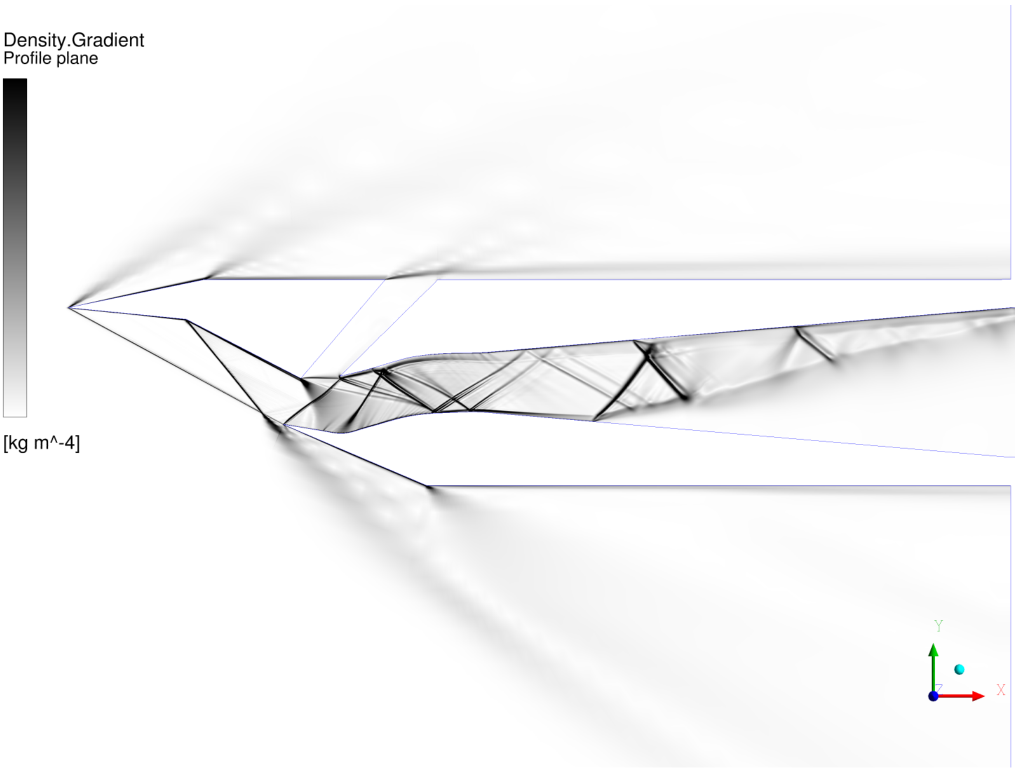
Density.Gradient
Profile plane
[kg m^-4]
Y
X

H Parametric study simulation, $M_{P,4}$

H.1 Supercritical operating range, $p_{4,1}$

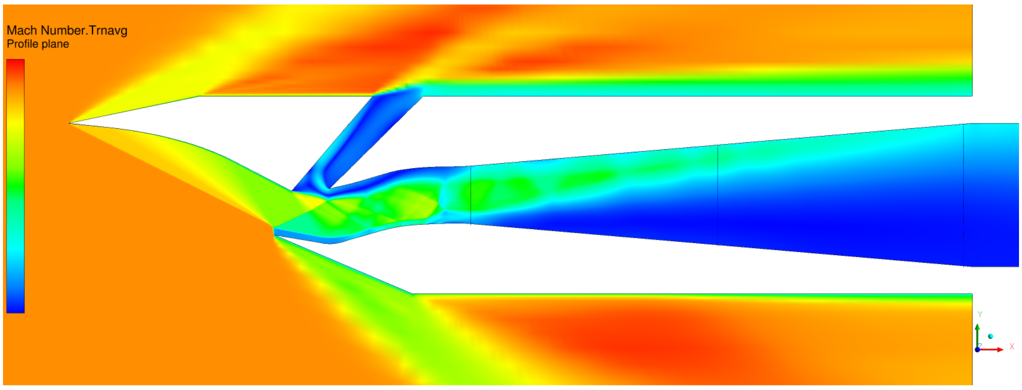

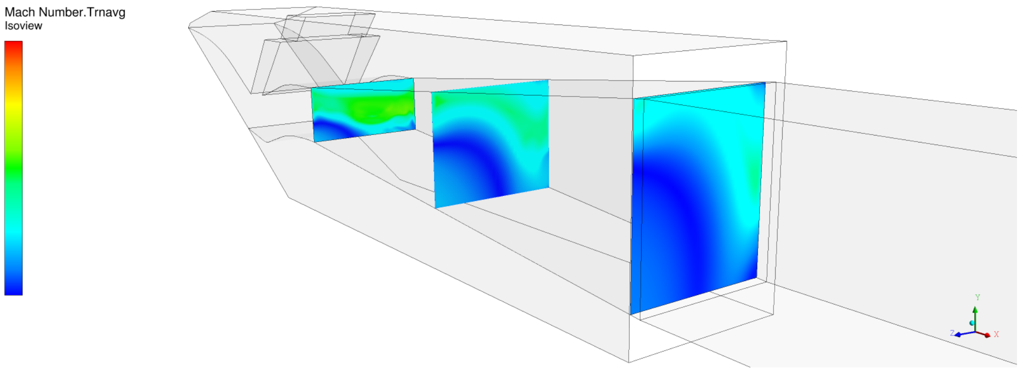

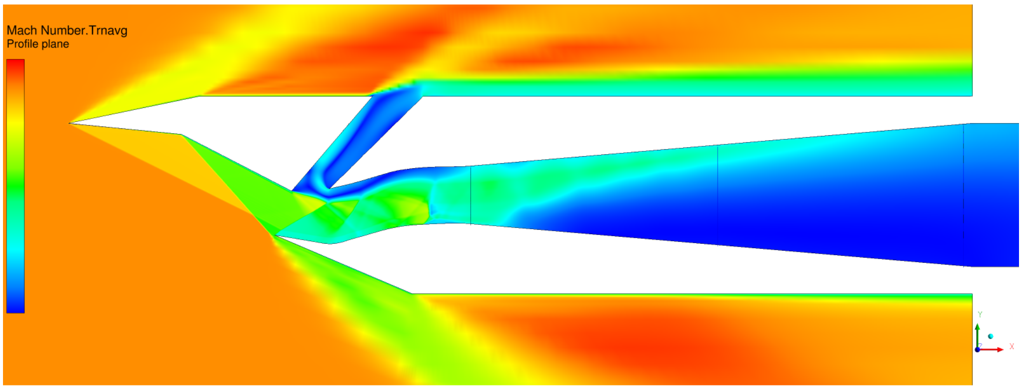

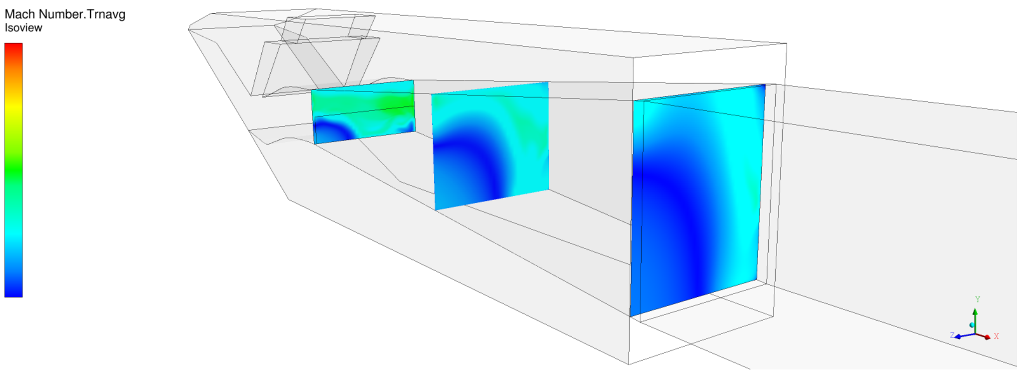

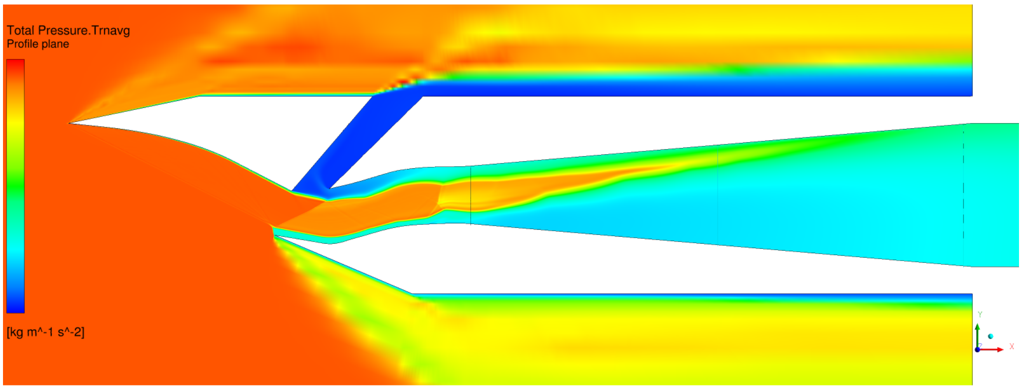
Total Pressure.Trnavg
Profile plane
[kg m^-1 s^-2]

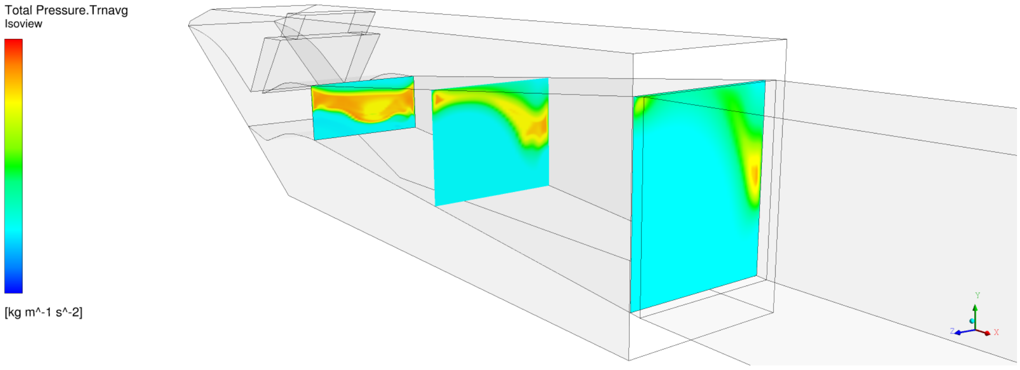
Total Pressure.Trnavg
Isoview
[kg m^-1 s^-2]

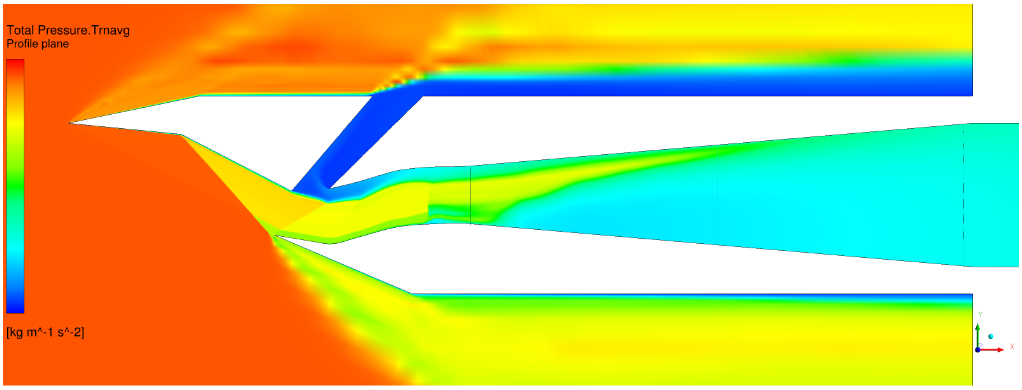
Total Pressure.Trnavg
Profile plane
[kg m^-1 s^-2]

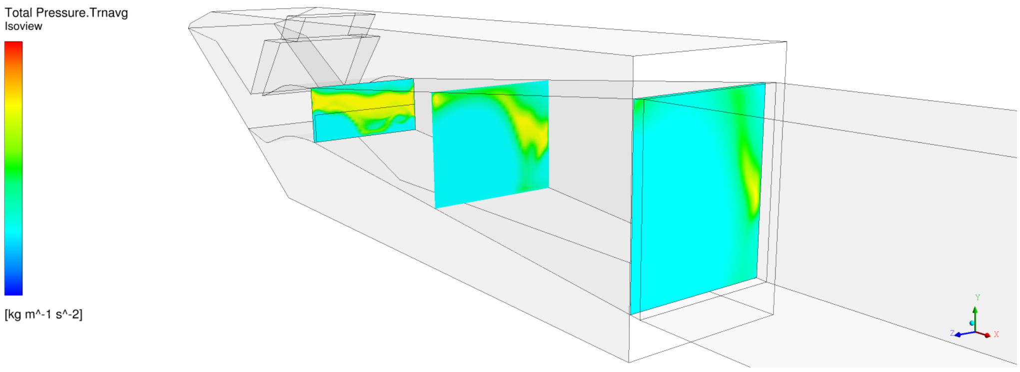
Total Pressure.Trnavg
Isoview
[kg m^-1 s^-2]

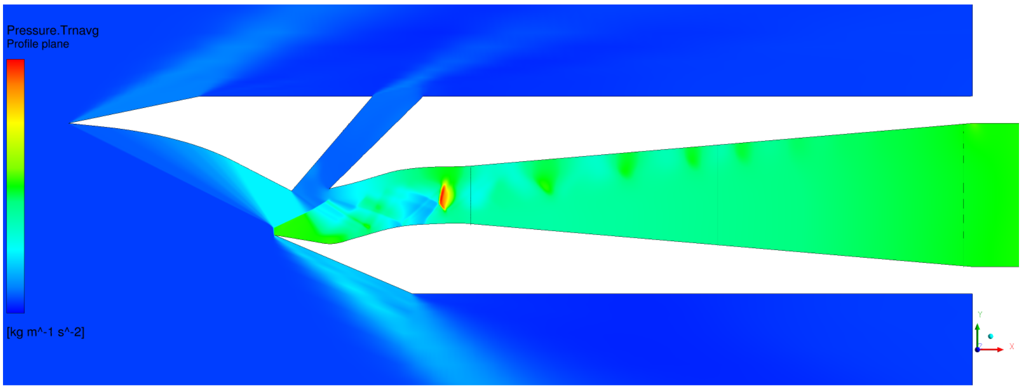
Pressure.Trnavg
Profile plane
[kg m^-1 s^-2]

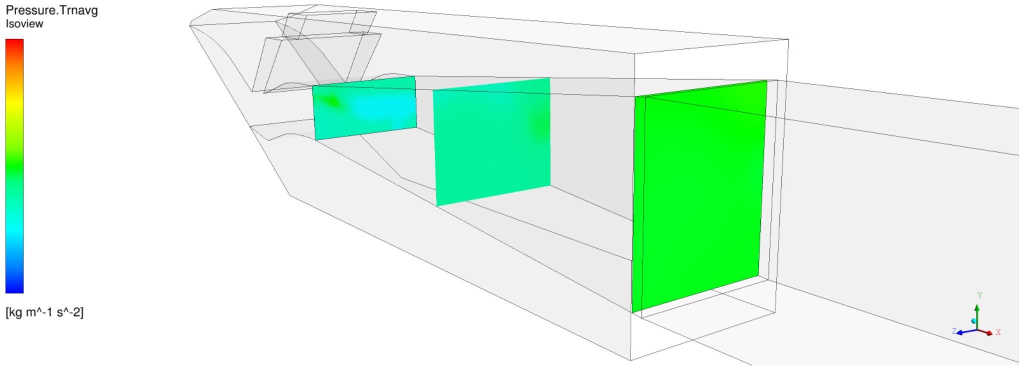
Pressure.Trnavg
Isoview
[kg m^-1 s^-2]

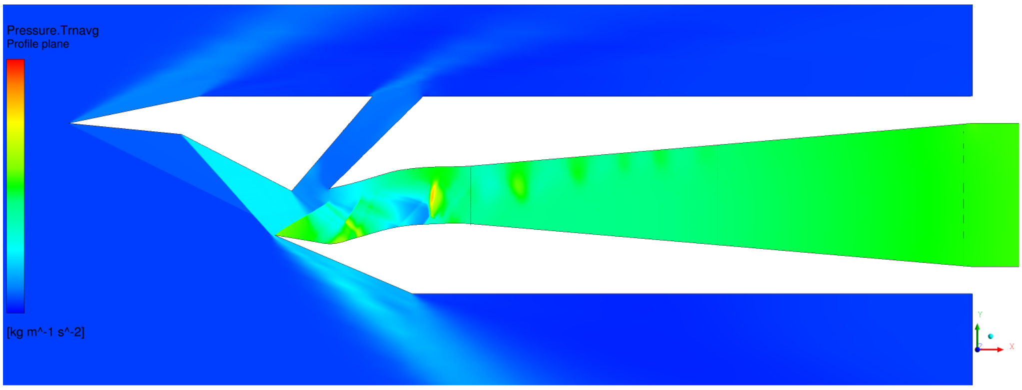
Pressure.Trnavg
Profile plane
[kg m^-1 s^-2]

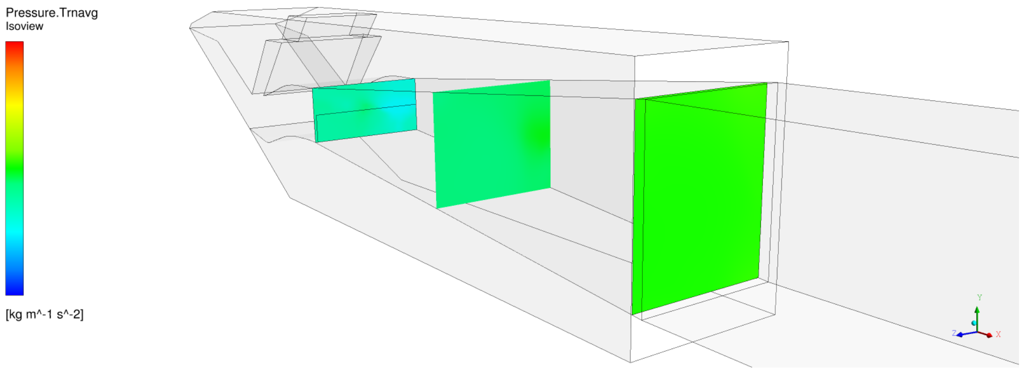
Pressure.Trnavg
Isoview
[kg m^-1 s^-2]

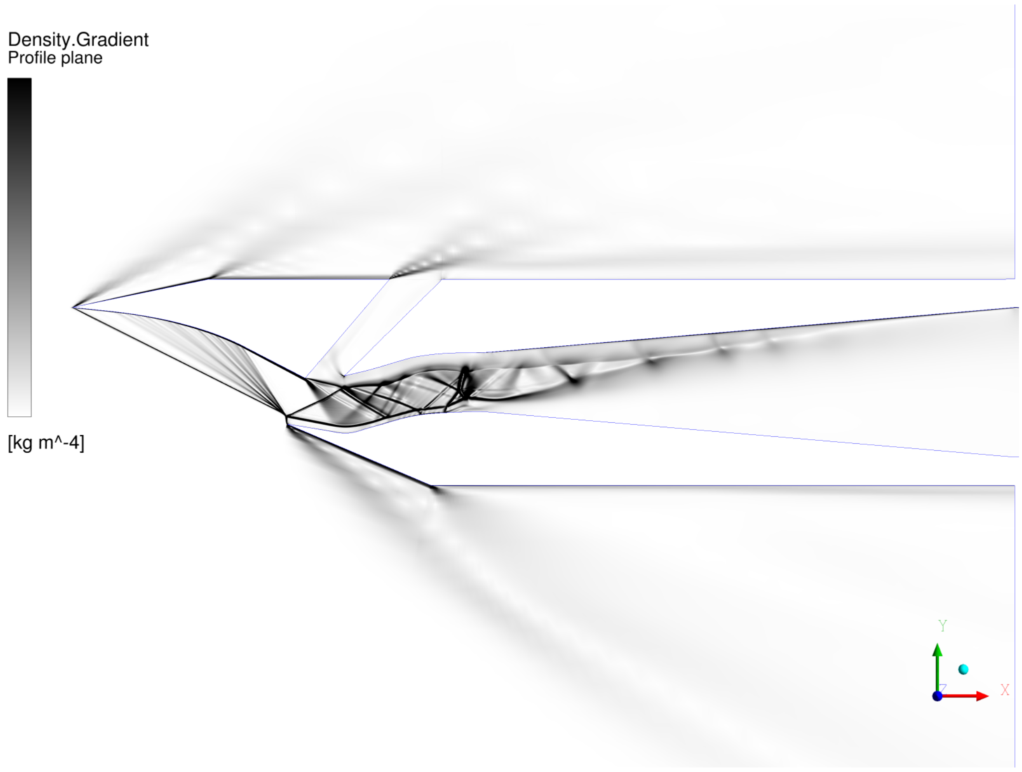
Density.Gradient
Profile plane
[kg m^-4]
Y
X

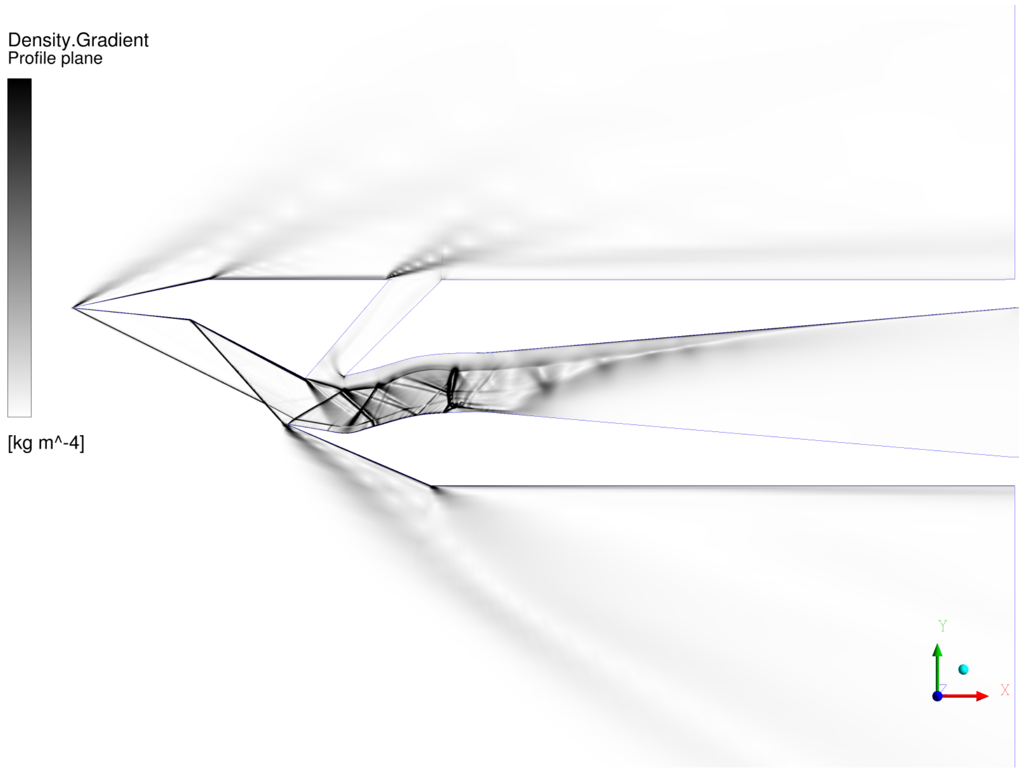
Density.Gradient
Profile plane
[kg m^-4]
Y
X